Microfabricated Optofluidic Ring Resonators for Sensitive, High-Speed Detection of Volatile Organic Compounds

by

Kee William Scholten

A dissertation submitted in partial fulfillment
of the requirements for the degree of
Doctor of Philosophy
(Applied Physics)
in The University of Michigan
2015

Doctoral Committee:
       Professor Edward T. Zellers, Chair
       Professor Xudong Fan
       Profess Cagliyan Kudrak
       Associate Professor Wei Lu

DEDICATION

To my family, friends and teachers

ACKNOWLEDGMENTS

TABLE OF CONTENTS

CHAPTERS

LIST OF FIGURES

LIST OF TABLES

LIST OF APPENDICES

CHAPTER I

Introduction

1.1 Dissertation overview

This dissertation describes the research and development of a novel microsensor which exploits the properties of optical resonance for the detection of volatile organic compounds (VOCs). The project was motivated by the need for a miniaturized device capable of rapid, sensitive, and selective detection of VOC analytes for a micro-scale gas chromatograph (μGC). The proposed device required the invention and integration of both a physical transducer and a chemical interface layer, as such this research has two primary focuses; the development of a microfabricated optofluidic whispering gallery mode (WGM) resonator and sensor for VOC detection, and the study of thiolate-monolayer protected gold nanoparticle (MPN) films as a sorptive material with differentiable optical responses to VOCs.

This research was part of a longstanding collaborative effort between the Enviromental Microsystems group headed by Professor Zellers and the Center for Wireless Integrated MicroSensing Systems (WIMS[2]) at the University of Michigan to develop μGC systems. These systems, which integrate multiple microelectromechanical systems (MEMS), show promise for *in situ* analysis of VOC mixtures at ambient air concentrations ranging from part-per-million to part-per-trillion. The device presented in this dissertation, named the microfabricated optofluidic ring resonator (μOFRR) sensor, serves to improve upon previously utilized sensor arrays by way of

increased limits of detection (LOD), narrower peak widths, and greater diversity in sensor responses allowing for improved selectivity.

The remainder of Chapter 1 provides the background and significance of this research. Chapter 2 describes initial investigations into chemiresistive sensor arrays composed of multiple materials, gold nanoparticle films and tin-oxide nanowires, as a preliminary study of methods for improving sensor array performance. Chapter 3 details a similar investigation into multi-transducer arrays, combining gold nanoparticle coated chemiresistors and gravimetric sensors. The work in these chapters revealed several short-comings of the studied sensors and approaches; multi-material and multi-transducer arrays did not yield significant improvements in selectivity, and none of the transducers demonstrated the combination of high sensitivity and fast response times desired for μGC applications. This work has been published in the *Journal of Nanotechnology* and the *IEEE Sensors Journal* respectively. The remainder of this dissertation focuses on optical transducers. Chapter 4 describes the design, fabrication and optical characterization of μOFRR structures, and the work in this chapter has been published in *Applied Physics Letters*. Chapter 5 details the creation of a μOFRR sensor from said structures, and presents the performance of the sensor during static and dynamic exposures of several VOCs. Several features of the sensor are reported including sensitivity, detection limits, response time, and transduction mechanism, and operation of the μOFRR downstream from a μGC column is described. The work in chapter 5 has recently been published in the journal *Lab on Chip*. Chapter 6 describes the use of the μOFRR as a detector in a μGC × μGC subsystems for VOC mixture analysis. This chapter describes packaging the μOFRR into a portable assembly with miniaturized ancillary components, and the successful separation of up to 13 components in under 3 minutes with the combined μGC system and μOFRR detector. Chapter 7 describes a study of multi-variable sensing by optical transduction,

as a means for increasing response diversity in microsensors. This chapter reports successful discrimination of two VOCs using a single sensing film, an octanethiol functionalized gold nanoparticle film, probed by transmission and reflectance measurements at multiple wavelengths. This work has been published in the journal *Analytical Methods*. Chapter 8 describes attempts at incorporating a nanoparticle film in to a µOFRR detector, and the successful implementation of a µOFRR coated with a triethylene glycol functionalized nanoparticle film as a µGC detector. Chapter 9 presents conclusions drawn from this thesis and proposes future work on this topic.

1.2 Background and Significance

1.2.1 In situ analysis of VOCs

The need to quantitatively analyze VOCs in complex mixtures is critical to numerous problems of societal concern, including mapping and remediating environmental pollution, assessing human exposure to toxic chemicals, diagnosing disease, battling terrorism, and ensuring indoor air quality. In most cases, the concentrations of VOCs requiring analysis are in the low- or sub-parts-per-billion (ppb) range. Performing such measurements *in situ* increases the quality and quantity of data that can be gathered and permits applications such as bed-side diagnostics and real-time detection of environmental hazards and occupational safety.

Current field-deployable technologies for VOC mixture determinations rely on techniques such as infrared spectrophotometry [1-3], direct-inlet mass spectrometry [4-9], ion mobility spectrometry [10-11], and gas chromatography with one of several detectors [12-28]. Unfortunately, typical instruments are too large and expensive for routine implementation, many lack sufficient sensitivity, and most lack the capability for the quantitative determinations (i.e., identification and quantification) demanded by these applications [29].

The development of micro-scale components for VOC-monitoring, made via Si microfabrication techniques, provides a method for reducing instrument size, cost and encumbrance. In recent years significant advances have been made towards micro-scale VOC detectors and analysis systems [12-19, 21-23, 28, 30-46]. Perhaps the most widely studied are the so called "electronic noses": arrays of standalone (micro)detectors employing sorptive interface materials (e.g. polymers) that interact with vapors through spontaneously reversible, non-bonding, physisorption [47-48]. These devices offer partially, and often predictably, selective responses to VOCs by virtue of using different interface layers, transducers, or by probing different aspects of

a single film; By applying chemometric analyses such as principal component regression or by use of neural networks to the collective response patterns from such arrays, these devices have been shown capable of recognizing many different individual VOCs as well as the components of simple VOC mixtures [48-53].

Despite initial hopes and expectations for such arrays to afford determinations of the components of complex VOC mixtures, it has become apparent that the interaction energies embodied in the reversible partitioning phenomena governing sensor response and the associated changes in the interface probed by the underlying transducers, span ranges too narrow to permit the differentiation of more than two or three vapors when presented to the array simultaneously [49-50, 54].

The most successful approaches to VOC mixture analysis with miniaturized components rely on temporal/spatial separation of analytes prior to detection. Gas chromatography (GC) is the most effective approach to such separations, and µGC systems fabricated using MEMS processing techniques [12-21] represent the most promising technology due to their capability for analyzing mixtures of arbitrary composition while minimizing size and power demand.

1.2.2 Micro-scale Gas Chromatographs

Efforts to miniaturize GC began in 1979 [20] and have enjoyed a resurgent interest in recent years spearheaded by groups at Sandia National Labs [15, 55], the University of Illinois [56-59] , and the University of Michigan [12, 14-15, 17-18, 21, 60]. However, the realization of a fully microfabricated GC system has been complicated by the need for integration of multiple MEMS components and corresponding integrated circuitry capable of precisely manipulating thermal and fluidic conditions at low power. Although most of the scaling laws favor miniaturization of GC system components, due to the limited length (and minimum diameter) of the separation columns

employed in a μGC, it suffers an inherent constraint with regard to resolution; multiple analytes may co-elute, which limits the complexity of the mixtures it can effectively analyze. Additionally the LOD of the microsensor determines the minimum mass of the preconcentrator and minimum length of the sampling period, and so places constraints on minimum instrument size, power demands and duty cycle.

Figure 1-1 presents a simple diagram illustrating the primary MEMS components in an archetypal μGC system. During operation, ambient air is drawn through a preconcentrator, trapping VOC analytes on an adsorbent material. The preconcentrator is then heated very rapidly while the flow is reversed, injecting the VOC mixture as a concentrated pulse into a stream of carrier gas which flows through the downstream components. Next the analytes pass through a microfabricted separation column, comprising a long, narrow channel coated or packed with a stationary phase material into which the VOCs differentially partition as they travel through the channel. Finally analytes elute out of the column, temporally/spatially separated within the carrier stream, passing through a detector or a sensor array, which detects each analyte and ideally permits identificationon the basis of retention time or sensor array response pattern.

1.2.2.1 μGC × μGC

Comprehensive two-dimensional gas chromatography (GC × GC) is a technique for the separation of far more complex mixtures than achievable with traditional chromatography, by separating analytes on a second column that would otherwise co-elute [61]. GC × GC uses two separation columns, each with a separate stationary phase with affinity for a different class of analyte (e.g. polar and non-polar). As analytes elute from the first (longer) column they are refocused and injected by a 'modulator' into the second (shorter) column in narrow bands several

seconds apart. Retention time on the second column can be calculated from the difference in elution time and the nearest modulation.

$\mu GC \times \mu GC$ refers to the implementation of this technology with MEMS components, including μGC separation columns and microfabricated modulator. Conventional modulators rely on pneumatic switching [62-63] or thermal absorption/de-sorption with cryogenic fluids [64-65] for rapid injection into the second column. Efforts at Michigan have produced a MEMS modulator, dubbed the μthermal-modulator, which uses solid-state heating and cooling for rapid, low power modulation [66-67]. Analytes eluting from the first column are retained on a PDMS coated microchannel while the device is cooled, and are then focused and injected into the second column by rapid heating. This produces sharp, concentrated injections of VOCs into the second column. Creating a fully miniaturized $\mu GC \times \mu GC$ system is hindered by the lack of microsensors capable of sufficiently rapid responses; separation on the second column relies on separation times of only a few seconds, thus resolution along the second dimension demands detectors capable of sub-second peak widths.

Considerable research has advanced the design and microfabrication of μGC components: micropreconcentrator [68-76], μcolumns [77-86], μsensors and μsensor arrays [36-37, 39-40, 42-45, 87-97] as well as ancillary components such as MEMS gas pumps [90] and modulators for multi-dimensional chromatography [66-67, 91]. There is great need to develop microsensors capable of low detection limits, rapid responses, and selective responses, as such an advance can reduce the demands on all other components.

1.2.3 Microsensors for VOC detection

A large number of VOC microsensors have been developed by use of MEMS production methods such as lithographic patterning and Si micromachining. Figure 1-2 presents a

representation of a generic microsensor. It has two primary features: an interface layer that will reversibly interact with a VOC and a transducer that will convert this interaction into a readable signal.

Useful interface layers include polymers [38, 42-44, 89, 95, 98-99], ionic liquids [100], nanostructures such as graphene [92], nanowires [101-104], or nanoparticles [36-37, 39-40, 45, 88, 96, 105-106], or biological components [107-108]. Though there has been considerable work on creating targeted interface layers for specific analytes [109], microsensors used as μGC detectors encounter numerous analytes in rapid succession, so the interactions must be non-specific and rapidly reversible. Such interactions are dictated by spontaneously reversible physisorption, such that the magnitude of sensor response is determined by the degree of partitioning into the interface layer. The partition coefficient (K), is defined as the ratio of the concentration of the analyte in the sorbent phase to the gas phase, and provides a useful measure of vapor solubility in interface layers. K values are primarily a function of VOC volatility and the strength of intermolecular interaction between the analyte and the interface layer. For polymer interface layers K can be modeled as [110]

$$K = \frac{\rho RT}{\gamma M p_v} \qquad \text{Eq. 1-1}$$

where ρ and M are the density and molecular weight of the polymer respectively, γ is an ideality constant known as the vapor activity coefficient, and p_v is the saturation vapor pressure of the VOC. The sensitivity of a microsensor to a VOC analyte is therefore inversely proportional to analyte vapor pressure, as less volatile compounds will sorb into interface layers in higher concentrations and yield higher responses

Transducers include but are not limited to resistors [36-37, 39-40, 45, 88-89, 92, 96, 101-104, 106], mechanical resonators [38, 42], capacitors [95], and optical devices [43-44, 99, 105, 108, 111]. The choice of transduction mechanism determines which properties of the analyte-interface interaction are probed, and can include changes in mass, density, refractive index, viscoelasticity, carrier density, and dielectric constant.

For successful application in µGC systems designed for rapid, on-site analysis of unknown mixture,s microsensors must meet the following requirements: high sensitivity (low LOD) to a wide range of analytes, fast response times (narrow chromatographic peaks), low power demands, small footprint, responses that are reversible and linear with concentration across a large dynamic range, compatibility with the flow rates (0.5-3 mL/minute) necessary for efficient chromatographic separation, and compatibility with a wide selection of interface layers. A small set of devices have been successively demonstrated in µGC systems, these include metal-oxide semiconductors [23], surface acoustic wave sensors [15, 22], and nanoparticle chemiresistors [12-14, 17-18, 21, 60].

1.2.3.1 Metal-oxide chemiresistors

Metal-oxide (MOX) films are an attractive material for chemiresistive sensing due to their high sensitivity and low cost. Figure 1-3 depicts a common design of a MOX chemiresistor: MOX nanowires spanning lithographically defined electrical contacts on top of a micromachined joule heater. MOX sensors are operated at high temperatures (> 200°C) [112] while probing the DC resistance across the film. Organic vapors, as well as reducing and oxidizing gases, bind to the surface replacing oxygen terminated sites and either increasing or decreasing charge carrier concentration (holes or electrons depending on the metal) with a corresponding impact on conductivity. The oxidation of VOCs at the surface is typically temperature dependent and gives

rise to unique temperature-response profiles for different analytes [113]. This that can be exploited to discriminate between VOCs by examining responses from multiple MOX sensors operated at different temperatures or from a single sensor with temperature rapidly modulated during operation [114-116]. Though tin-oxide is the most well studied interface material for MOX chemiresistors [112], a large number of other MOX films are available and multiple film arrays have been demonstrated for VOC discrimination [117]. The sensitivity of MOX chemiresistors can be improved by increasing the surface area-to-volume ratio of the MOX material, magnifying the contribution of the surface carriers to bulk conductivity. This can be accomplished through the use of thin films, or to a greater degree with MOX nanowires [101].

1.2.3.2 Nanoparticle chemiresistors

Chemiresistors employing functionalized nanoparticles as interface layers have generated particular interest owing to ease of fabrication and simple design. One type of device consists of microfabricated, interdigital contact electrodes bridged by a thin layer of thiolate monolayer-protected gold nanoparticle (MPN) film: gold nanoparticle cores separated by a mesh of organothiolate ligands (Figure 1-4). Under an applied voltage MPN films conduct by way of eletron tunneling between cores and electron "hopping" along the atoms of the thiolate ligand [118]. Figure 1-5a depicts this conduction mechanism, and Figures 1-5b and c show images of a representative device. Vapors partition into the MPN film and swell the ligands, increasing the intercore spacing (δ), and contribute to the dielectric permittivity of the intercore medium (ε_{th}) [106, 119]. This interaction is probed by measuring the DC resistance across the film, which varies with the length and magnitude of the electron tunneling barrier between adjacent nanoparticle cores.

$$\frac{\Delta R}{R} = e^{\Delta \delta \beta + \Delta E a / kT} - 1 \qquad \text{Eq. 1-2}$$

10

Equation 1-2 is a model of the sensor response of an MPN chemiresistor, defined as the fractional change in DC resistance, where β is the electron tunneling constant and E_a is the tunneling activation barrier which is inversely proportional to ε_{th} [106]. For small changes in δ and E_a the exponential can be approximated as the first two terms of the Taylor expansion, and sensor responses are accurately modeled as linear with analyte concentration [120]. For MPN chemiresistors sensitivity is a function of analyte partitioning into the organic component of the film and the difference in analyte dielectric compared to the of the thiolate ligand. Though MPN chremiresistors have been successfully deployed in µGC, such devices typically produce LODs spanning from 1-100 ng, requiring sampling time of several minutes to achieve < ppm measurements [12-14].

1.2.3.3 Surface acoustic wave resonators

The surface acoustic wave (SAW) resonator is a mechanical transducer that probes changes in the mass or viscoelastic properties of an interface layer. SAW devices consist of a piezoelectric substrate patterned with electrodes and coated in a sorptive interface film, acoustic waves are generated by applying voltage to a 'transmitter' electrode pair and subsequently detected by measuring a potential across a 'receiver' pair. SAW devices exhibit resonance at a frequency determined in part by the density and elasticity of the interface layer which is mechanically coupled to the vibrations of piezoelectric substrate. A common variant of SAW sensors is the thickness shear mode resonator (TSMR) [121-122]. TSMR devices typically consist of quartz discs sandwiched between electrodes, with one side coated with an interface layer (Figure 1-6). Piezoelectric actuation excites a shear mechanical resonance with the viscoelastic interface film moving in or out of phase with the quartz depending on the film thickness [123]. Increases in mass or decreases in rigidity will decrease the frequency of this resonant mode, permitting

11

transduction of VOC sorption into the film. In the acoustically thin regime the change in resonant frequency due to vapor sorption is proportional to the mass of sorbed vapor, and can be modeled simply by [124]

$$\frac{\Delta f_v}{f} = \frac{C_v K}{\rho}$$

where C_v is the concentration of the analyte in the gas phase, and ρ is the density of the analyte in the liquid phase. TSMRs typically suffer from low sensitivity and comparatively large sizes, making them poorly suited for μGC applications. However their function as micro-scale balances makes them an important tool for direct measurements of interface layer partition coefficients.

1.2.3.4 Sensor dynamics

Regardless of the choice of transducer or interface layer, microsensor performance in a μGC system will be strongly dependent on the time required for a sensor to respond to an analyte. The number of analytes that can be resolved in a given period is in part determined by the speed of the sensor response; slow responses broaden chromatographic peaks and constrain the complexity of the mixture that can be analyzed without analytes co-eluting. Sensor response time is determined by four factors: the bandwidth of the VOC as it is injected into the microsensor (t_1), the time required for the VOC to be cleared from the space over the interface layer (t_2), the time required for the VOC to diffuse into and out of the interface layer (t_3), and the time required for the transducer to respond (t_4). The injection peak width into the sensor is ultimately the limiting factor, and is determined by upstream chromatographic separation or injection. The time required to fill and then clear the space over the interface layer is dependent on flow rate, and the volume and design of the flow cell containing the sensor. The minimum value of t_2 is (cell volume)/(flow rate), however this can be increased by mixing or turbulent flow within the

volume. t_3 is determined by rate of Fickian diffusion into the sorptive interface layer and the evaporation rate of the analyte out of the film. As such t_3 is determined largely by film thickness, the saturated vapor pressure of the VOC, and temperature. Increasing temperature or decreasing the thickness of the interface layer can reduce response time, however there is often a corresponding decrease in sensitivity, as this reduces the amount of analyte condensed onto the transducer [96]. t_4, the read rate of the transducer itself is rarely a limiting factor and can typically be ignored. Achieving rapid sensor responses with microsensors typically requires minimizing flow cell volume and film thickness. This exerts an influence on transducer choice: devices that can be easily integrated with low dead-volume flow cells and fluidic interconnects, and can operate sensitively with only thin interfacial films, are preferred as they enable microsensors with faster response times.

1.2.4 VOC microsensor arrays

Microsensor arrays are frequently employed to achieve limited but critical differentiability between VOC analytes. A microsensor array typically comprises several closely spaced transducers each coated with a different interface layer. VOC analytes will preferentially partition into interface films for which they have greater chemical affinity, and the relative sensor responses can yield a pattern that permits discrimination between analytes. Microsensor arrays require non-destructive transduction mechanisms and low volume interface layers, such that uptake of VOC by one sensor does not diminish the response of downstream sensors in the array. Examples of microsensors used with chromatographic separations include MPN chemiresistor arrays made using multiple MPN films with different ligand moieties [36-37, 40, 45, 88, 96], and mechanical resonators coated with different polymers [42, 52].

Choice of interface layers ultimately determines the limits of array selectivity; an ideal array contains sorptive materials which vary significantly in their affinity for analytes such that the diversity of possible sensor responses is maximized. In practice, however, partitioning is dominated by vapor pressure regardless of interface film, and it can be difficult to find even a small range of interface layers that do not give rise to correlated responses. The partition coefficient K can be expressed a linear combination of just five terms describing analyte-sorbent interaction through the use of linear solvation energy relationships (LSER) [47, 125-126].

$$\log K = c + rR_2 + s\pi_2^H + a\Sigma\alpha_2^H + b\Sigma\beta_2^H + Log\ L^{16} \qquad \text{Eq. 1-4}$$

The solvaton parameters R_2, π_2^H, $\Sigma\alpha_2^H$, $\Sigma\beta_2^H$, and log L^{16} are descriptors of the analyte encompassing polariziability, dipolarity, hydrogen bond acidity, hydrogen bond basicity, and dispersion forces, respectively. The coefficients r, s, a, b, and l describe the corresponding contributions from the sorbent material. This model reveals the finite degrees of freedom which describe variation in VOC partitioning. This places an inherent limit on the diversity of the response patterns achievable with such arrays and as a consequence places an upper bound on microsensor selectivity. Studies have shown repeatedly that this obstacle cannot be overcome simply by increasing the number of sensors in an array, as no complementary information is provided once all solvation parameters are represented among the employed interface layers [49-50, 127].

1.2.4.1 Chemometric analysis

The collection of microsensor responses from an array can be formed into a 'sensor response pattern', which is then used to identify the analyte from an existing library of calibrated responses. A variety of statistical methods exist for quantifying similarities between response

patterns, which can be used to perform such identifications as well as to quantify the performance of an array. In the simplest approach, sensor responses form an n-dimensional vector which is sum-normalized to remove the influence of analyte concentration. Sensor patterns are then matched on the basis of the shortest Euclidean distance between points in this n-dimensional space. In principal component analysis (PCA) the space is reduce to the two or three orthogonal dimensions that capture the greatest degree of variation in responses, this allows for easy visualization of how the response patterns differ between analytes [128]. Figure 1-7 illustrates the transformation from sensor calibrations, to response pattern, to PCA analysis. The limited range in possible sensor responses constrains the available space spanned by the principle components; this constraint, combined with noise in sensor responses, gives rise to confusion and incorrect identifications.

Microsensor array performance can be evaluated by the frequency of correct determinations of an unknown analyte, called the recognition rate (RR). RR is improved by increasing the diversity and decreasing the noise in sensor responses. Extended disjoint principle component regression (EDPCR) is an important method for estimating RR from a limited data set [129]. With EDPCR, Monte Carlo simulation is used to create a large, simulated set of sensor patterns for a library of VOCs by inducing random noise on experimentally collected sensor responses. Each data point is assigned a position along a single principle component, and assigned an identity based on proximity. The correct fraction of assignments is the estimated RR for that array and set of vapors. Experiments have shown that only a few sensors are required in an array to easily reach RR > 90% for libraries of up to 16 VOCs [130], however, RR decreases sharply when sensor arrays are challenged with simultaneous exposures of simple VOC mixtures. Achieving RR of greater than 90% for even a single quaternary mixture has eluded current efforts.

1.2.4.2. Multi-transducer and multi-variable arrays

Enhancing the successful VOC recognition rates of microsensor arrays, particularly when challenged with binary or ternary mixtures, can be achieved with partial success through the deliberate combination of complementary transducers or transduction mechanisms: devices that probe independent chemical properties of vapor interactions for the same surface chemistries. Multi-transducer (MT) arrays include dissimilar transducers with the same interface layers in a single array, examples include sets of polymer coated cantilevers, capacitors, calorimeters and microbalances used for VOC determinations [54, 127, 131-133]. By probing the same interface material in a MT array information can be extracted describing physical properties of an analyte; for example VOC dielectric constants were successfully derived from the combined responses of chemiresistors and TSMRs coated with the same MPN film interface layer [106]. MT arrays have demonstrated marginal, but measurable, improvement in selectivity over single transducer (ST) arrays [54, 98, 127, 134].

Multi-variable (MV) arrays rely on a single transducer operated in multiple different modes to extract additional information. Examples include polymer coated RFID antennae probed for changes in film resistance and capacitance [98], or mechanical resonators operated at different resonant modes to probe for changes in mass-loading or elastic coefficients [135]. This approach allows for a small set of VOCs to be differentiated with measurements from a single device. An integrated array of MV sensors could provide a larger diversity of responses achievable based on relative physisorption alone, and increase selectivity beyond that typically seen in ST arrays.

While the attributes of existing microsensor arrays (small size, low power dissipation, and low-cost production via high-volume microfabrication) are compelling, additional innovation is

needed to improve the diversity of responses, the speed of responses, and sensitivity provided by such devices, and thereby their utility for VOC analysis.

1.2.5. Optofluidic resonators and sensors

Optofluidic sensors integrate high-quality-factor resonators into a microfluidic pathway, providing a platform for optical transduction of VOC analytes compatible with μGC systems. The OFRR is a variant of other whispering gallery mode (WGM) resonator architectures that have been adapted for analysis in the liquid and vapor phase [136-144]. A WGM resonator consists of an optical cavity formed from a waveguide in a ring, disk, sphere or toroid shape, that confine light at resonant wavelengths by total internal reflection at curved boundaries. Resonance requires modes constructively interfere after circulating through the structure, such that the resonant wavelength (λ_{WGM}) satisfies the following relation for a circumferential WGM.

$$\lambda_{WGM} = \frac{2\pi r}{m} n_{eff}$$

Eq. 1-5

where r is the radius of the resonator, n_{eff} is the effective refractive index of the waveguide, and m is an integer specifying the mode number. Light is confined within the structure by the lower refractive index (RI) material at the surface of the cavity, however a portion of the mode extends outside the resonator as an evanescent wave, decaying in intensity exponentially with distance. n_{eff} is therefore a weighted average of the RI of the waveguide as well as the exterior material. Changes in the RI of an interface layer coating the resonator surface causes shifts in λ_{WGM}. WGM sensors have been used extensively for detecting biological components in liquid phase and for detecting changes in liquid bulk RI [145-151], but only rarely in gas phase applications [99, 111].

The OFRR is a section of thin-walled glass capillary of circular cross section, in which the wall serves as the optical waveguide and resonator, and the interior serves as a fluidic channel

[136-144, 152]. WGM modes in the visible and near-IR ranges can be launched in the OFRR by placing a tapered fiber-optic probe orthogonally against the outer wall. The (laser) light couples into the OFRR and resonances with Q factors as high as 10^6 can be produced at numerous closely spaced wavelengths [136]. Figure 1-8 illustrates a cross-section of an OFRR and the basic operating principle. The radial distribution of the electric field in the cylindrical OFRR is described by the solutions of Maxwell's equations in adherence with the boundary conditions imposed by the OFRR wall thickness and the depth and optical properties of any interface layer.

$$E_m(r) = \begin{cases} AJ_m(kr) & r \geq R \\ BJ_m(kn_{glass}r) + CH_m^{(1)}(kkn_{glass}r) & R \geq r \geq R - t \\ DJ_m(kn_{IntLayer}r) + EH_m^{(1)}(kkn_{IntLayer}r) & R - t \geq r \geq R - (t + d) \\ FH_m^{(1)}(kr) & R - (t + d) \geq r \end{cases} \qquad \text{Eq. 1-6}$$

$$n_{eff} = [n_{IntLayer}\eta_{IntLayer} + \eta_{Air} + n_{Glass}(1 - \eta_{IntLayer} - \eta_{Air})] \quad \text{Eq. 1-7}$$

Equation 1-6 describes the boundary conditions for a device with outer radius R, OFRR wall thickness t, and an internal interface layer of thickness d. Here J_m and H_m are the mth Bessel and Hankel functions of the first kind, and the refractive index of the surrounding air is approximated as 1. The field has resonant solutions at λ_{WGM} given by equation 1-5 for an n_{eff} described by equation 1-6 [153]. η is the proportion of the field in the interface layer, glass wall and surrounding air as designated, which is largely determined by the OFRR wall thickness. Thinner walls force the optical mode to protrude further into the interior and exterior. Changes in the resonant wavelength ($\Delta\lambda_{WGM}$) arise from changes in $n_{IntLayer}$ due to analyte sorption or immobilization at the interface layer, or changes in $\eta_{IntLayer}$ due to changes in interface layer thickness.

X. Fan et al. pioneered OFRR sensors produced by drawing a capillary pre-form under heat

and tension and then further reducing the wall thickness by etching with dilute HF [136-140]. These devices exhibit exceptionally high Q-factors and have been used for detecting biomolecules [136] as well as VOCs [137-138, 140]. OFRRs used for gas phase detection are coated internally with a thin polymer film, VOC sorption into the film can change $n_{IntLayer}$ due to contributions from the analytes RI, and can increase $\eta_{IntLayer}$ due to polymer swelling, if the polymer film is sufficiently thin. Capillary-drawn OFRRs are also used as detectors for GC [138]. However, the drawn-capillary OFRRs reported to date are not well suited for integration in lab-on-a-chip microsystems. Drawn-capillary OFRRs are very fragile and manufactured serially, with high variation in length and wall thickness between devices, and minimizing wall thickness risks structural integrity. Interfacing with optical fiber probes is performed manually, and fluidic interconnections are cumbersome.

An alternative design has been produced by O.G. Schmidt et. al that relies on a strain-induced self-rolling process to create µOFRRs from dielectric bilayers with very thin (~200 nm) walls and small inner diameters (~10 µm) [141-144]. These structures have been successfully incorporated into lab-on-chip devices for liquid phase biological detection, showcasing the OFRR geometry for use in microsensors. However these devices suffer from comparatively low Q-factors (~100-1000), and the small dimensions make the devices unsuitable for flow rates required in µGC applications. Realizing the advantages of OFRR technology for µGC systems motivates the development of a microfabricated OFRR (µOFRR), with high Q-factors, precisely specified dimensions, thin walls, and robust structure.

1.2.6 Optical detection with nanoparticle films

Optical transducers provide new opportunities to pursue multi-variable sensing for improved VOC discrimination. Films of optical nanostructures exhibit wavelength-dependent

changes in optical absorption or RI at different probing wavelengths during exposure to VOCs. This provides a means to differentiate VOCs with the response from a single optical sensor. Potyrailo et al. demonstrated this phenomenom by examining the reflection spectra of morpho butterfly wings during VOC exposure [108]; analytes adsorbed to the surface of naturally occuring lamellar gratings on the wings and imparted spectral changes in reflectance as a function of analyte RI and affinity for the structure. A sensor pattern consisting of responses at just three discrete wavelengths was sufficient for discrimination between water, methanol and dichloroethylene, showing this approach ammenable for use in sensor arrays without requiring spectrophotometry.

Adaptation of this phenomenom for microsensors requires periodic, subwavelength structures that can be produced with specified dimensions and chemical properties, and can be integrated on substrates using existing coating techniques. Metal nanoparticles such as MPNs are an enticing candidate for this appliation: MPNs have been repeatedly demonstrated as interface layers for VOC microsensor arrays, they can be synthesized with control of particle size, spacing, and thiolate moeity, and they exhibit a property known as localized surface plasmon resonance (LSPR) frequently exploited for detecting biological [154-156] and VOC analytes [105, 157-161]. Density waves in the surface electrons of nanoparticles can be excited by visible wavelength, and resonate at a frequency determined by particle geometry (size and shape), free electron density, and the dielectric properties of the surrounding medium.

$$\varepsilon_m = \varepsilon_b(\omega) + \frac{\omega_p{}^2}{\omega(\omega+i\gamma)} - \frac{\omega_p{}^2}{\omega(\omega+i\gamma+\frac{iv_f}{r})} \qquad \text{Eq. 1-8}$$

Equation 1-4 [162-163] provides the adjusted complex permittivity of gold nanoparticles exhibiting LSPR, where ε_b is the permittivity of bulk gold at a given optical frequency, ω_p is the plasma frequency in bulk gold, γ is the damping constant in the free-electron Drude model, v_f is

the fermi velocity and r is the particle radius. For sparse films, or for nanoparticles suspended in solvents, bulk optical characteristics such as RI or absorbance can be calculated from $\varepsilon_m(\omega)$ by two known methods [164]: an effective medium approximation such as Maxwell-Garnett, or the Clausius-Mossotti equation can be solved with dipole polarizability of the nanoparticle inclusions calculated from Mie theory [165].

However, for MPN films which can easily have nanoparticle volume fractions of greater than 20% [166] the assumptions upon which these models rely are violated. In this 'dense' regime the plasmon resonance is strongly coupled between nanoparticles, and optical properties are strongly dependent on inter-particle spacing. Experiments on dense films with spacing mediated by DNA-linkers reveal that the LSPR absorption maximum (λ_{LSPR}) blue-shifts with increased spacing, while peak width broadens with increased polydispersity [167]. Computational methods known as direct dipole approximations (DDA) have been used to model the LSPR spectra for such dense films, and reveal that changes in total absorbance and resonant wavelength (λ_{LSPR}) arise from changes in RI of the inter-particle medium [168].

VOC sorption into MPN films is known to cause both volumetric swelling and changes in the dielectric properties (and thus the RI) in the thiolate-linker meshing that comprises the interparticle medium [106]. Multi-wavelength measurements of MPN interface layers should provide information on VOC RI, partition coeffecient, and polariziability arising from each property's contribution to changes in LSPR. Additionally, the response dependence on nanoparticle size, spacing, and thiolate RI provides a large field of controllable variables that could be potentially tuned to enhance response diveristy, and therefore selectivity, among numerous analytes and their mixture in optical microsensors.

As described, considerable effort has been expended to develop sensitive and selective microsensors for VOC detection, yet over the past four decades only a few have found use in μGC applications, and of these there persist major problems with limited response selectivity, high LODs and slow response times. This dissertation describes our efforts to solve these problems through multi-transducer and multi-variable arrays. This research includes the development of the first microfabricated OFRR structures and sensors, as well as the successful integration of these devices with an upstream μGC column and μGC × μGC subsystem. Additionally this work tests and confirms the hypothesis that a single MPN film can discriminate VOCs by dint of optical response at multiple wavelengths, and ultimately demonstrates the inclusion of an MPN film on a μOFRR sensor, providing a platform for the development of a highly sensitive and highly selective μGC detector.

1.3 References

1 . Thermo Scientific, Infared Analyzer, MIRAN SapphIRe, http://www.thermoscientific.com/content/tfs/en/product/miran-sapphire-portable-ambient-analyzers-1.html, accessed November 9th 2014
2 . GASMET DX4040 Portable FTIR, Quantitech, http://www.quantitech.co.uk/entity214-GASMET-DX4040-Portable-FTIR-Ambient-Air-FTIR-Gas-analyser.aspx, accessed November 9th 2014
3 . HazMatID360, Smiths Detection, http://www.smithsdetection.com/chemical-identification/57-chemical-identification/hazmatid-360.html#.VGAAL_nF84k, accessed November 9th 2014
4 . I. Cotte-Rodríguez and R. G. Cooks, *Chemical Communications* **2006**, 2968-2970.
5 . L. Gao, A. Sugiarto, J. D. Harper, R. G. Cooks and Z. Ouyang, *Analytical Chemistry* **2008**, *80*, 7198-7205.
6 . P. I. Hendricks, J. K. Dalgleish, J. T. Shelley, M. A. Kirleis, M. T. McNicholas, L. Li, T.-C. Chen, C.-H. Chen, J. S. Duncan and F. Boudreau, *Analytical chemistry* **2014**, *86*, 2900-2908.
7 . A. Keil, H. Hernandez-Soto, R. J. Noll, M. Fico, L. Gao, Z. Ouyang and R. G. Cooks, *Analytical Chemistry* **2008**, *80*, 734-741.
8 . C. C. Mulligan, D. R. Justes, R. J. Noll, N. L. Sanders, B. C. Laughlin and R. G. Cooks, *Analyst* **2006**, *131*, 556-567.

9 .   G. Huang, W. Xu, M. A. Visbal-Onufrak, Z. Ouyang and R. G. Cooks, *Analyst* **2010**, *135*, 705-711.

10 .   J. A. Syage, B. J. Nies, M. D. Evans and K. A. Hanold, *Journal of the American Society for Mass Spectrometry* **2001**, *12*, 648-655.

11 .   L. Whalley, A. Lewis, J. McQuaid, R. Purvis, J. Lee, K. Stemmler, C. Zellweger and P. Ridgeon, *Journal of Environmental Monitoring* **2004**, *6*, 234-241.

12 .   W. R. Collin, G. Serrano, L. K. Wright, H. Chang, N. Nuñovero and E. T. Zellers, *Analytical Chemistry* **2013**, *86*, 655-663.

13 .   R.-S. Jian, Y.-S. Huang, S.-L. Lai, L.-Y. Sung and C.-J. Lu, *Microchemical Journal* **2013**, *108*, 161-167.

14 .   S. K. Kim, H. Chang and E. T. Zellers, *Analytical chemistry* **2011**, *83*, 7198-7206.

15 .   P. R. Lewis, R. P. Manginell, D. R. Adkins, R. J. Kottenstette, D. R. Wheeler, S. S. Sokolowski, D. E. Trudell, J. E. Byrnes, M. Okandan and J. M. Bauer, *Sensors Journal, IEEE* **2006**, *6*, 784-795.

16 .   J. Liu, N. K. Gupta, K. D. Wise, Y. B. Gianchandani and X. Fan, *Lab on a Chip* **2011**, *11*, 3487-3492.

17 .   C.-J. Lu, W. H. Steinecker, W.-C. Tian, M. C. Oborny, J. M. Nichols, M. Agah, J. A. Potkay, H. K. Chan, J. Driscoll and R. D. Sacks, *Lab on a Chip* **2005**, *5*, 1123-1131.

18 .   C.-J. Lu, J. Whiting, R. D. Sacks and E. T. Zellers, *Analytical chemistry* **2003**, *75*, 1400-1409.

19 .   R. P. Manginell, J. M. Bauer, M. W. Moorman, L. J. Sanchez, J. M. Anderson, J. J. Whiting, D. A. Porter, D. Copic and K. E. Achyuthan, *Sensors* **2011**, *11*, 6517-6532.

20 .   S. C. Terry, J. H. Jerman and J. B. Angell, *Electron Devices, IEEE Transactions on* **1979**, *26*, 1880-1886.

21 .   Q. Zhong, W. H. Steinecker and E. T. Zellers, *Analyst* **2009**, *134*, 283-293.

22 .   D. R. Adkins and P. R. Lewis, *SPIE Defense, Security, and Sensing* **2009**, pp. 73040S-73040S-73010.

23 .   S. Zampolli, I. Elmi, F. Mancarella, P. Betti, E. Dalcanale, G. Cardinali and M. Severi, *Sensors and Actuators B: Chemical* **2009**, *141*, 322-328.

24 .   490 Micro-GC, Agilent Technologies, http://www.chem.agilent.com/en-US/products-services/Instruments-Systems/Gas-Chromatography/490-Micro-GC/Pages/default.aspx, accessed November 9 2014

25 .   Explorer, INFICON, http://products.inficon.com/en-us/nav-products/Product/Detail/Explorer-Portable-Gas-Chromatograph?path=Products%2Fpg-ChemicalDetection%2F, accessed November 9th 2014

26 .   TRIDION-9, Torion, http://torion.com/products/tridion.html, accessed November 9th 2014

27 .   VOC-Analyzer 200, GmbH, http://www.iut-berlin.info/229.0.html?&L=1, accessed November 9 2014

28 .   http://www.defiant-tech.com/, accessed November 9th 2014

29 .   S. R. DiNardi and A. I. H. Association, *The Occupational Environment: Its evaluation, control, and management*, AIHA Press (American Industrial Hygiene Association), **2003**,

30 .   C. Charlton, F. De Melas, A. Inberg, N. Croitoru and B. Mizaikoff, *IEE Proceedings-Optoelectronics* **2003**, *150*, 306-309.

31 .   R. A. Miller, E. G. Nazarov, G. A. Eiceman and A. Thomas King, *Sensors and Actuators A: Physical* **2001**, *91*, 301-312.

32 . T. Sikanen, S. Franssila, T. J. Kauppila, R. Kostiainen, T. Kotiaho and R. A. Ketola, *Mass spectrometry reviews* **2010**, *29*, 351-391.

33 . R. Syms, *Analytical and bioanalytical chemistry* **2009**, *393*, 427-429.

34 . E. Wapelhorst, J.-P. Hauschild and J. Müller, *Sensors and Actuators A: Physical* **2007**, *138*, 22-27.

35 . J. R. Askim, M. Mahmoudi and K. S. Suslick, *Chemical Society Reviews* **2013**, *42*, 8649-8682.

36 . F. I. Bohrer, E. Covington, C. a. Kurdak and E. T. Zellers, *Analytical chemistry* **2011**, *83*, 3687-3695.

37 . Q.-Y. Cai and E. T. Zellers, *Analytical chemistry* **2002**, *74*, 3533-3539.

38 . J. W. Grate, *Chemical reviews* **2000**, *100*, 2627-2648.

39 . M.-D. Hsieh and E. T. Zellers, *Journal of occupational and environmental hygiene* **2004**, *1*, 149-160.

40 . R.-S. Jian, R.-X. Huang and C.-J. Lu, *Talanta* **2012**, *88*, 160-167.

41 . G. Konvalina and H. Haick, *Accounts of chemical research* **2013**, *47*, 66-76.

42 . M. Li, E. Myers, H. Tang, S. Aldridge, H. McCaig, J. Whiting, R. Simonson, N. Lewis and M. Roukes, *Nano letters* **2010**, *10*, 3899-3903.

43 . K. Reddy, Y. Guo, J. Liu, W. Lee, M. K. Khaing Oo and X. Fan, *Sensors and Actuators B: Chemical* **2011**, *159*, 60-65.

44 . K. Reddy, Y. Guo, J. Liu, W. Lee, M. K. K. Oo and X. Fan, *Lab on a Chip* **2012**, *12*, 901-905.

45 . W. H. Steinecker, S. K. Kim, F. I. Bohrer, L. Farina, Ç. Kurdak and E. T. Zellers, *Sensors Journal, IEEE* **2011**, *11*, 469-480.

46 . A. D. Wilson and M. Baietto, *Sensors* **2011**, *11*, 1105-1176.

47 . A. Hierlemann, E. T. Zellers and A. J. Ricco, *Analytical chemistry* **2001**, *73*, 3458-3466.

48 . F. Röck, N. Barsan and U. Weimar, *Chemical reviews* **2008**, *108*, 705-725.

49 . M.-D. Hsieh and E. T. Zellers, *Analytical chemistry* **2004**, *76*, 1885-1895.

50 . J. Park, W. A. Groves and E. T. Zellers, *Analytical chemistry* **1999**, *71*, 3877-3886.

51 . M. Penza and G. Cassano, *Sen. and Act. B* **2003**, *89*, 269-284.

52 . A. J. Ricco, R. M. Crooks and G. C. Osbourn, *Accounts of chemical research* **1998**, *31*, 289-296.

53 . L. R. Senesac, P. Dutta, P. G. Datskos and M. J. Sepaniak, *Analytica Chimica Acta* **2006**, *558*, 94-101.

54 . C. Jin, P. Kurzawski, A. Hierlemann and E. T. Zellers, *Analytical Chemistry* **2008**, *80*, 227-236.

55 . G. C. Frye-Mason, R. J. Kottenstette, E. J. Heller, C. M. Matzke, S. A. Casalnuovo, P. R. Lewis, R. P. Manginell, W. K. Schubert, V. M. Hietala and R. J. Shul, *Micro Total Analysis Systems' 98* **1998**, pp. 477-481.

56 . Y. Tang, J. Yeom, J. Han, B. Bae, R. Masel and M. Shannon, *Proceedings of Micro Total Analysis Systems Workshop* **2005**.

57 . B. Bae, J. Yeom, A. D. Radadia, R. I. Masel and M. A. Shannon, *Solid-State Sensors, Actuators and Microsystems Conference, 2007. TRANSDUCERS 2007. International* **2007**, pp. 1497-1500.

58 . A. D. Radadia, R. I. Masel and M. A. Shannon, *Solid-State Sensors, Actuators and Microsystems Conference, 2007. TRANSDUCERS 2007. International* **2007**, pp. 2011-2014.

59 . J. Yeom, C. R. Field, B. Bae, R. I. Masel and M. A. Shannon, *Journal of Micromechanics and Microengineering* **2008**, *18*, 125001.

60 . E. Zellers, G. Serrano, H. Chang and L. Amos, *Solid-State Sensors, Actuators and Microsystems Conference (TRANSDUCERS), 2011 16th International* **2011**, pp. 2082-2085.

61 . J. Dallüge, J. Beens and U. A. T. Brinkman, *Journal of Chromatography A* **2003**, *1000*, 69-108.

62 . J. V. Seeley, F. Kramp and C. J. Hicks, *Analytical chemistry* **2000**, *72*, 4346-4352.

63 . R. E. Mohler, B. J. Prazen and R. E. Synovec, *Analytica chimica acta* **2006**, *555*, 68-74.

64 . J. B. Phillips, R. B. Gaines, J. Blomberg, F. W. van der Wielen, J. M. Dimandja, V. Green, J. Granger, D. Patterson, L. Racovalis and H. J. de Geus, *Journal of High Resolution Chromatography* **1999**, *22*, 3-10.

65 . M. Libardoni, C. Fix, J. H. Waite and R. Sacks, *Analytical Methods* **2010**, *2*, 936-943.

66 . G. Serrano, D. Paul, S.-J. Kim, K. Kurabayashi and E. T. Zellers, *Analytical Chemistry* **2012**, *84*, 6973-6980.

67 . S.-J. Kim, G. Serrano, K. D. Wise, K. Kurabayashi and E. T. Zellers, *Analytical Chemistry* **2011**, *83*, 5556-5562.

68 . E. Camara, P. Breuil, D. Briand, L. Guillot, C. Pijolat and N. de Rooij, *Sensors and Actuators B: Chemical* **2010**, *148*, 610-619.

69 . M. Kim and S. Mitra, *Journal of Chromatography A* **2003**, *996*, 1-11.

70 . C. J. Lu and E. T. Zellers, *Analyst* **2002**, *127*, 1061-1068.

71 . C.-J. Lu and E. T. Zellers, *Analytical chemistry* **2001**, *73*, 3449-3457.

72 . R. P. Manginell, D. R. Adkins, M. W. Moorman, R. Hadizadeh, D. Copic, D. A. Porter, J. M. Anderson, V. M. Hietala, J. R. Bryan and D. R. Wheeler, *Microelectromechanical Systems, Journal of* **2008**, *17*, 1396-1407.

73 . W.-C. Tian, H. K. Chan, C.-J. Lu, S. W. Pang and E. T. Zellers, *Microelectromechanical Systems, Journal of* **2005**, *14*, 498-507.

74 . W.-C. Tian, S. W. Pang, C.-J. Lu and E. T. Zellers, *Microelectromechanical Systems, Journal of* **2003**, *12*, 264-272.

75 . I. Voiculescu, R. A. McGill, M. E. Zaghloul, D. Mott, J. Stepnowski, S. Stepnowski, H. Summers, V. Nguyen, S. Ross and K. Walsh, *Sensors Journal, IEEE* **2006**, *6*, 1094-1104.

76 . E. T. Zellers, M. Morishita and Q.-Y. Cai, *Sensors and Actuators B: Chemical* **2000**, *67*, 244-253.

77 . M. Agah, J. A. Potkay, G. Lambertus, R. Sacks and K. D. Wise, *Microelectromechanical Systems, Journal of* **2005**, *14*, 1039-1050.

78 . S. Ali, M. Ashraf-Khorassani, L. T. Taylor and M. Agah, *Sensors and Actuators B: Chemical* **2009**, *141*, 309-315.

79 . A. Bhushan, D. Yemane, D. Trudell, E. B. Overton and J. Goettert, *Microsystem technologies* **2007**, *13*, 361-368.

80 . D. Gaddes, J. Westland, F. L. Dorman and S. Tadigadapa, *Journal of Chromatography A* **2014**, *1349*, 96-104.

81 . G. Lambertus, A. Elstro, K. Sensenig, J. Potkay, M. Agah, S. Scheuering, K. Wise, F. Dorman and R. Sacks, *Analytical chemistry* **2004**, *76*, 2629-2637.

82 . H.-s. Noh, P. J. Hesketh and G. C. Frye-Mason, *Microelectromechanical Systems, Journal of* **2002**, *11*, 718-725.

83 . J. A. Potkay, G. R. Lambertus, R. D. Sacks and K. D. Wise, *Microelectromechanical Systems, Journal of* **2007**, *16*, 1071-1079.

84 . A. D. Radadia, R. I. Masel, M. A. Shannon, J. P. Jerrell and K. R. Cadwallader, *Analytical chemistry* **2008**, *80*, 4087-4094.

85 . S. Reidy, G. Lambertus, J. Reece and R. Sacks, *Analytical chemistry* **2006**, *78*, 2623-2630.

86 . M. Stadermann, A. D. McBrady, B. Dick, V. R. Reid, A. Noy, R. E. Synovec and O. Bakajin, *Analytical chemistry* **2006**, *78*, 5639-5644.

87 . S. S. Bedair and G. K. Fedder, *Sensors, 2004. Proceedings of IEEE* **2004**, pp. 955-958.

88 . E. Covington, F. Bohrer, C. Xu, E. Zellers and C. Kurdak, *Lab on a Chip* **2010**, *10*, 3058-3060.

89 . J. Hatfield, P. Neaves, P. Hicks, K. Persaud and P. Travers, *Sensors and Actuators B: Chemical* **1994**, *18*, 221-228.

90 . H. Kim, A. A. Astle, K. Najafi, L. P. Bernal and P. D. Washabaugh, *Micro Electro Mechanical Systems, 2007. MEMS. IEEE 20th International Conference on* **2007**, pp. 131-134.

91 . S.-J. Kim, S. M. Reidy, B. P. Block, K. D. Wise, E. T. Zellers and K. Kurabayashi, *Lab on a Chip* **2010**, *10*, 1647-1654.

92 . G. S. Kulkarni, K. Reddy, Z. Zhong and X. Fan, *Nature communications* **2014**, *5*.

93 . C. Y. Lee, R. Sharma, A. D. Radadia, R. I. Masel and M. S. Strano, *Angewandte Chemie International Edition* **2008**, *47*, 5018-5021.

94 . S. Martin, G. Frye, J. Spates and M. Butler, *Ultrasonics Symposium, 1996. Proceedings., 1996 IEEE* **1996**, pp. 423-434.

95 . T. E. Mlsna, S. Cemalovic, M. Warburton, S. T. Hobson, D. A. Mlsna and S. V. Patel, *Sensors and Actuators B: Chemical* **2006**, *116*, 192-201.

96 . L. Wright and E. Zellers, *Analyst* **2013**, *138*, 6860-6868.

97 . S. Zimmermann, P. Krippner, A. Vogel and J. Müller, *Sensors and Actuators B: Chemical* **2002**, *83*, 285-289.

98 . R. A. Potyrailo and W. G. Morris, *Analytical Chemistry* **2007**, *79*, 45-51.

99 . A. Ksendzov, M. Homer and A. Manfreda, *Electronics Letters* **2004**, *40*, 63-65.

100 . M.-C. Tseng and Y.-H. Chu, *Chemical Communications* **2010**, *46*, 2983-2985.

101 . F. Hernandez-Ramirez, J. D. Prades, R. Jimenez-Diaz, T. Fischer, A. Romano-Rodriguez, S. Mathur and J. R. Morante, *Physical Chemistry Chemical Physics* **2009**, *11*, 7105-7110.

102 . A. Kolmakov, Y. Zhang, G. Cheng and M. Moskovits, *Advanced Materials* **2003**, *15*, 997-1000.

103 . D. C. Meier, S. Semancik, B. Button, E. Strelcov and A. Kolmakov, *Applied Physics Letters* **2007**, *91*, 063118.

104 . G. Sberveglieri, C. Baratto, E. Comini, G. Faglia, M. Ferroni, M. Pardo, A. Ponzoni and A. Vomiero, *Thin Solid Films* **2009**, *517*, 6156-6160.

105 . R. A. Potyrailo, M. Larsen and O. Riccobono, *Angewandte Chemie International Edition* **2013**, *52*, 10360-10364.

106 . W. H. Steinecker, M. P. Rowe and E. T. Zellers, *Analytical chemistry* **2007**, *79*, 4977-4986.

107 . B. R. Goldsmith, J. J. Mitala Jr, J. Josue, A. Castro, M. B. Lerner, T. H. Bayburt, S. M. Khamis, R. A. Jones, J. G. Brand and S. G. Sligar, *Acs Nano* **2011**, *5*, 5408-5416.

108 . R. A. Potyrailo, H. Ghiradella, A. Vertiatchikh, K. Dovidenko, J. R. Cournoyer and E. Olson, *Nature Photonics* **2007**, *1*, 123-128.

109 .   J. J. Lavigne and E. V. Anslyn, *Angewandte Chemie International Edition* **2001**, *40*, 3118-3130.

110 .   S. J. Patrash and E. T. Zellers, *Analytical chemistry* **1993**, *65*, 2055-2066.

111 .   N. A. Yebo, P. Lommens, Z. Hens and R. Baets, *Optics Express* **2010**, *18*, 11859-11866.

112 .   N. Barsan and U. Weimar, *Journal of Electroceramics* **2001**, *7*, 143-167.

113 .   A. P. Lee and B. J. Reedy, *Sensors and Actuators B: Chemical* **1999**, *60*, 35-42.

114 .   A. Fort, M. Gregorkiewitz, N. Machetti, S. Rocchi, B. Serrano, L. Tondi, N. Ulivieri, V. Vignoli, G. Faglia and E. Comini, *Thin Solid Films* **2002**, *418*, 2-8.

115 .   E. N. Dattoli, A. V. Davydov and K. D. Benkstein, *Nanoscale* **2012**, *4*, 1760-1769.

116 .   A. Vergara, E. Llobet, J. Brezmes, P. Ivanov, C. Cané, I. Gràcia, X. Vilanova and X. Correig, *Sensors and Actuators B: Chemical* **2007**, *123*, 1002-1016.

117 .   M. Fleischer, S. Kornely, T. Weh, J. Frank and H. Meixner, *Sensors and Actuators B: Chemical* **2000**, *69*, 205-210.

118 .   H. Wohltjen and A. W. Snow, *Analytical Chemistry* **1998**, *70*, 2856-2859.

119 .   M. P. Rowe, K. E. Plass, K. Kim, C. Kurdak, E. T. Zellers and A. J. Matzger, *Chemistry of materials* **2004**, *16*, 3513-3517.

120 .   N. Krasteva, Y. Fogel, R. E. Bauer, K. Müllen, Y. Joseph, N. Matsuzawa, A. Yasuda and T. Vossmeyer, *Advanced Functional Materials* **2007**, *17*, 881-888.

121 .   J. W. Grate, S. J. Martin and R. M. White, *Analytical Chemistry* **1993**, *65*, 940A-948A.

122 .   J. W. Grate, S. J. Martin and R. M. White, *Analytical Chemistry* **1993**, *65*, 987A-996A.

123 .   D. Ballantine Jr, R. M. White, S. J. Martin, A. J. Ricco, E. Zellers, G. Frye and H. Wohltjen, *Acoustic Wave Sensors: Theory, Design, & Physico-Chemical Applications*, Academic press, **1996**, p.

124 .   J. W. Grate and M. Klusty, *Analytical Chemistry* **1991**, *63*, 1719-1727.

125 .   J. W. Grate, S. J. Patrash and M. H. Abraham, *Analytical Chemistry* **1995**, *67*, 2162-2169.

126 .   J. W. Grate, B. M. Wise and M. H. Abraham, *Analytical Chemistry* **1999**, *71*, 4544-4553.

127 .   C. Jin and E. T. Zellers, *Analytical chemistry* **2008**, *80*, 7283-7293.

128 .   M. A. Sharaf, *Chemometrics*, John Wiley & Sons, **1986**, p.

129 .   E. T. Zellers, T.-S. Pan, S. J. Patrash, M. Han and S. A. Batterman, *Sensors and Actuators B: Chemical* **1993**, *12*, 123-133.

130 .   E. T. Zellers, J. Park, T. Hsu and W. A. Groves, *Analytical chemistry* **1998**, *70*, 4191-4201.

131 .   M. Haug, K. Schierbaum, G. Gauglitz and W. Göpel, *Sensors and Actuators B: Chemical* **1993**, *11*, 383-391.

132 .   J. Mitrovics, H. Ulmer, U. Weimar and W. Göpel, *Accounts of chemical research* **1998**, *31*, 307-315.

133 .   K. Schierbaum, A. Gerlach, M. Haug and W. Göpel, *Sensors and Actuators A: Physical* **1992**, *31*, 130-137.

134 .   P. Kurzawski, C. Hagleitner and A. Hierlemann, *Analytical chemistry* **2006**, *78*, 6910-6920.

135 .   F. Battiston, J.-P. Ramseyer, H. Lang, M. Baller, C. Gerber, J. Gimzewski, E. Meyer and H.-J. Güntherodt, *Sensors and Actuators B: Chemical* **2001**, *77*, 122-131.

136 .   X. Fan, I. M. White, H. Zhu, J. D. Suter and H. Oveys, *Proc. SPIE* **2007**, p. 64520M.

137 .   Y. Sun, J. Liu, G. Frye-Mason, S.-j. Ja, A. K. Thompson and X. Fan, *Analyst* **2009**, *134*, 1386-1391.

138 .   Y. Sun, J. Liu, D. J. Howard, G. Frye-Mason, A. K. Thompson, S.-j. Ja and X. Fan, *Analyst* **2010**, *135*, 165-171.

139 . I. M. White, H. Oveys and X. Fan, *Optics Letters* **2006**, *31*, 1319-1321.

140 . Y. Sun, S. I. Shopova, G. Frye-Mason and X. Fan, *Optics letters* **2008**, *33*, 788-790.

141 . E. J. Smith, S. Schulze, S. Kiravittaya, Y. Mei, S. Sanchez and O. G. Schmidt, *Nano letters* **2010**, *11*, 4037-4042.

142 . A. Bernardi, S. Kiravittaya, A. Rastelli, R. Songmuang, D. Thurmer, M. Benyoucef and O. Schmidt, *Applied Physics Letters* **2008**, *93*, 094106.

143 . G. Huang, V. A. Bolaños Quiñones, F. Ding, S. Kiravittaya, Y. Mei and O. G. Schmidt, *Acs Nano* **2010**, *4*, 3123-3130.

144 . S. M. Harazim, V. A. B. Quiñones, S. Kiravittaya, S. Sanchez and O. G. Schmidt, *Lab on a Chip* **2012**, *12*, 2649-2655.

145 . F. Vollmer and S. Arnold, *Nature methods* **2008**, *5*, 591-596.

146 . A. L. Washburn, L. C. Gunn and R. C. Bailey, *Analytical Chemistry* **2009**, *81*, 9499-9506.

147 . E. Krioukov, D. Klunder, A. Driessen, J. Greve and C. Otto, *Optics letters* **2002**, *27*, 512-514.

148 . J. H. Wade and R. C. Bailey, *Analytical chemistry* **2013**, *86*, 913-919.

149 . A. Schweinsberg, S. Hocdé, N. N. Lepeshkin, R. W. Boyd, C. Chase and J. E. Fajardo, *Sensors and Actuators B: Chemical* **2007**, *123*, 727-732.

150 . L. He, Ş. K. Özdemir, J. Zhu, W. Kim and L. Yang, *Nature nanotechnology* **2011**, *6*, 428-432.

151 . J. L. Nadeau, V. S. Ilchenko, D. Kossakovski, G. H. Bearman and L. Maleki, *High-Power Lasers and Applications* **2002**, pp. 172-180.

152 . M. Sumetsky, Y. Dulashko and R. Windeler, *Optics letters* **2010**, *35*, 898-900.

153 . Y. Sun and X. Fan, *Optics express* **2008**, *16*, 10254-10268.

154 . J. N. Anker, W. P. Hall, O. Lyandres, N. C. Shah, J. Zhao and R. P. Van Duyne, *Nature materials* **2008**, *7*, 442-453.

155 . A. D. McFarland and R. P. Van Duyne, *Nano letters* **2003**, *3*, 1057-1062.

156 . N. Nath and A. Chilkoti, *Analytical Chemistry* **2002**, *74*, 504-509.

157 . C.-S. Cheng, Y.-Q. Chen and C.-J. Lu, *Talanta* **2007**, *73*, 358-365.

158 . M. C. Dalfovo, R. C. Salvarezza and F. J. Ibañez, *Analytical chemistry* **2012**, *84*, 4886-4892.

159 . L. E. Kreno, J. T. Hupp and R. P. Van Duyne, *Analytical chemistry* **2010**, *82*, 8042-8046.

160 . T. Karakouz, A. Vaskevich and I. Rubinstein, *The Journal of Physical Chemistry B* **2008**, *112*, 14530-14538.

161 . F.-Y. Chen, W.-C. Chang, R.-S. Jian and C.-J. Lu, *Analytical chemistry* **2014**.

162 . W. T. Doyle, *Physical review B* **1989**, *39*, 9852.

163 . S. Kubo, A. Diaz, Y. Tang, T. S. Mayer, I. C. Khoo and T. E. Mallouk, *Nano letters* **2007**, *7*, 3418-3423.

164 . S. K. Ghosh and T. Pal, *Chemical Reviews* **2007**, *107*, 4797-4862.

165 . V. Myroshnychenko, J. Rodríguez-Fernández, I. Pastoriza-Santos, A. M. Funston, C. Novo, P. Mulvaney, L. M. Liz-Marzán and F. J. G. de Abajo, *Chemical Society Reviews* **2008**, *37*, 1792-1805.

166 . J. W. Grate, D. A. Nelson and R. Skaggs, *Analytical Chemistry* **2003**, *75*, 1868-1879.

167 . J. J. Storhoff, A. A. Lazarides, R. C. Mucic, C. A. Mirkin, R. L. Letsinger and G. C. Schatz, *Journal of the American Chemical Society* **2000**, *122*, 4640-4650.

168 . M. M. Miller and A. A. Lazarides, *The Journal of Physical Chemistry B* **2005**, *109*, 21556-21565.
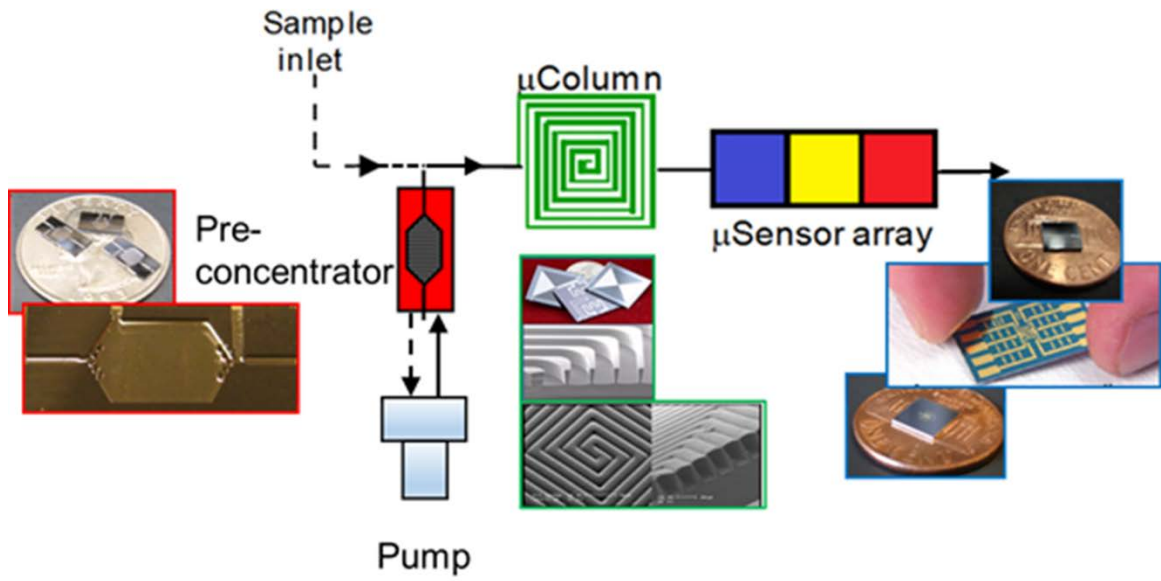
Figure 1-1. Cartoon illustrating typical layout and operation of a micro-scale gas chromatograph, with accompanying photographs of MEMS components. Dashed line show flow path during sampling, solid lines show flow path during backflushing.
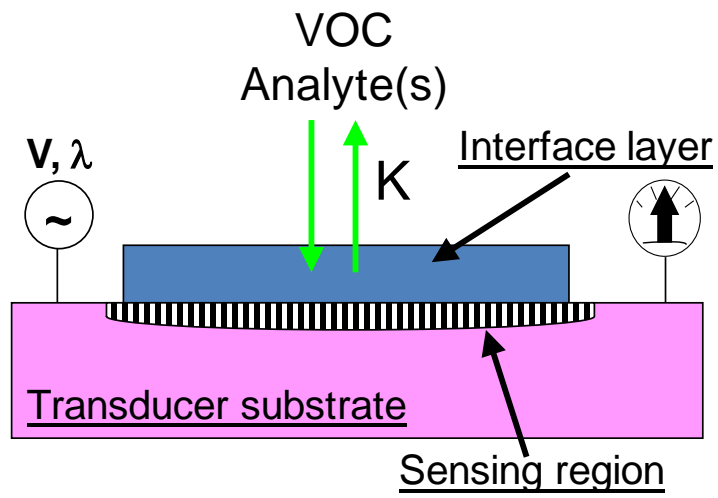
Figure 1-2. Cartoon illustrating archetypal microsensor, depicting VOC detection and transduction.
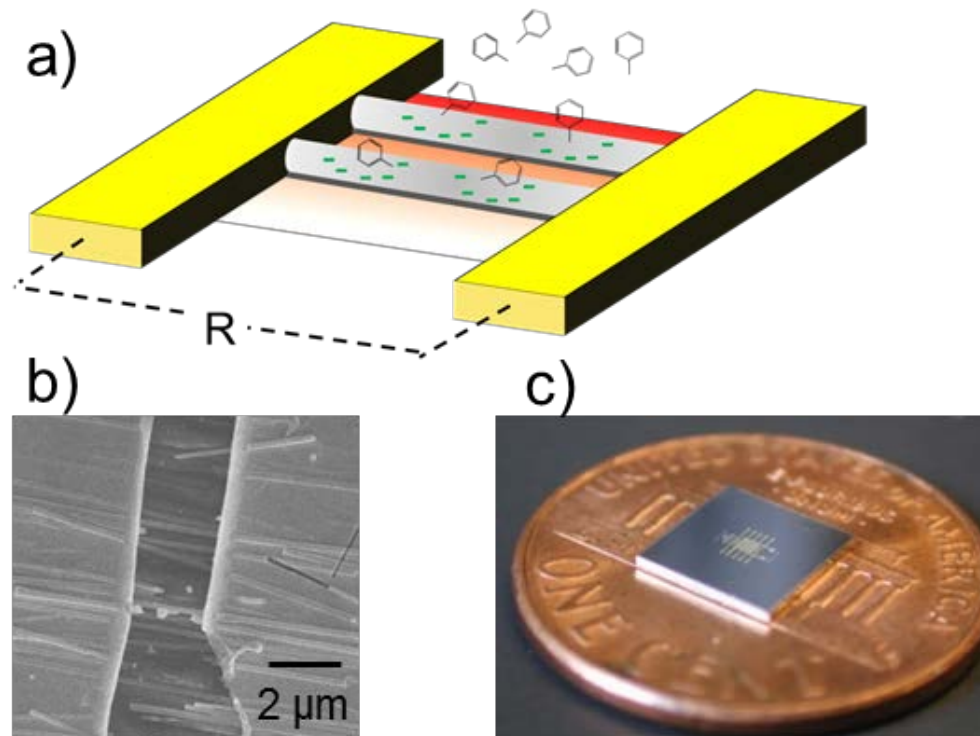
Figure 1-3. (a) Cartoon depicting basic design and operation of MOX nanowire sensor; (b) SEM of MOX nanowires spanning electrode contacts; (c) photograph of MOX microsensor with coin for scale.
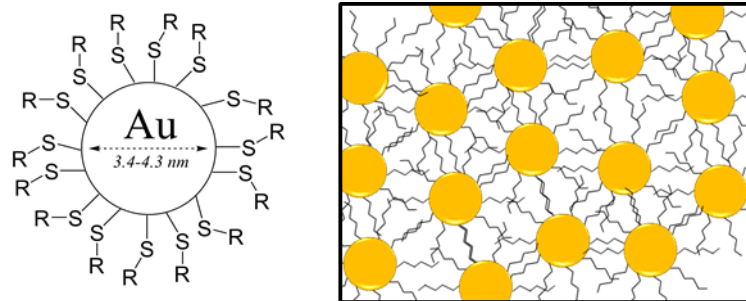
Figure 1-4. Diagram of thiolate-protected gold nanoparticle and illustration of MPN multi-layer film.
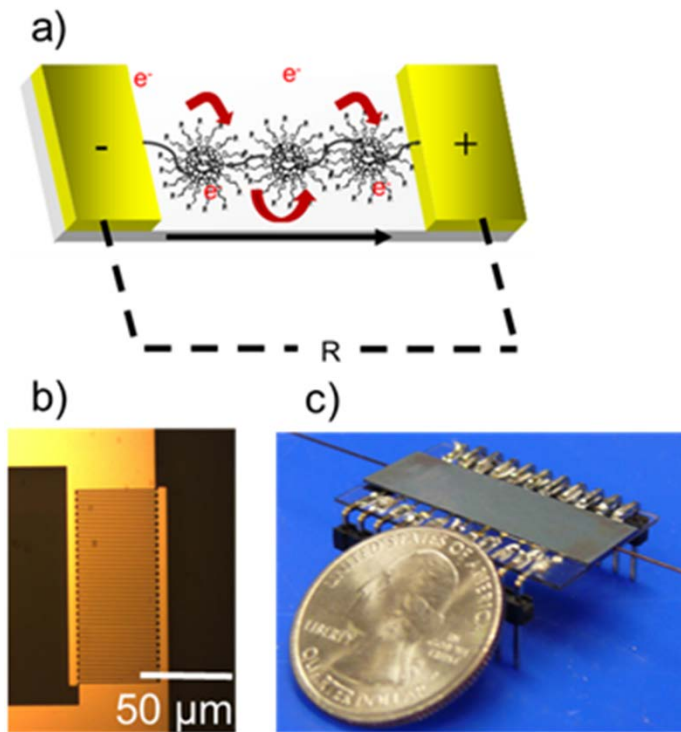
Figure 1-5. (a) Cartoon depicting operation of an MPN coated chemiresistor; (b) Microimage of interdigitated electrodes comprising a chemiresistor; (c) Photograph of packaged MPN chemiresistor sensor.
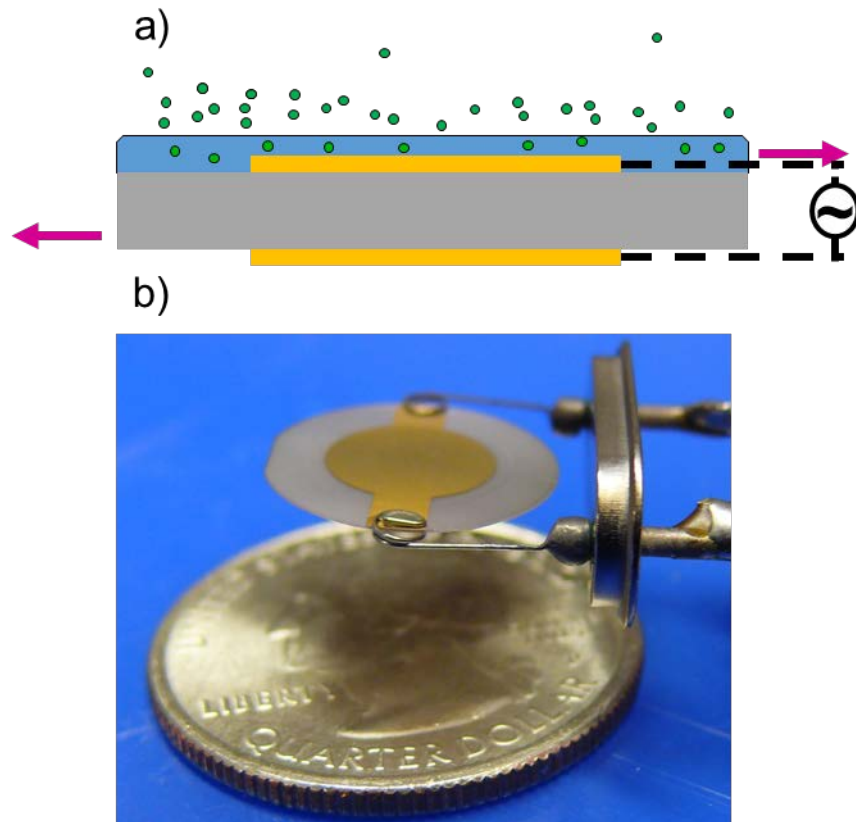
Figure 1-6. (a) Illustration of TSMR cross-section and operating principle; (b) photograph of TSMR fabricated from thin quart disc.
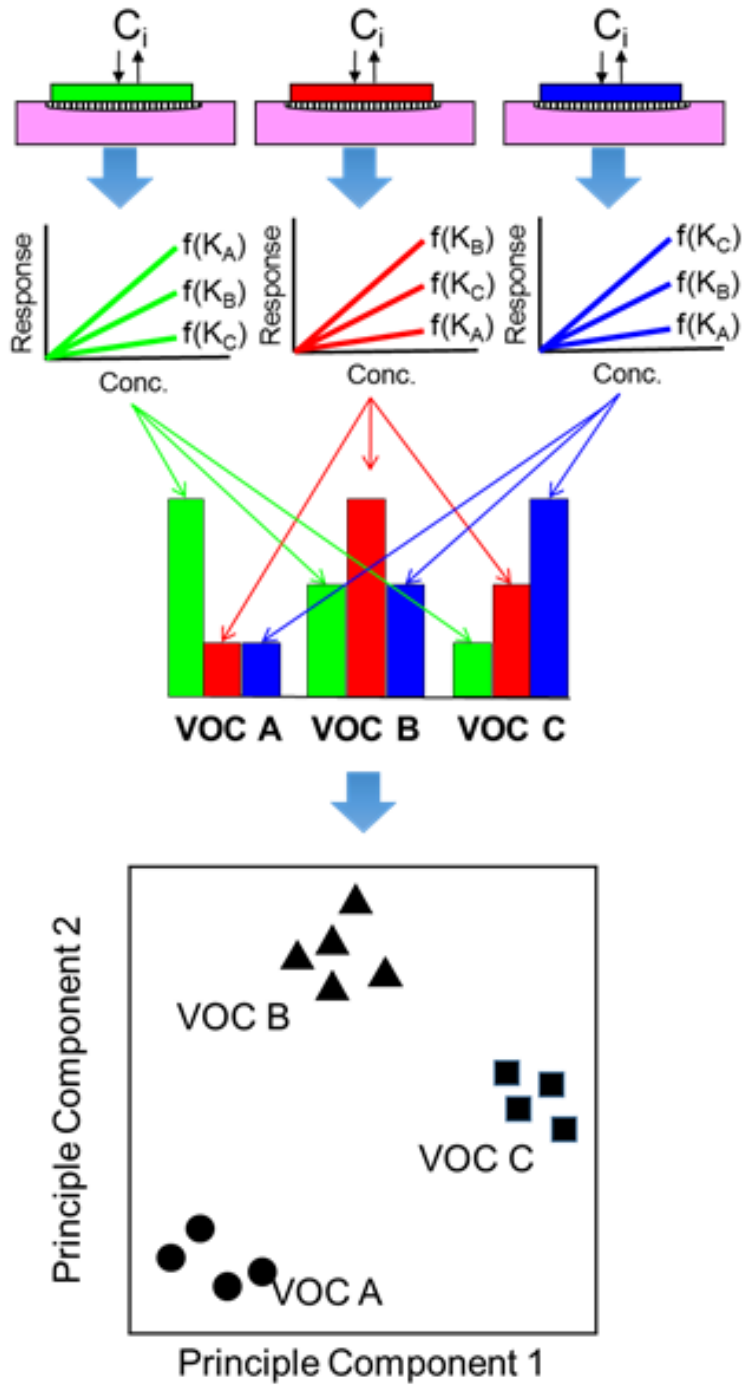
Figure 1-7. Diagram illustrating the transformation between sensor calibrations to sensor response pattern to principle component projection, using data from a multisensor array.
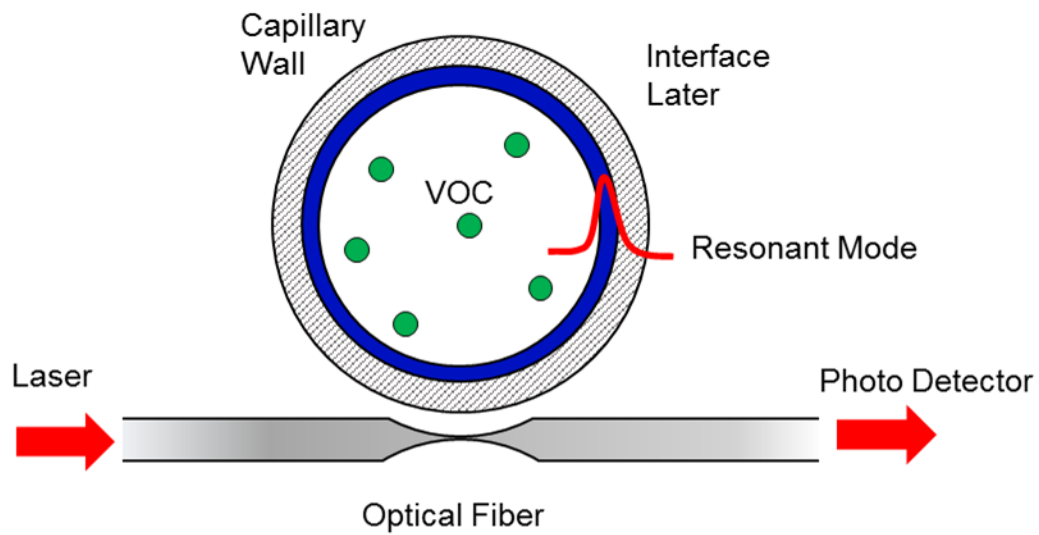
Figure 1-8. Illustration of OFRR cross section and typical operating configuration.

CHAPTER II

Organic Vapor Discrimination with Chemiresistor Arrays of Temperature Modulated Tin-Oxide Nanowires and Thiolate-Monolayer-Protected Gold Nanoparticles

2. 1 Introduction

Heated films of tin-oxide have been used in chemiresistors (CR) for gases and vapors for over 30 years; resistance changes accompanying analyte oxidation at the surface of the tin-oxide permit highly sensitive detection of a wide range of analytes [1]. Nanowires (NW) of tin-oxide have been reported to offer potentially improved sensitivity to gases and vapors by virtue of their high ratio of surface area to volume and improved degree of crystalline order [2-5]. Deposition of NWs onto micromachined hotplate platforms can yield low-power temperature-modulated NW-CR sensors with responses to different analytes that exhibit different temperature dependences [3, 6]. Although recent studies suggest that it should be possible to discriminate among a set of organic vapors by means of an array of as few as two such devices operated at different (elevated) temperatures [3-4, 6-8], this topic has not been addressed in published reports.

Thiolate-monolayer-protected Au nanoparticles (MPNs) have been studied as interface materials for CR vapor sensors over the past 12 years [9-15]. Vapor sorption into the organothiolate

monolayers surrounding the Au cores in a thin MPN film increases the average intercore distance, which reduces the rate of electron tunneling and generally increases the film resistance. If the dielectric constant of the vapor is significantly greater than that of the inter-core matrix, this factor will mitigate swelling-induced resistance changes [16-17]. An array of CRs with different MPN interface layers will exhibit partially selective responses whose pattern can be used to discriminate among individual vapors and the components of simple mixtures. Several reports have shown this capability using arrays of 2-4 sensors [11, 16, 18-19].

Since the mechanisms by which resistance changes arise in these two classes of sensors are completely different, it might be expected that an array of NW-CRs would provide relative responses to a set of analyte vapors that would complement those provided by an array of MPN-CRs. Thus, greater diversity and selectivity might be realized from a hybrid [NW+MPN]-CR array. The notion of combining sensors operating on the basis of different transduction or interactions mechanisms is not new [20-24], and recent studies of multi-transducer arrays of capacitive, calorimetric, and gravimetric sensors employing polymer interface layers suggest that some improvement in the diversity of responses to a set of vapors and their mixtures can be realized, relative to single-transducer arrays containing the same number of sensors [25-26] . As yet, however, no study has explored whether combining NW CRs with MPN CRs in hybrid arrays might yield improvements in vapor discrimination over that obtained with CR arrays employing one or the other type of interface material. The primary goal of the preliminary investigation described here was to test this hypothesis.

Toward that end, data were collected from a set of CRs coated with four different MPNs operated at ambient temperature and also from an NW-CR operated at two different (elevated) temperatures upon exposure to each of three individual vapors. The calibrated responses were then

pooled and the various actual and virtual arrays of 2-6 sensors were evaluated with regard to vapor discrimination. Monte Carlo simulations were used to iteratively generate synthetic responses by superimposing different levels of random error on the calibrated sensor responses, and then principal components regression analysis was used to estimate the rates of recognition (RR) achievable among the different possible arrays. Assessments were made of the diversity of responses exhibited using each type of interface material (i.e., NWs and MPNs) as well as the degree to which they complement each other in effecting vapor discrimination. For this study, tests were confined to differentiation among three individual vapors (i.e., no analyses of mixtures were performed).

2.2 Experimental methods

2.2.1 Devices and testing

The NW CR is a multi-layer structure in which a silicon oxynitride membrane supports a resistive heater electrically insulated from the top NW layer by another oxynitride layer (Figure 2-1a). First, the Ti-Pt resistive heater and temperature sensor were defined by a standard liftoff process on a 1-µm silicon oxynitride insulating layer pre-deposited on a Si substrate. A second 1-µm layer of silicon oxynitride was then deposited over the Ti-Pt structures, with contact pads subsequently exposed by an HF etch. Next, NWs fabricated as described previously [27], were transferred to the device surface as a mat of randomly oriented nanowires via contact printing [28]. Five pairs of Au contacts, 50 µm wide and separated by 2-4 µm, were lithographically defined and deposited on top of the NWs by a second liftoff process (Figure 2-1b). Finally, the backside of the Si substrate was subjected to deep reactive ion etching to yield a 2-µm thick suspended membrane

structure. Figure 2-1c shows the central region of a completed chip, with the five electrode pairs aligned horizontally over the membrane region.

Electrical connections were made by wire bonds and each device was mounted on a 20-pin ceramic header. Although devices could be heated to > 360 ºC, initial testing resulted in several device failures from stress-induced cracking of the membrane substrate upon cooling. The likely cause of this problem is the mismatch in thermal expansion of the heater metals and the underlying/overlying substrate layers arising from the fact that the metals were deposited at room temperature and not annealed. Subsequent tests were constrained to temperatures $\leq$ 360 ºC. It required 275 mW to heat the devices to 300 °C. Resistance was measured with a multimeter (34401A, Agilent Technologies, Palo Alto, CA) and, by convention, converted to conductance. Sensor responses are reported as the fractional change in conductance relative to the baseline value (i.e., $\Delta G/G$, or G_r). Only one device per chip was used for testing.

An array of eight MPN-CRs was created as described previously [29]. Cr-Au interdigital electrodes with 5-µm-wide fingers and spaces were deposited on a thick SiO_2 layer grown on a Si substrate. Pins were soldered to the bonding pads and the devices were plugged into sockets on a custom PC board that connected the devices to a voltage divider circuit. Interface layers were made by solvent casting films of MPNs having thiolate monolayers derived from n-octanethiol (C8), 4-(phenylethynyl)-benzenethiol (DPA), 6-phenoxyhexane-1-thiol (OPH), and methyl-6-mercaptohexanoate (HME) [30]. Two films of each type of MPN were deposited. The resistance was determined indirectly by measuring the voltage drop using a computer controlled DAQ card and a constant DC voltage source. By convention, sensor responses are reported as the fractional change in resistance (i.e., $\Delta R/R$, or R_r).

A single mounted NW CR was sealed in a 0.5-L glass chamber equipped with ports for electrical feedthroughs and gas flow. The MPN-CR array was sealed in a 0.5-L stainless steel chamber immediately upstream from the NW-CR chamber. The flow rate of the test-atmosphere through the chambers was 14 L/min. Nitromethane, n-hexane, and toluene were the analytes tested. Test atmospheres were generated by passing scrubbed air through fritted bubblers containing the (single) liquid analyte, followed by dilution with a metered scrubbed air stream. The flows were varied to span a range of concentrations, which differed for each analyte, but were within the range of 200 to 7,000 ppm (by volume). Vapor concentrations were confirmed by a calibrated flame ionization detector. Typical tests entailed exposure for 5-7 minutes followed by purging with clean air for a similar amount of time. Responses to n-hexane and toluene were collected simultaneously from the MPN-CR array and the NW CR over a 3-4-fold concentration range. Responses to nitromethane were collected in separate, sequential exposures to each type of sensor at two discrete concentrations for the NW CRs and over a 6-fold range for the MPN-CR array. The net change between the (average) pre-exposure baseline sensor signal under scrubbed air and the steady-state signal observed during vapor exposure was recorded.

2.2.2 Chemometrics

The performance of the various actual and virtual arrays was assessed using Monte Carlo simulations coupled with extended disjoint principal components regression (EDPCR) classification models. Using the experimental sensitivity values, synthetic MPN-CR responses to each vapor were generated by randomly selecting a vapor concentration within the range of 3-30×LOD, where the LOD was dictated by the least sensitive sensor in the array to ensure that all sensors are contributing to the response patterns. The response was calculated from the calibration-curve regression equation. Then error was introduced by adding to it a value obtained by

multiplying that response value by a factor derived from randomly sampling a Gaussian distribution with a mean of zero and a standard deviation of 0.05, 0.10, or 0.15, corresponding to random sensitivity errors (ε) of 5-15% of the response. The error enhanced responses from all sensors were combined and the location of the resulting response vector was projected onto the principal component corresponding to the original calibrations for each vapor via EDPCR. The identity of the vapor assigned to this synthetic response vector was determined by the shortest Euclidean distance. This procedure was performed iteratively (i.e., 1000 samples) to yield a statistical estimate of recognition rate (RR) for each array at each level of ε. Details of this methodology as applied to sensor-array evaluations can be found elsewhere [25-26, 31-32] .

For the (virtual) dual NW-CR array, the ratio of normalized responses at the two different temperatures was treated as a single response variable. However, error was superimposed on each response separately, as above, to produce the error-enhanced ratio. Since the NW-CR response ratio is independent of concentration (see below), it was not necessary to vary the concentration when generating the population of error enhanced responses. Assigning a vapor identity to the synthetic NW-CR array responses was based merely on how close the value of the synthetic ratio was to the true (i.e., calibrated) ratio.

For assigning vapor identities to synthetic responses generated from a hybrid array, the sum of the normalized distances between the error-enhanced synthetic response vector and each of the corresponding calibrated response vectors for the sensors under consideration (i.e., the response ratio for the NW-CR array and the principal component for the MPN-CR array) was calculated. As above, the synthetic response was assigned to the vapor for which this sum was the smallest.

2.3 Results and discussions

2.3.1 Sensor performance

The baseline conductance varied significantly among the tested NW-CR devices, ranging from 0.005-1 µS at 215 °C. This variation undoubtedly arises from device-to-device variations in the number of NWs involved in charge conduction between the CR electrodes. The observed temperature dependence of baseline conductance is similar to that in previous reports [33], with conductance increasing sharply with increasing temperature (data not shown).

Initial testing characterized the temperature dependence of the NW-CR vapor sensitivity to nitromethane. Two NW CRs were exposed to nitromethane vapors at discrete operating temperatures ranging from 170°C to 360 °C. The exposure concentration was 240 ppm for the first device and was inadvertently increased to 360 ppm for the other. NW-CR responses achieved steady state within ~20 seconds of the initial response at all temperatures. Recoveries required up to 5 minutes to reach the pre-exposure baseline, which is consistent with other reports [3,5]. The sensitivity exhibits a non-linear temperature dependence and passes through a maximum at ~280 °C for both devices (Figure 2-2a). Although the raw sensitivities differ significantly between the two devices, by normalizing the response at any temperature to that at the temperature of maximum sensitivity (i.e., 280 °C for device A and 285 °C for device B), the temperature dependent sensitivities of the two devices are nearly superimposable, as shown in Figure 2-2b. This is not surprising, because the deposition process creates a stochastic distribution of nanowires (size and number) carrying current in each bridge. By the same token, the ratio of responses of a given device at two different temperatures is a useful metric for comparing vapor responses across devices, because it corrects for inherent differences in the mobilities and number of charge carriers in each device. Therefore, all subsequent NW-CR vapor exposures were performed at the

temperatures at which the lowest and highest responses to nitromethane were observed, i.e., 215 °C and 280 °C.

Figure 2-3a and b show the NW-CR responses to n-hexane and toluene, respectively, over a range of concentrations at 215 and 280 °C. Although the response is greater at the higher temperature for any given concentration, the ratio of responses at the two different operating temperatures for a given vapor is nearly constant over the entire range of concentrations. Notably, however, the ratio differs between the two vapors: for toluene, the ratio of G_r values is 0.85 ± 0.05 and that for n-hexane is 0.72 ± 0.04. For nitromethane, a G_r ratio of 0.31 was obtained at 240 ppm from the data presented in Figure 2-2a for the same two temperatures. Thus, it is possible to differentiate the vapors on the basis of the response ratio over the concentration range tested.

Note that while the signal-to-noise ratios (G_r) are quite high, the slope sensitivities are relatively low over the concentration ranges measured for both of these vapors at both temperatures, and the concentration resolution at any given temperature(s) is relatively low. Although it is apparent from the plots that these curves will become non-linear at lower concentrations, with corresponding increases in slope sensitivity (i.e., resolution), as the concentrations decrease the responses at the different temperatures will converge and the ratios will approach unity. Thus, there will be a limit to the concentration range over which discrimination on the basis of temperature-dependent response ratios will be possible (this range was not determined in this study).

Responses from the array of MPN CRs to the same three vapors were rapid and reversible, and varied linearly with concentration (linear regression r^2 values with forced zero y-intercepts are all > 0.97), consistent with previous reports [16]. Response and recovery times were ≤ 20 sec in all cases. The sensitivities derived from the responses of the two CRs coated with a given MPN

differed by < 10% and were averaged for subsequent analyses. For n-hexane and toluene MPN-CR and NW-CR measurements were collected simultaneously. Sensors were exposed twice at each concentration to gather temperature dependent NW-CR data. Since the duplicate MPN-CR sensor responses differed by < 7%, the average values were used.

Figure 2-4 presents a series of bar charts that summarize the relevant response data. For the NW-CR array, the bars represent the relative sensitivities (G_r) at each test temperature for each vapor, normalized to the high-temperature G_r value. For the MPN-CR array the bars represent the relative sensitivities (R_r/ppm) normalized to the sensor with the highest sensitivity for each vapor.

2.3.2 Sensor array analysis

In order to compare the performance of different arrays properly, the number of sensors in each array must be the same. Since we are using the ratio of two NW CRs, in order to compare the vapor discrimination capabilities of this NW-CR array to those of the MPN CRs, it is necessary to restrict the number of MPN CRs in any array considered to two. Among the set of four MPN CRs, there are six possible dual-MPN-CR arrays, all of which were considered in succession.

Results of the Monte Carlo/EDPCR analyses, shown in Table 2-1, reveal that the NW-CR array ranks fourth among the seven possible dual-sensor arrays in terms of RR. For $\varepsilon = 5\%$, the RR for the NW-CR array is 91.5%, compared to an RR of 99.9% for the dual MPN-CR array that used coatings of DPA and HME (best performance) and an RR of only 75.9% for the MPN-CR array that used coatings of C8 and HME (worst performance). The confusion matrix for the NW-CR array (not shown) indicates that it can distinguish nitromethane from the other two vapors without error (i.e., RR = 100%) but confuses n-hexane and toluene at a high rate (i.e., the RR values were both ~88%). A similar pattern of confusion is exhibited by the lower-ranked dual-

MPN-CR arrays. As the value of ε increases the performance of all arrays declines, and at $\varepsilon =$ 15% even the highest-ranked MPN-CR array exhibits unacceptably low RR values (i.e., $< 90\%$).

Analyses were then performed of arrays with larger numbers of sensors, including hybrid arrays consisting of 4-6 sensors (note: the smallest hybrid array considered was that consisting of two MPN-CRs and the two NW-CRs). The results are summarized in Table 2-1. All of the 3- and 4-sensor arrays are shown to perform quite well at the lowest level of superimposed error. As ε increases, however, differences in performance emerge. The two highest ranked 4-sensor arrays are the 'all-MPN' array, with coatings of DPA, HME, C8, and OPH, and the hybrid array that combines the DPA- and HME-coated CRs with the NW CR. Both give RR values $> 95\%$, even for $\varepsilon = 15\%$, and their performance is not statistically significantly different (i.e., the 95% confidence intervals around the average RR values overlap for all values of ε). The performance of the third-highest ranked 4-sensor array (i.e., DPA, HME, and NW) is not significantly different from that of the higher ranking arrays, but its average RR value falls off at the highest ε level, indicating somewhat less diversity. It is also noteworthy that the two highest-ranked 3-sensor MPN-arrays perform as well as the three highest-ranked 4-sensor arrays. On the other hand, the three lowest-ranked 4-sensor arrays show greater sensitivity to the level of superimposed error, and their performance declines significantly for $\varepsilon > 5\%$.

Thus, several arrays could be used for this vapor discrimination problem as long as there is only a small amount of variation in sensor responses from sample to sample (i.e., a small value of ε). The highest ranked arrays are more resilient to such variations. Most importantly, the best 4-sensor hybrid array performs no better (or worse) than the best 3- or 4-sensor array consisting entirely of MPN CRs.

Interestingly, there appears to be no benefit to using more than three sensors in terms of recognition or resiliency to response error. Although this is largely due to the relatively simple problem being posed, which does not *require* additional input for its resolution, it illustrates the diminishing yield in diversity with increasing array size. Similar findings have been reported in attempting to discriminate among larger sets of individual vapors and their simple mixtures with other single- and multi-transducer arrays employing sorptive interface layers [25-26, 31-32] .

2.4 Conclusions

Contact-printed tin-oxide NW-CR vapor sensors on membrane substrates with integrated heaters were fabricated, and the temperature dependence of the baseline conductance and sensitivity to each of three different organic vapors were characterized. The vapor sensitivity differed significantly among replicate NW-CR devices, due to differences in the number, size, and orientation of NWs involved in transporting charge across the electrode gap. However, taking the ratio of responses at two different temperatures yielded device-independent sensitivities that differed among the three test vapors examined.

The ability to discriminate among the test vapors on the basis of these response ratios was greater than that of some of the dual MPN-CR arrays to which it was compared, but less than others. Importantly, the best 4-sensor hybrid array one could create from a combination of NW and MPN CRs yielded vapor recognition rates that were not significantly different from those of the best 3- or 4-sensor array composed entirely of MPN-CRs. Furthermore, the 6-sensor hybrid array showed no improvement in performance over the best 3- and 4-sensor arrays.

Thus, this preliminary study suggests that there is little or no advantage to combining tin-oxide NW CRs with MPN CRs in hybrid arrays for vapor recognition compared to using arrays

consisting entirely of MPN CRs. The question of whether the performance of NW-CR array would improve by use of devices operating at more than two temperatures or by rapid modulation of the temperature of a single device [8], remains unanswered, and may be worth further investigation. Tests of mixtures, where the mixture components must be resolved from their composite, present a more difficult problem for any sensor array [25,30], and would form the basis of more rigorous future assessments of performance.

2.5 References

1 .   N. Barsan and U. Weimar, *Journal of Electroceramics* **2001**, *7*, 143-167.
2 .   F. Hernandez-Ramirez, J. D. Prades, R. Jimenez-Diaz, T. Fischer, A. Romano-Rodriguez, S. Mathur and J. R. Morante, *Phys Chem Chem Phys* **2009**, *11*, 7105-7110.
3 .   D. C. Meier, S. Semancik, B. Button, E. Strelcov and A. Kolmakov, *Applied Physics Letters* **2007**, *91*, 063118.
4 .   G. Sberveglieri, C. Baratto, E. Comini, G. Faglia, M. Ferroni, M. Pardo, A. Ponzoni and A. Vomiero, *Thin Solid Films* **2009**, *517*, 6156-6160.
5 .   A. Kolmakov, Y. Zhang, G. Cheng and M. Moskovits, *Advanced Materials* **2003**, *15*, 997-1000.
6 .   K. M. Ryu, D. H. Zhang and C. W. Zhoua, *Applied Physics Letters* **2008**, *92*, 093111.
7 .   L. Qin, J. Xu, X. Dong, Q. Pan, Z. Cheng, Q. Xiang and F. Li, *Nanotechnology* **2008**, *19*, 185705.
8 .   K. D. Benkstein, B. Raman, D. L. Lahr, J. E. Bonevich and S. Semancik, *Sensors and Actuators B-Chemical* **2009**, *137*, 48-55.
9 .   H. Wohltjen and A. W. Snow, *Analytical Chemistry* **1998**, *70*, 2856.
10 .   Y. Joseph, N. Krasteva, I. Besnard, B. Guse, M. Rosenberger, U. Wild, A. Knop-Gericke, R. Schlogl, R. Krustev, A. Yasuda and T. Vossmeyer, *Faraday Discussions* **2004**, *125*, 77-97.
11 .   L. Han, X. J. Shi, W. Wu, F. L. Kirk, J. Luo, L. Y. Wang, D. Mott, L. Cousineau, S. I. I. Lim, S. Lu and C. J. Zhong, *Sensors and Actuators B-Chemical* **2005**, *106*, 431-441.
12 .   F. J. Ibanez, U. Gowrishetty, M. M. Crain, K. M. Walsh and F. P. Zamborini, *Analytical Chemistry* **2006**, *78*, 753-761.
13 .   C.-J. Lu, W. H. Steinecker, W.-C. Tian, M. C. Oborny, J. M. Nichols, M. Agah, J. A. Potkay, H. K. L. Chan, J. Driscoll, R. D. Sacks, K. D. Wise, S. W. Pang and E. T. Zellers, *Lab on a chip* **2005**, *5*, 1123.
14 .   C. Yang, C. Li and C. Lu, *Analytica Chimica Acta* **2006**, *565*, 17.
15 .   L. Han, D. R. Daniel, M. M. Maye and C.-J. Zhong, *Analytical Chemistry* **2001**, *73*, 4441-4449.

16 .   W. H. Steinecker, M. P. Rowe and E. T. Zellers, *Analytical Chemistry* **2007**, *79*, 4977-4986.
17 .   Y. Joseph, A. Peic, X. D. Chen, J. Michl, T. Vossmeyer and A. Yasuda, *Journal of Physical Chemistry C* **2007**, *111*, 12855-12859.
18 .   E. Covington, F. I. Bohrer, C. Xu, E. T. Zellers and C. Kurdak, *Lab on a chip* **2010**.
19 .   Q.-Y. Cai and E. T. Zellers, *Analytical chemistry* **2002**, *74*, 3533-3539.
20 .   K. D. Schierbaum, A. Gerlach, M. Haug and W. Gopel, *Sensors and Actuators a-Physical* **1992**, *31*, 130-137.
21 .   M. Haug, K. D. Schierbaum, G. Gauglitz and W. Gopel, *Sensors and Actuators B-Chemical* **1993**, *11*, 383-391.
22 .   R. Zhou, A. Hierlemann, U. Weimar and W. Göpel, *Sensors and Actuators B: Chemical* **1996**, *34*, 356-360.
23 .   H. Ulmer, J. Mitrovics, G. Noetzel, U. Weimar and W. Göpel, *Sensors and Actuators B: Chemical* **1997**, *43*, 24-33.
24 .   M. Pardo, L. Kwong, G. Sberveglieri, K. Brubaker, J. Schneider, W. Penrose and J. Stetter, *Sensors and Actuators B: Chemical* **2005**, *106*, 136-143.
25 .   C. Jin, P. Kurzawski, A. Hierlemann and E. T. Zellers, *Analytical chemistry* **2008**, *80*, 227-236.
26 .   C. Jin and E. T. Zellers, *Analytical chemistry* **2008**, *80*, 7283-7293.
27 .   E. N. Dattoli, Q. Wan, W. Guo, Y. Chen, X. Pan and W. Lu, *Nano letters* **2007**, *7*, 2463-2469.
28 .   Z. Fan, J. C. Ho, Z. A. Jacobson, R. Yerushalmi, R. L. Alley, H. Razavi and A. Javey, *Nano letters* **2008**, *8*, 20-25.
29 .   Q. Zhong, W. H. Steinecker and E. T. Zellers, *Analyst* **2009**, *134*, 283-293.
30 .   M. P. Rowe, K. E. Plass, K. Kim, Ã. a. Kurdak, E. T. Zellers and A. J. Matzger, *Chem. Materials* **2004**, *16*, 3513-3517.
31 .   M.-D. Hsieh and E. T. Zellers, *Analytical chemistry* **2004**, *76*, 1885-1895.
32 .   J. Park, W. A. Groves and E. T. Zellers, *Analytical Chemistry* **1999**, *71*, 3877-3886.
33 .   Q. Wan, E. Dattoli and W. Lu, *Small* **2008**, *4*, 451-454.

Table 2-1. Average recognition rates (RR) with arrays of MPN CRs and NW CRs of different size (number) and composition for the discrimination of nitromethane, n-hexane, and toluene as determined by Monte-Carlo/EDPCR analysis (n=1000 iterations) with different levels of superimposed random response error (ε).

Array Size and Composition					Recognition Rate (%)		
2 sensors							
-	DPA	HME	-	-	99.9	95.0	88.0
-	-	HME	OPH	-	99.8	93.3	87.2
C8	-	-	OPH	-	99.8	94.3	85.3
-	-	-	-	NW	95.4	80.6	69.3
C8	DPA	-	-	-	91.3	80.7	74.4
-	DPA	-	OPH	-	85.7	76.5	68.2
C8	-	HME	-	-	77.0	70.8	66.8
3 sensors							
C8	-	HME	OPH	-	100.0	99.5	97.2
-	DPA	HME	OPH	-	100.0	98.6	93.9
C8	DPA	-	OPH	-	99.8	94.9	86.9
C8	DPA	HME	-	-	100.0	95.9	82.9
4 sensors							
C8	DPA	HME	OPH		100.0	99.8	97.4
-	DPA	HME	-	NW	100.0	98.6	95.5
C8	-	HME	-	NW	100.0	99.1	94.5
C8	-	-	OPH	NW	99.4	93.4	85.5
-	-	HME	OPH	NW	99.0	91.3	84.7
-	DPA	-	OPH	NW	98.6	89.8	81.3
C8	DPA	-	-	NW	94.6	83.1	77.3
5 sensors							
C8	DPA	HME	-	NW	100.0	98.9	95.4
C8	-	HME	OPH	NW	100.0	98.2	93.4
-	DPA	HME	OPH	NW	99.7	95.3	90.0
C8	DPA	-	OPH	NW	99.4	94.8	87.8
6 sensors							
C8	DPA	HME	OPH	NW	100.0	98.0	94.4
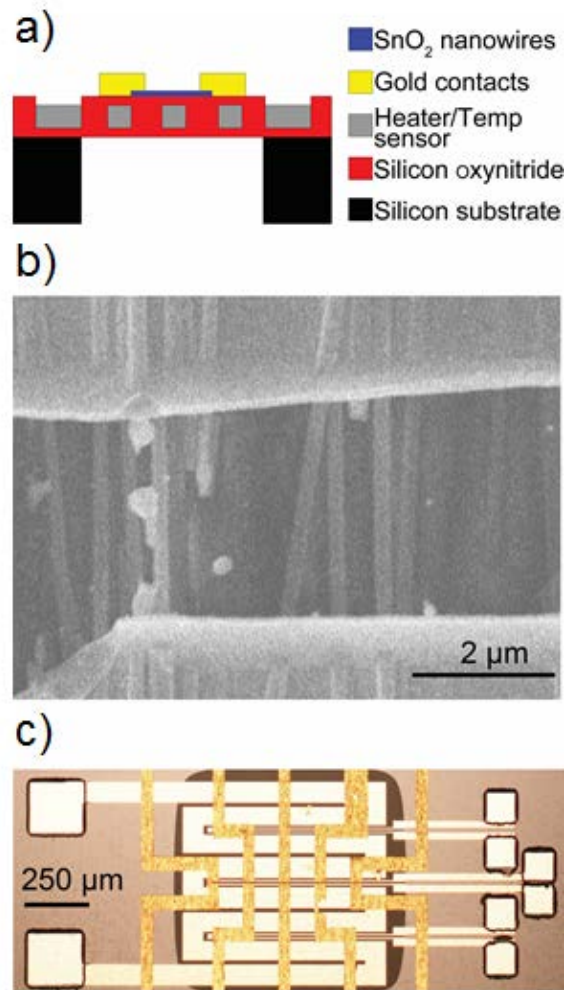
Figure 2-1. (a) Cross sectional diagram of the NW-CR on the membrane hotplate; (b) SEM image of tin-oxide NW mat bridging the CR electrodes; (c) Photomicrograph of the central region of the NW-CR chip with five electrode pairs distributed horizontally across the membrane hot plate.
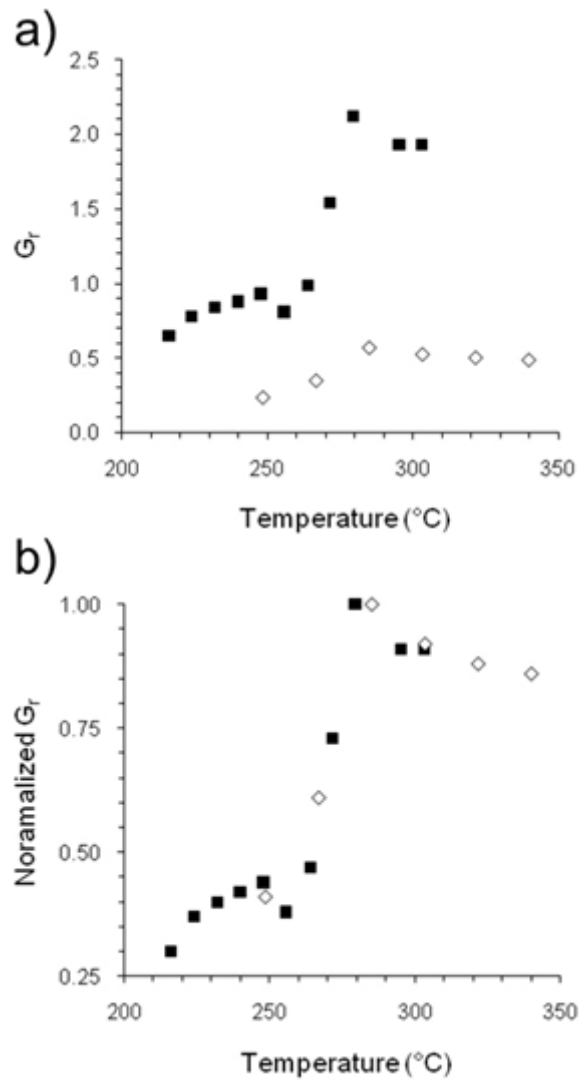
Figure 2-2. (a) Raw and b) normalized relative responses ($G_r = \Delta G/G$) to nitromethane as a function of temperature for two NW-CR devices (filled squares, device 1, 240 ppm; unfilled diamonds, device 2, 360 ppm). For (b), the responses shown in (a) were normalized to the response at 280 °C for device 1 and 285 °C for device 2.
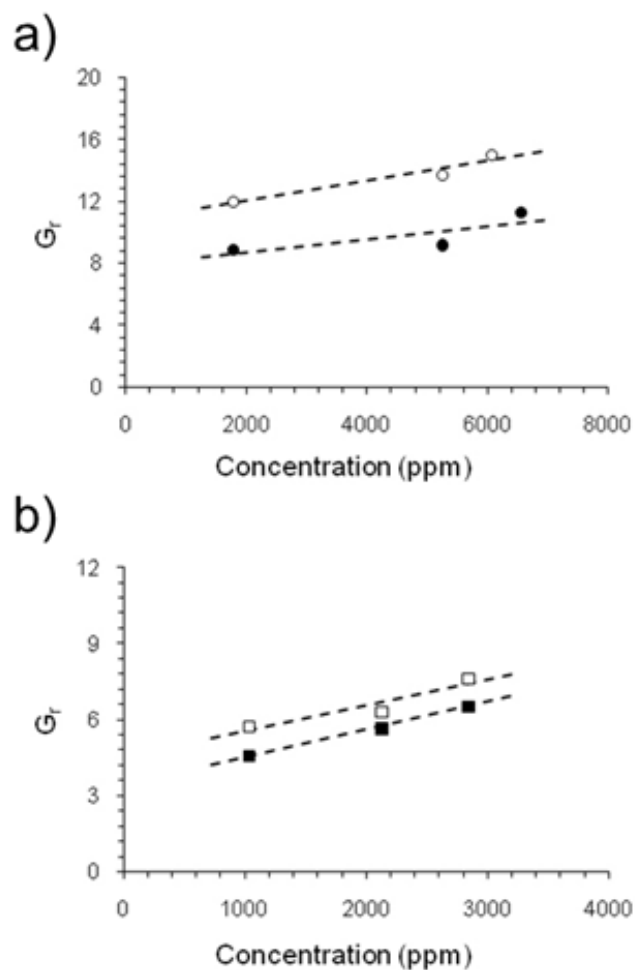
Figure 2-3. NW-CR calibration curves for (a) n-hexane and (b) toluene at 215 °C (filled symbols) and 280° C (unfilled symbols). Lines represent the least-squares fit of the data ($r^2 > 0.92$ in all cases). Response ratios do not vary significantly with concentration.
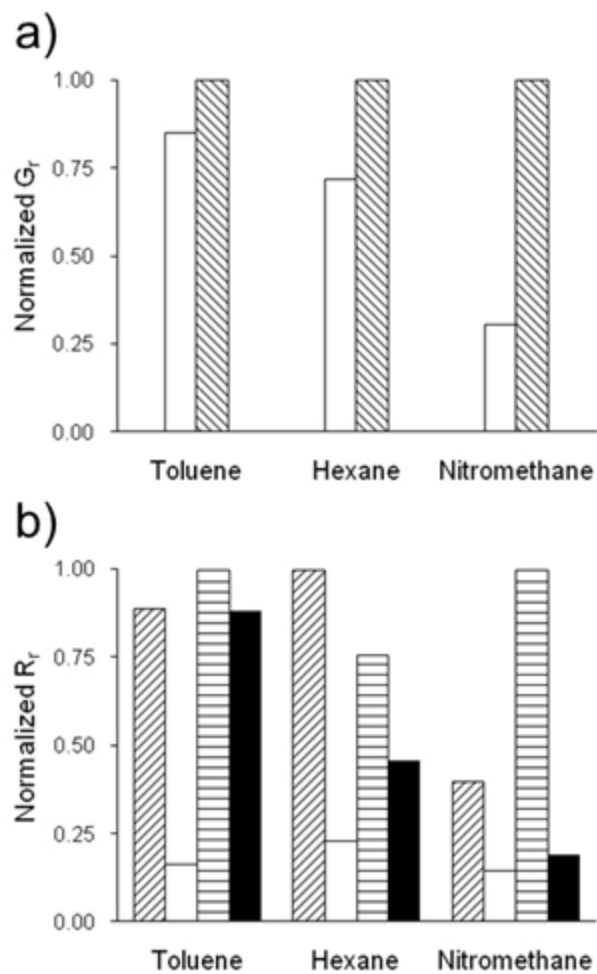
Figure 2-4. (a) Normalized relative response ratios for NW CRs exposed to the indicated vapors at 215° C (unfilled) and 280° C (cross-hatched); (b) normalized MPN-CR array sensitivities to the indicated vapors (in order, from left to right, C8, DPA, OPH, and HME).

Chapter III

Vapor Discrimination with Single- and Multi-Transducer Arrays of Nanoparticle Coated Chemiresistors and Resonators

3.1 Introduction

Microsensor arrays for the quantitative analysis of airborne volatile organic compounds (VOC) typically comprise a small set of transducers coated with interface layers that interact reversibly and differentially with a wide range of VOCs. Examples include arrays of polymer-coated surface acoustic wave resonators [1-2], cantilevers [3-6], and capacitors [7], as well as chemiresistors (CR) coated with metal-oxide semiconductors [8], conducting polymers [9], carbon-loaded insulating polymers [10], or monolayer-protected nanoparticles (MPN) [11-14]. By comparing the collective response patterns generated by the array to calibrated patterns in a reference library it is possible to differentiate one vapor from another.

Previous reports have shown that the recognition of individual vapors among a set of, say, 10 or more possibilities is often more facile than the discrimination of even a simple mixture from its components due to the low energies of reversible vapor-interface interactions involved and the inherent similarity of the patterns of a mixture and its components [3, 15-16]. The discrimination of mixtures of more than three vapors from their components or lower-order mixtures is generally not possible with standalone arrays [2, 15-16]. Furthermore, several reports have shown that the capability of an optimally selected set of sensors to differentiate one vapor from another does not

improve beyond ~4-6 sensors in the array, regardless of the transducer [2, 10, 17-19]. Combining sensors that operate on different transduction principles into hybrid, or multi-transducer (MT), arrays as a means of increasing the diversity of responses was first reported over 25 years ago [20-21], and has been explored in a few subsequent studies [18, 22-27]. Although the performance of MT arrays can be superior to that of single-transducer (ST) arrays of similar dimension (i.e., number of sensors), only a few studies have explored this topic systematically [18, 23, 26-27].

Two popular transducers are the TSMR and the CR. TSMRs, also known as quartz crystal microbalances, are bulk-wave mechanical oscillators. When coated with a sorptive interface layer and exposed to a vapor, mass uptake in the film due to vapor partitioning causes a measurable shift in resonant frequency [28]. Typical CRs are interdigital electrodes that measure changes in resistance (directly or indirectly) of a conductive or semiconductive interface film accompanying vapor sorption. Previous studies have explored the VOC responses of TSMRs and CRs coated with films of the same carbon-loaded insulating polymers and noted that the correlation varied with the VOC density [29-30]. Han, *et al.* [31] and Yang *et al.* [32] compared responses from TSMRs and CRs with matching films of MPNs and found transducer-dependent differences in the sign and/or magnitude of responses. More recently, Steinecker *et al.* showed correlations between MPN-coated TSMR and CR responses that depended on the VOC density and dielectric constant [33], suggesting that the pooled responses might provide more information than either alone. Subsequently, Bohrer *et al.* compared responses collected from four TSMRs and four ultra-small CRs with matching films of MPNs with four different thiolate moieties [34]. None of these studies examined CRs and TSMRs in MT arrays as a means for enhancing VOC discrimination. Very recently, Li et al. reported that an 8-sensor MT array composed of TSMRs and CRs with the same four MPN coatings could discriminate among 15 individual vapors better, on average, than either

4-sensor ST array, as expected, but noted that some 4-sensor MT arrays did not perform as well as the 4-sensor ST arrays [27].

In this article, we report on a study of the diversity of response patterns of MT and ST arrays of MPN-coated TSMR and CR sensors. Using the data set of vapor sensitivities reported by Bohrer *et al.* [34], we derived response patterns from every possible array of 2-8 sensors that could be constructed from the set of four TSMR and four CR sensors for each of the five vapors tested. Monte Carlo simulations were used to iteratively generate synthetic responses with different levels of random error superimposed on the calibrated sensitivities, and then principal component regression analysis was used to estimate the rates of recognition (RR) achievable among the different possible arrays. The performance was evaluated as a function of the array dimension, transducer type, and the thiolate functionalities on the MPNs. Analyses of binary mixtures were performed similarly by assuming linear additivity of responses.

3.2 Data set and analytical methods

3.2.1 Sensor fabrication, coating and vapor exposures

Detailed descriptions of the devices, interface films, and exposure tests are provided in the original study [34] and are only summarized here. The dielectric constants and (liquid) densities of the five VOCs are as follows: 2.00 ε_o, 0.703 g/ml (n-octane); 2.40 ε_o, 0.865 g/ml (toluene), 20.10 ε_o, 0.804 g/ml (n-propanol), 18.50 ε_o, 0.805 g/ml (2-butanone); 39.40 ε_o, 1.13 g/ml (nitromethane), where ε_o is the permittivity of free space.

Each CR chip had a set of four closely spaced interdigital electrodes (IDE) with active areas of 150 μm^2. All four CR devices on a given chip were coated simultaneously with a continuous film of the same MPN by drop casting from a suitable solvent. The average thickness

of the multilayer films was ~240 nm on the basis of AFM images of a representative film [34]. Four such CR chips were coated; one with each of the MPNs listed below. The average sensitivity from the sensors coated with a given MPN was used as the basis for the data analyses performed here.

Each of the four TSMRs consisted of a circular quartz crystal 1.4-cm diameter with 0.8-cm diameter gold electrode and a resonant frequency of 10 MHz. TSMR devices were coated by airbrushing a solution of MPNs with pressurized air as the propellant. Film masses of 24–28 μg were derived from the frequency shifts via the Sauerbrey equation, and gave average thicknesses of 116-136 nm, presumed to be in the acoustically thin regime [35]. MPNs with thiolate monolayers derived from n-octanethiol (C8), 4-(phenylethynyl)-benzenethiol (DPA), 6-phenoxyhexane-1-thiol (OPH), and methyl-6-mercaptohexanoate (HME) and ranging in Au core diameters from 3.4-4.7 nm were used.

CRs were mounted on custom PC boards and biased with the DC voltage from a battery (V=1.59 V) and connected in series with a reference resistor (R_{ref} = 3.0 MΩ). The voltage drop was measured by a multiplexer card (model 34970A/34902A, Agilent Technologies, Santa Clara, CA) and subsequently converted to resistance. All four CR array chips were installed in sockets on the floor of a 0.5-L stainless steel exposure chamber. TSMRs were mounted between Viton O-rings in a custom-made holder threaded into the lid of the chamber, and frequency was monitored by a phase-lock oscillator (Maxtek, Beaverton, OR).

3.2.2 Data analysis

The performance of every possible MT and ST array of 2-8 sensors permutable from the four MPN-CRs and four MPN-TSMRs was assessed by use of Monte Carlo simulations and extended disjoint principal component regression (EDPCR) classification models. Synthetic

responses were generated by randomly selecting a vapor concentration within the range of 5-15 $\times$ LOD (where the LOD was dictated by the least sensitive sensor in the array) and then multiplying by the experimental sensitivity (i.e., slope of the calibration curve). Error was introduced by multiplying that response value by a factor derived from randomly sampling a Gaussian distribution with a mean of one and a standard deviation of 0.05, 0.075, or 0.10, corresponding to random sensitivity errors, ε, of 5, 7.5, or 10% of the response, respectively.

The error enhanced responses from all sensors in the array under consideration were combined and the location of the resulting response vector was projected sequentially onto the principal component corresponding to the original calibrations for each vapor via EDPCR. The identity of the vapor assigned to this synthetic response (test) vector was that for which the Euclidean distance between test and calibration vector was the shortest. This procedure was performed iteratively (i.e., 500 samples) to obtain a precise statistical estimate of recognition rate (RR; the fraction of correct assignments out of the total) for each array at each level of ε. Details of this methodology as applied to sensor array evaluations can be found elsewhere [2, 13-14, 16].

Assessment of binary mixture recognition was performed similarly by assuming that the composite response to a binary mixture was equivalent to the sum of the responses of the two components at their respective concentrations [36]. Thus, sensor responses were computed for an independent, randomly selected concentration of each vapor alone (within the range of 5-15×LOD, as defined above) and then combined. Using EDPCR, the composite response vector was assigned to the mixture or to one of the component vapors (i.e., each binary mixture was considered separately). Iteration, again, yielded a precise statistical estimate of the RR for the mixture. All 10 possible binary mixtures were considered in succession.

EDPCR modeling and Monte Carlo simulations were performed on a desktop computer

using routines written in Visual Basic (version 7.0, Microsoft Corp.) and linked to spreadsheets in Excel (version 7.0, Microsoft Corp.). Principal components (PC) plots were generated using R statistical software (version 2.13.1, R Foundation).

3.3 Results and discussion

3.3.1 Individual vapor recognition

For reference, the 10 vapor-wise 4-ST$_{tsmr}$ and 4-ST$_{cr}$ array response patterns, normalized to the highest-sensitivity sensor for a given vapor, are presented in Figure 3-1. As noted in the original article [34], the DPA-coated TSMR sensor (DPA$_{tsmr}$) exhibits the highest of all TSMR sensitivities for all vapors, due to the higher fractional mass of organic material in the DPA film, while the DPA-coated CR sensor (DPA$_{cr}$) exhibits the lowest of all CR sensitivities for all vapors, due to the lower swelling efficiency of the rigid conjugated structure of the DPA moiety. Among the CRs, the OPH$_{cr}$ has the highest sensitivity to all VOCs except OCT for which the C8$_{cr}$ is the most sensitive. The latter can be attributed to a combination of vapor affinity and the flexibility and swelling efficiency of the highly intercalated C8 chains on adjacent MPN cores [34]. Among the CRs the range of relative sensitivities between any two sensors is as high as 35-fold (typically < 15-fold), whereas among the TSMRs the range is about 5-fold or less.

Figure 3-2a plots the average RR value ($\varepsilon = 5\%$) of all five individual vapors for the best performing 2-, 3-, and 4-ST and MT arrays. Among all possible 2-ST$_{tsmr}$ and 2-ST$_{cr}$ arrays, the average RR values for recognition of the individual vapors span from 46.4–97.1% for the former and from 65.6–88.1% for the latter. For the 2-MT arrays the range is 58.4–90.6 % (Table 3-1). This emphasizes the importance of being judicious in selecting sensors to include in an array [15]. Surprisingly, the best 2-ST$_{tsmr}$ array (C8$_{tsmr}$+OPH$_{tsmr}$, RR = 97.1%) outperforms the best 2-ST$_{cr}$

array (C8$_{cr}$+DPA$_{cr}$, RR = 88.1%) and the best MT array (HME$_{cr}$+DPA$_{tsmr}$, RR = 90.6%). The differences in average RR values reflect 'real' differences in expected performance, but are not statistically significant because the range of individual-vapor RR values is quite broad, as shown in Table 3-1. That an array of just two sensors effectively recognizes and discriminates among five vapors is consistent with results reported previously for arrays of polymer-coated SAW sensors and MPN-coated CRs [2, 13, 15-16]. That a 2-ST$_{tsmr}$ array affords a higher degree of diversity is surprising because of its dependence only on mass uptake; the dependence of the CRs on changes in volume and dielectric constant might have been expected to yield greater diversity, given the range of densities and dielectric constants among the test vapors.

Increasing the number of sensors in the array leads to a significant increase in the RR of the best-performing ST$_{cr}$ arrays, but little or no change in RR for the best ST$_{tsmr}$ arrays; the 4-ST$_{tsmr}$ and 4-ST$_{cr}$ arrays perform equally well (RR = 97%). Although this level of performance is quite good, as shown, the best 3- and 4-MT arrays perform slightly better on average (RR = 99.7%). These results suggest that only two of the four TSMR sensors contribute a significant amount of uncorrelated (i.e., independent) information about the vapors to the ST$_{tsmr}$ arrays, and that combining certain TSMR and CR transducers results in a modest increase in uncorrelated information relative to either ST array.

The plateau in the RR value for mid-range array dimensions is followed by a decline at higher dimensions (Figure 3-2b), which is a general feature of vapor sensor arrays [2, 18-19]; additional sensors contribute little or no independent information about the vapors, despite having interface films of MPNs with different thiolate functionalities, while they contribute an increasing amount of dispersion to all response patterns. As expected, the average RR value decreases as the degree of superimposed variation in sensitivity increases for the optimal MT arrays of 2-8 sensors

(Figure 3-2b). If a minimum threshold RR of 95% is adopted [2], then no more than 7.5% random variation in sensitivity among the sensors is tolerable without a significant loss in average performance for this data set. Although maintaining this level of control in sensitivity drift is apparently achievable in practice [37], this constraint on performance must be kept in mind.

The correlation matrix in Table 3-2 presents the pair-wise correlation coefficients, r, derived from the linear regressions of the sensitivities to all five test vapors of one sensor onto those of another. Among the TSMR sensor pairs, Table 3-2 shows that the $C8_{tsmr}$, DPA_{tsmr} and HME_{tsmr} responses are highly correlated (i.e., r = 0.99 in all cases) and the RR values for the corresponding 2-ST_{tsmr} arrays are low (i.e., < 65%). The other three pairs of TSMR sensors have r values ≤ 0.83 and the RR values for these 2-ST_{tsmr} arrays are higher. A similar analysis of the 2-CR and 2-MT arrays, however, reveals several instances where a low r value between a pair of sensors does not produce a high RR, such as for $C8_{cr}+OPH_{cr}$ and $C8_{cr}+HME_{cr}$. This is due to OCT, for which the relative sensitivities of the sensors differ markedly from those for the other four vapors, while the relative sensitivities to the other vapors are more highly correlated.

The representative linear regressions shown in Figure 3-4 for the $C8_{cr}+OPH_{cr}$ array reveal that the high correlation among the other four vapors is masked by the OCT data point when the r value is derived from the entire set of vapor sensitivities. Although OCT is easily discriminated from the other vapors, none of the other vapors is easily discriminated from one another, and the average RR value is therefore quite low. Even a relatively high r value does not necessarily result in a low RR value: if the regression line does not pass near or through the origin, then the r value inflates the degree of correlation among the sensor responses to the different vapors. This highlights the shortcomings of using pair-wise correlation metrics to select sensors and/or interface materials. Interestingly, three of the four cross-transducer pairs with a common MPN coating give

high r values and correspondingly low RR values. The HME coated pair is the exception, with a relatively low r value of 0.65 and a relatively high RR value of ~78%. Accordingly, the HME_{cr} and HME_{tsmr} sensors are included in the best-performing 4-MT array (see below).

Figure 3-3 shows principal component projections for each 4-ST array and the best-performing 4-MT array ($C8_{tsmr}+OPH_{tsmr}+HME_{tsmr}+HME_{cr}$). The central cluster corresponding to each vapor is the result of using synthetic responses with $\varepsilon =1\%$ and the corresponding elliptical boundary is the 95% confidence interval (CI_{95}) calculated from the synthetic responses generated with $\varepsilon =5\%$. As shown, the CI_{95} boundaries for POH, TOL and NME overlap in the $4\text{-}ST_{cr}$ plot and those for POH and TOL overlap in the $4\text{-}ST_{tsmr}$ plot. There is only a slight overlap for the NME+MEK and TOL+POH pairs in the 4-MT plot. Consistent with this, confusion matrices derived from EDPCR analyses indicate that TOL and POH are confused for each other at rates of 3-7% for the $4\text{-}ST_{cr}$ and $4\text{-}ST_{tsmr}$ arrays and only 0.8% for the 4-MT array. For all arrays, OCT is well separated and easily discriminated from all other vapors.

Table 3-1 presents the compositions of the best-performing 2-, 3-, and 4-ST and MT arrays along with the average and range of RRs for individual-vapor recognition. As the array dimension increases, the number of MT arrays providing acceptable performance increases: there are 11 3-MT arrays and 18 4-MT arrays with average RR values $\geq 95\%$. Among these there are six 3-MT arrays that outperform the best 3-ST array and 13 4-MT arrays that outperform the best 4-ST array. Table 3-1 also shows the arrays of each dimension that provide the lowest RR values; the worst-performing 2-, 3-, and 4-MT arrays give RR values much lower than those of the best-performing ST arrays of the same dimension, demonstrating, again, the importance of careful sensor selection. Notably, C8, OPH, and HME all appear in the best-performing 3- and 4-sensor arrays, regardless

of transducer type, indicating that the extent of vapor-interface interaction is perhaps a more important determinant of array diversity than is the transducer.

3.3.2 Binary mixture analyses

With 2- and 3-sensor arrays, the only binary mixtures that could be discriminated from their components with RR values >95% are those containing OCT. Among these arrays, the best 2-ST_{cr} array performs slightly better than the best 2-MT array, but the best 3-ST_{cr} array and the best 3-MT array perform equally well. The 2- and 3-ST_{tsmr} arrays do not perform as well. None of the 2- or 3-sensor arrays could discriminate any of the other six binary mixtures from their components with RR values > 90%.

With arrays of 4 sensors, the performance generally follows what would be expected on the basis of the cluster separation distances in the PCA plots of Figure 3-3. For the 4-ST_{cr} array, mixtures containing OCT are easily discriminated from their components, whereas mixtures of other vapors give much lower RR values (Table 3-3). For the 4-ST_{tsmr} arrays only one mixture could be analyzed effectively (i.e., NME+OCT, RR = 96.4%), consistent with these two vapors having the greatest separation in Figure 3-3b. In general, the RR values for the mixtures depend strongly on their separation distances in Figs. 3a-c, as expected.

Two approaches were taken to further assess the performance of the 4-MT arrays. First, the two 4-MT arrays yielding the highest average RR values on the basis of individual-vapor recognition were considered. These also give the highest average RR values among all 10 binary mixture analyses: 74.7% for both arrays. This value exceeds the average RR values for the 4-ST_{cr} and 4-ST_{tsmr} arrays by a small margin (71.3 and 69.7%, respectively). However, neither top MT array provides an RR >95% for any specific mixture.

In the second approach to MT array assessment, the 4-MT array giving the highest mixture-specific RR value was selected successively for each of the 10 mixtures. In those cases where the array composition differed from the two selected on the basis of the highest overall average RR, the array is listed in Table 3-3. As shown, there are eight different 4-MT arrays required to achieve the highest possible RR values for all mixtures, and each of the eight possible sensors is represented at least once among these 4-MT arrays. In all cases, the highest RR value for a specific mixture is always provided by a 4-MT array, but the best performance for one or two specific mixtures by one 4-MT array is invariably coupled with significantly poorer performance than a different 4-MT array for several of the other mixtures. Furthermore, none of the 4-MT arrays consistently outperforms either 4-ST array for all mixtures.

This prompted the question of whether a single MT array of higher dimension might provide better overall performance. To answer this, again two approaches were taken. First, the best 5-, 6-, 7-, and 8-MT arrays were identified on the basis of overall average performance. The average RR values for these arrays range from 71.6 to 68.6 %, which are lower than the RR values for the best performing 4-MT arrays (overall average) shown in Table 3-3. Second, starting with the best 4-MT array for each mixture in Table 3-3, the best-performing MT arrays of higher dimension were identified for that specific mixture. Figure 3-5 shows some representative data.

For mixtures containing OCT, performance peaks at n = 4 or 5 sensors and stays constant or declines very slightly out to n = 8, as shown for the TOL+OCT case. For mixtures with components separated by a somewhat shorter Euclidean distance than those between OCT and the other components (on the basis of Figure 3-3c), the performance declines gradually but steadily as each additional sensor is added to the optimal MT array, as shown in Figure 3-5 for TOL+MEK. Where the Euclidean distance between mixture components is quite short (Figure 3-3c), there is a

dramatic decrease in RR value as the array dimension increases to n = 8, as shown in Figure 3-5 for POH+NME. These trends re-affirm that adding highly correlated sensors to an array merely increases the dispersion of the patterns used for discrimination, and show further that performance degrades more rapidly for mixtures of components with more similar patterns.

These results suggest the possibility of deploying an array of all eight sensors and then down-selecting the subset of sensors providing the best performance for a given analysis as needed. Since the problems posed in the binary analyses assumed that the range of possible analytes was limited to the mixture or either of its two components, it is feasible to exercise such an option. If the components of the mixture were not known and constrained in this way, however, this option would not be feasible. Such constraints would apply when using an MT array as the detector for (micro) gas chromatographic (GC) analysis [37-38], where the identities of co-eluting or partially co-eluting analytes could be determined *apriori* by calibration. In this case, post-measurement down-selection of a different optimal subset of sensors for each set of overlapping peaks eluting in specific retention time windows would be possible.

Note that the average RR of the optimal mixture-specific 4-MT arrays that could be down-selected is 86.9%, with only four mixtures giving RR values > 95%. Thus, although this average RR exceeds that for the 4-MT array selected on the basis of overall average RR value (74.7%), such performance is still not acceptable. Taking advantage of partial chromatographic resolution by use of multivariate curve resolutions methods should enhance the discrimination, though for co-eluting vapors with similar patterns the chromatographic resolution may need to be fairly high [39].

3.4 Conclusions

Distinct differences were observed in the vapor discrimination capabilities of ST arrays of low dimension (i.e., $n \leq 4$) assembled from the MPN-coated CR and TSMR vapor sensors considered here, consistent with the results reported by Li, et al. [27]. Although the best MT arrays generally outperformed the best ST arrays, differences were often marginal and exceptions occurred. The specific sensors included in the MT array was critical, and both the interface material and transducer were important factors. Correlation analysis was of limited use in assessing the extent to which two sensors complement each other in effecting the discrimination of multiple vapors. PCA and comparisons of Euclidean distances were much better tools for predicting recognition rates, particularly for binary mixtures.

The relatively facile problem of discriminating among a set of individual vapors could be solved adequately with both types of 4-ST arrays and with numerous 4-MT arrays. Importantly, performance was not improved by adding more sensors to the MT array. This finding is consistent with those from other studies of this topic with vapor sensor arrays employing sorptive interfaces, and argues strongly for moving the research agenda beyond such problems to the more challenging problems of quantitatively analyzing mixtures of vapors [2, 16, 18].

No single array of any type provided universally optimal performance for the 10 binary mixtures considered here, despite each mixture being tested separately and the problem being constrained to a determination of whether one or both components was present. Furthermore, six of the mixtures could not be determined with sufficiently high RR values to be effective with any array. Increasing the number of sensors in the array from four to eight invariably led to a decline in performance, which was often dramatic, and serves as yet another reminder to limit the number of sensors used for a given analysis [16, 18, 26].

This study lends support to arguments that the only feasible way to take advantage of the vapor recognition capabilities of ST or MT arrays in performing quantitative analysis of vapor mixtures is to couple them with an upstream chromatographic separation module [2, 16, 18, 26, 36-39]. Although the 4-MT array providing the highest average RR value among the individual vapors also provided the highest average RR value for the 10 binary mixtures, if each mixture was considered separately, then the best-performing 4-MT array differed in all but one case. Using a large MT array as a GC detector and down-selecting subsets of sensors to analyze different overlapping peaks in specific retention-time windows, as proposed here, shows promise and could be pre-programmed into the chemometric software routines used in such (micro)systems.

3.5 References

1 .   J. W. Grate, *Chemical reviews* **2000**, *100*, 2627-2648.
2 .   J. Park, W. A. Groves and E. T. Zellers, *Analytical chemistry* **1999**, *71*, 3877-3886.
3 .   L. R. Senesac, P. Dutta, P. G. Datskos and M. J. Sepaniak, *Analytica Chimica Acta* **2006**, *558*, 94-101.
4 .   L. Pinnaduwage, D. Hedden, A. Gehl, V. Boiadjiev, J. Hawk, R. Farahi, T. Thundat, E. Houser, S. Stepnowski and R. McGill, *Review of Scientific Instruments* **2004**, *75*, 4554-4557.
5 .   P. J. Chapman, F. Vogt, P. Dutta, P. G. Datskos, G. L. Devault and M. J. Sepaniak, *Analytical chemistry* **2007**, *79*, 364-370.
6 .   M. Li, E. Myers, H. Tang, S. Aldridge, H. McCaig, J. Whiting, R. Simonson, N. Lewis and M. Roukes, *Nano letters* **2010**, *10*, 3899-3903.
7 .   S. Patel, T. Mlsna, B. Fruhberger, E. Klaassen, S. Cemalovic and D. Baselt, *Sensors and Actuators B: Chemical* **2003**, *96*, 541-553.
8 .   F. Röck, N. Barsan and U. Weimar, *Chemical reviews* **2008**, *108*, 705-725.
9 .   J. Hatfield, P. Neaves, P. Hicks, K. Persaud and P. Travers, *Sensors and Actuators B: Chemical* **1994**, *18*, 221-228.
10 .   B. J. Doleman, M. C. Lonergan, E. J. Severin, T. P. Vaid and N. S. Lewis, *Analytical Chemistry* **1998**, *70*, 4177-4190.
11 .   L. Han, X. Shi, W. Wu, F. L. Kirk, J. Luo, L. Wang, D. Mott, L. Cousineau, S. I.-I. Lim and S. Lu, *Sensors and Actuators B: Chemical* **2005**, *106*, 431-441.
12 .   Y. Joseph, A. Peic, X. Chen, J. Michl, T. Vossmeyer and A. Yasuda, *The Journal of Physical Chemistry C* **2007**, *111*, 12855-12859.
13 .   Q. Zhong, W. H. Steinecker and E. T. Zellers, *Analyst* **2009**, *134*, 283-293.
14 .   E. Dovgolevsky, U. Tisch and H. Haick, *Small* **2009**, *5*, 1158-1161.

15 .   E. T. Zellers, S. A. Batterman, M. Han and S. J. Patrash, *Analytical chemistry* **1995**, *67*, 1092-1106.

16 .   M.-D. Hsieh and E. T. Zellers, *Analytical chemistry* **2004**, *76*, 1885-1895.

17 .   A. J. Ricco, R. M. Crooks and G. C. Osbourn, *Accounts of chemical research* **1998**, *31*, 289-296.

18 .   C. Jin, P. Kurzawski, A. Hierlemann and E. T. Zellers, *Analytical chemistry* **2008**, *80*, 227-236.

19 .   E. García-Berríos, T. Gao, J. C. Theriot, M. D. Woodka, B. S. Brunschwig and N. S. Lewis, *The Journal of Physical Chemistry C* **2011**, *115*, 6208-6217.

20 .   A. W. Snow, W. R. Barger, M. Klusty, H. Wohltjen and N. L. Jarvis, *Langmuir* **1986**, *2*, 513-519.

21 .   B. Bott and T. Jones, *Sensors and Actuators* **1986**, *9*, 19-25.

22 .   K. Schierbaum, A. Gerlach, M. Haug and W. Göpel, *Sensors and Actuators A: Physical* **1992**, *31*, 130-137.

23 .   M. Pardo, L. Kwong, G. Sberveglieri, K. Brubaker, J. Schneider, W. Penrose and J. Stetter, *Sensors and Actuators B: Chemical* **2005**, *106*, 136-143.

24 .   M. Holmberg, F. Winquist, I. Lundström, J. Gardner and E. Hines, *Sensors and Actuators B: Chemical* **1995**, *27*, 246-249.

25 .   H. Ulmer, J. Mitrovics, U. Weimar and W. Göpel, *Sensors and Actuators B: Chemical* **2000**, *65*, 79-81.

26 .   C. Jin and E. T. Zellers, *Analytical chemistry* **2008**, *80*, 7283-7293.

27 .   C.-L. Li, Y.-F. Chen, M.-H. Liu and C.-J. Lu, *Sensors and Actuators B: Chemical* **2012**, *169*, 349-359.

28 .   M. Janghorbani and H. Freund, *Analytical Chemistry* **1973**, *45*, 325-332.

29 .   E. J. Severin and N. S. Lewis, *Analytical chemistry* **2000**, *72*, 2008-2015.

30 .   C. A. Mills, J. Beeley, C. Wyse, D. R. Cumming, A. Glidle and J. M. Cooper, *Sensors and Actuators B: Chemical* **2007**, *125*, 85-91.

31 .   L. Han, D. R. Daniel, M. M. Maye and C.-J. Zhong, *Analytical chemistry* **2001**, *73*, 4441-4449.

32 .   C.-Y. Yang, C.-L. Li and C.-J. Lu, *Analytica chimica acta* **2006**, *565*, 17-26.

33 .   W. H. Steinecker, M. P. Rowe and E. T. Zellers, *Analytical chemistry* **2007**, *79*, 4977-4986.

34 .   F. I. Bohrer, E. Covington, C. a. Kurdak and E. T. Zellers, *Analytical chemistry* **2011**, *83*, 3687-3695.

35 .   J. W. Grate, D. A. Nelson and R. Skaggs, *Analytical chemistry* **2003**, *75*, 1868-1879.

36 .   Q.-Y. Cai and E. T. Zellers, *Analytical chemistry* **2002**, *74*, 3533-3539.

37 .   S. K. Kim, H. Chang and E. T. Zellers, *Analytical chemistry* **2011**, *83*, 7198-7206.

38 .   C.-J. Lu, W. H. Steinecker, W.-C. Tian, M. C. Oborny, J. M. Nichols, M. Agah, J. A. Potkay, H. K. Chan, J. Driscoll and R. D. Sacks, *Lab on a Chip* **2005**, *5*, 1123-1131.

39 .   C. Jin and E. T. Zellers, *Sensors and Actuators B: Chemical* **2009**, *139*, 548-556.

Table 3-1. Average and range of recognition rates (RR) among the 5 individual vapors for the best- and worst-performing arrays consisting of 2, 3, and 4 sensors ($\varepsilon = 5\%$).

Array Dimension and Type	Composition	RR (%) Avg.	Range
	n = 2 sensors		
	Best-performing		
ST_{cr}	$C8_{cr} + DPA_{cr}$	88.1	77.9–98.2
ST_{cr}	$OPH + HME_{cr}$	79.7	62.1–97.3
ST_{cr}	$DPA_{cr} + OPH_{cr}$	79.6	60.4–98.8
ST_{tsmr}	$C8_{tsmr} + OPH_{tsmr}$	97.1	93.7–100.0
ST_{tsmr}	$DPA_{tsmr} + OPH_{tsmr}$	84.7	70.8–98.6
ST_{tsmr}	$OPH_{tsmr} + HME_{tsmr}$	70.7	55.6–85.9
MT	$HME_{cr} + DPA_{tsmr}$	90.6	83.5–97.7
MT	$C8_{cr} + OPH_{tsmr}$	82.5	68.6–96.4
MT	$OPH_{cr} + HME_{tsmr}$	80.4	68.2–92.5
	Worst-performing		
ST_{cr}	$C8_{cr} + HME_{cr}$	65.6	37.5–93.6
ST_{tsmr}	$DPA_{tsmr} + HME_{tsmr}$	46.4	31.7–61.2
MT	$OPH_{cr} + DPA_{tsmr}$	58.4	37.0–79.8
	3 sensors		
	Best-performing		
ST_{cr}	$HME_{cr} + C8_{cr} + OPH_{cr}$	94.6	90.0–99.2
ST_{cr}	$DPA_{cr} + OPH_{cr} + HME_{cr}$	92.5	86.7–98.3
ST_{cr}	$C8_{cr} + DPA_{cr} + HME_{cr}$	86.3	75.5–97.0
ST_{tsmr}	$HME_{tsmr} + C8_{tsmr} + OPH_{tsmr}$	97.7	94.8–100.0
ST_{tsmr}	$C8_{tsmr} + DPA_{tsmr} + OPH_{tsmr}$	97.0	93.8–100.0
ST_{tsmr}	$DPA_{tsmr} + OPH_{tsmr} + HME_{tsmr}$	86.7	73.5–100.0
MT	$HME_{cr} + C8_{tsmr} + OPH_{tsmr}$	99.7	99.3–100.0
MT	$DPA_{cr} + C8_{tsmr} + OPH_{tsmr}$	99.2	98.3–100.0
MT	$DPA_{cr} + OPH_{tsmr} + HME_{tsmr}$	99.0	97.9–100.0
	Worst-performing		
ST_{cr}	$C8_{cr} + DPA_{cr} + OPH_{cr}$	85.6	72.5–98.8
ST_{tsmr}	$C8_{tsmr} + DPA_{tsmr} + HME_{tsmr}$	83.2	71.9–94.4
MT	$C8 + HME_{cr} + HME_{tsmr}$	69.2	43.4–95.0
	4 sensors		
	Best-performing		
ST_{cr}	$DPA_{cr} + HME_{cr} + C8_{cr} + OPH_{cr}$	96.7	93.9–99.5
ST_{tsmr}	$DPA_{tsmr} + HME_{tsmr} + C8_{tsmr} + OPH_{tsmr}$	96.5	92.3–100.0
MT	$HME_{cr} + HME_{tsmr} + C8_{tsmr} + OPH_{tsmr}$	99.7	99.4–99.9
MT	$DPA_{cr} + HME_{tsmr} + C8_{tsmr} + OPH_{tsmr}$	99.1	98.2–100.0
MT	$DPA_{cr} + HME_{cr} + DPA_{tsmr} + OPH_{tsmr}$	98.6	96.9–100.0
	Worst-performing		
MT	$C8_{cr} + HME_{cr} + C8_{tsmr} + HME_{tsmr}$	70.0	45.3–94.8

Table 3-2. Matrix of pair-wise correlation coefficients, r, derived from the linear regression of sensitivities between each pair of sensors, and the average RR values (%, in parentheses) of the corresponding 2-sensor arrays derived from Monte Carlo/EDPCR analyses ($\varepsilon = 5\%$) for the five individual test vapors.

	$C8_{cr}$	DPA_{cr}	OPH_{cr}	HME_{cr}	$C8_{tsmr}$	DPA_{tsmr}	OPH_{tsmr}	HME_{tsmr}
$C8_{cr}$	1							
DPA_{cr}	0.59 (88.1)	1						
OPH_{cr}	0.22 (79.0)	0.87 (79.6)	1					
HME_{cr}	0.38 (65.6)	0.93 (67.6)	0.99 (79.7)	1				
$C8_{tsmr}$	0.94 (62.9)	0.83 (79.1)	0.53 (79.1)	0.65 (78.6)	1			
DPA_{tsmr}	0.90 (69.6)	0.87 (65.8)	0.62 (58.4)	0.74 (90.6)	0.99 (65.0)	1		
OPH_{tsmr}	0.53 (82.5)	0.89 (78.7)	0.91 (59.8)	0.95 (77.1)	0.76 (97.1)	0.83 (84.7)	1	
HME_{tsmr}	0.94 (69.6)	0.80 (70.7)	0.52 (80.4)	0.65 (77.8)	0.99 (63.3)	0.99 (46.4)	0.78 (70.7)	1

Table 3-3. Recognition rates (RR, %) of binary vapor mixtures for the 4-ST arrays, the two 4-MT arrays giving the highest overall average RR values, and the 4-MT arrays giving the highest mixture-specific RR values as determined by Monte Carlo/EDPCR analyses ($\varepsilon = 5\%$).[a]

Array Composition				RR (%)										
				POH OCT	TOL OCT	MEK OCT	NME OCT	TOL NME	MEK NME	POH NME	TOL POH	MEK POH	MEK TOL	Average
4-ST arrays														
C8$_{cr}$	OPH$_{cr}$	DPA$_{cr}$	HME$_{cr}$	96.2	97.8	97.8	98	36.8	47.8	31.8	31.8	68.4	72.8	71.3
C8$_{tsmr}$	OPH$_{tsmr}$	DPA$_{tsmr}$	HME$_{tsmr}$	67.8	78.8	90.0	96.4	72.4	52.0	77.6	27.8	66.6	47.6	69.7
Best 4-MT arrays: overall average														
C8$_{tsmr}$	OPH$_{tsmr}$	HME$_{cr}$	HME$_{tsmr}$	81.8	90.6	81.0	90.6	79.2	58.6	71.8	49.2	66.6	**78.0**	74.7
C8$_{tsmr}$	OPH$_{tsmr}$	DPA$_{cr}$	HME$_{tsmr}$	85.2	78.4	86.4	93.2	84.6	**84.0**	**89.8**	44.0	58.8	42.8	74.7
Best 4-MT arrays: mixture specific														
OPH$_{tsmr}$	DPA$_{cr}$	DPA$_{tsmr}$	HME$_{cr}$	81.2	77.4	50.0	70.6	83.0	78.2	75.0	**62.4**	41.6	75.2	69.5
C8$_{cr}$	C8$_{tsmr}$	OPH$_{cr}$	HME$_{cr}$	96.6	98.2	**98.4**	97.8	36.2	52.0	29.0	25.8	70.6	72.0	67.7
C8$_{cr}$	OPH$_{cr}$	HME$_{cr}$	DPA$_{tsmr}$	**97.4**	97.4	97.2	98.0	35.4	47.4	31.8	24.8	**71.6**	74.2	67.5
OPH$_{tsmr}$	DPA$_{cr}$	HME$_{cr}$	HME$_{tsmr}$	85.2	65.8	46.2	73.8	**89.6**	78.2	68.0	56.0	36.2	75.6	67.5
C8$_{cr}$	OPH$_{cr}$	HME$_{cr}$	HME$_{tsmr}$	96.0	**99.6**	98.2	97.4	37.2	53.0	24.2	24.2	69.6	71.6	67.1
C8$_{cr}$	C8$_{tsmr}$	OPH$_{cr}$	HME$_{tsmr}$	94.2	95.8	97.8	**98.4**	6.6	35.4	24.0	16.0	58.0	45.0	57.1

[a] Dashed boxes indicate the highest RR value for a given mixture among all 4-MT arrays.
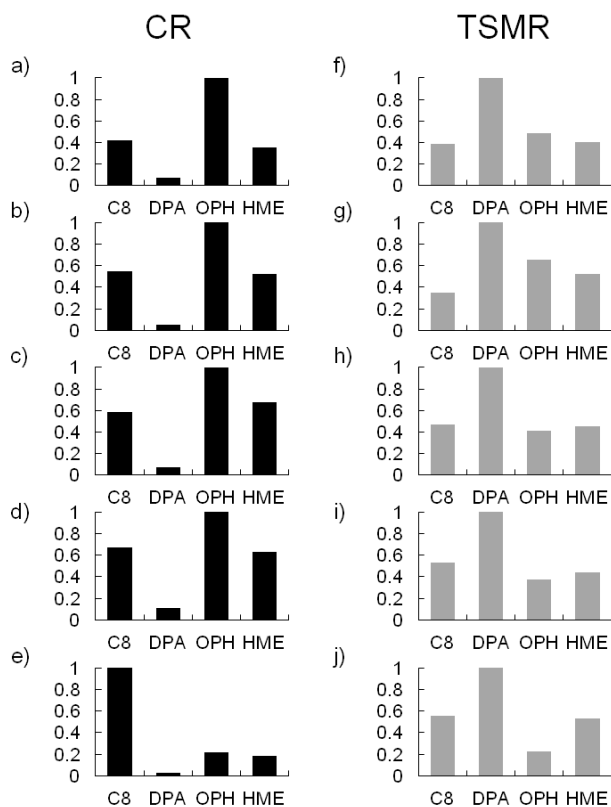
Figure 3-1. Normalized sensitivities from the 4-ST$_{cr}$ (a-e) and 4-ST$_{tsmr}$ (e-h) arrays for the five test vapors: a,f) 2-butanone; b,g) nitromethane; c,h) toluene; d,i) n-propanol; and e,j) n-octane. Sensitivities are normalized to the sensor giving rise to the largest response.
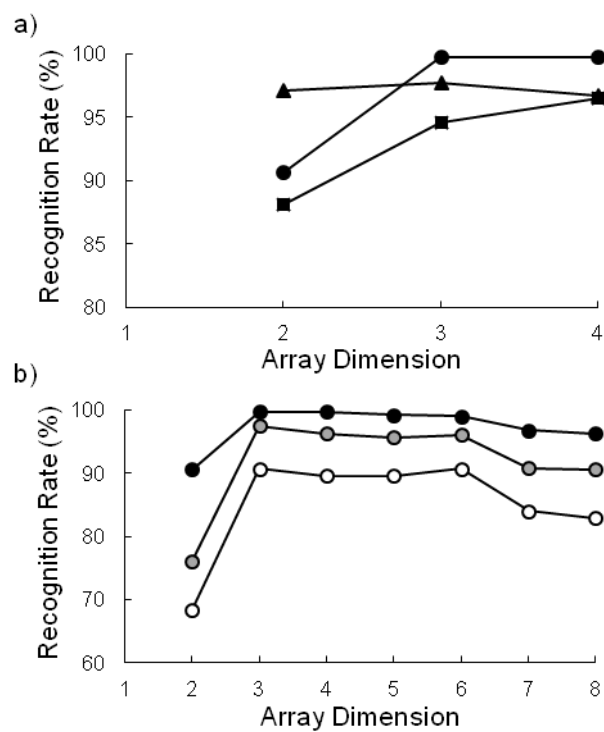
Figure 3-2. Recognition rates for individual-vapor discriminations from the best-performing arrays of each dimension: a) ST_{cr} arrays (filled squares), ST_{tsmr} arrays (filled triangles), and MT arrays (filled circles) (ε=5%); b) MT arrays for ε=5% (filled circles), 7.5% (shaded circles), and 10% (unfilled circles).

74
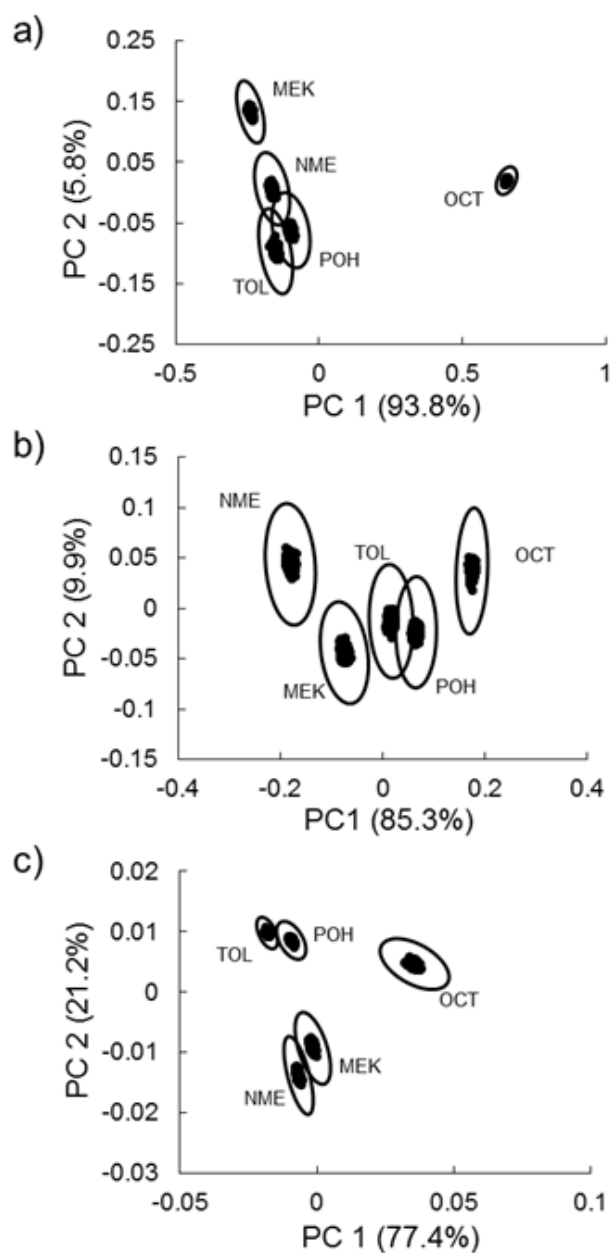
Figure 3-3. Principal components projections from the (a) 4-ST$_{cr}$, array (b) 4-ST$_{tsmr}$ array, and (c) best-performing 4-MT array (i.e., C8$_{tsmr}$+OPH$_{tsmr}$+HME$_{tsmr}$+HME$_{cr}$), derived from responses to the five test vapors. Data points are Monte-Carlo generated synthetic responses with $\varepsilon=1\%$ and ellipses represent the boundary of the 95% confidence interval with $\varepsilon=5\%$.
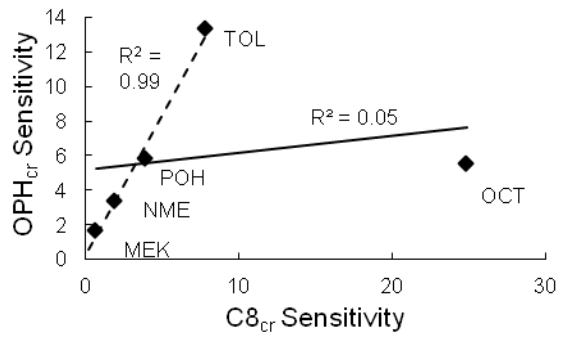
Figure 3-4. Plot of $C8_{cr}$ sensitivities vs. OPH_{cr} sensitivities ($\Delta R/R_b/\text{mg} \cdot \text{m}^{-3}$) for the five test vapors. Solid line shows the best-fit line from linear regression for all five vapors with corresponding R^2 value. Dashed line shows best-fit line from linear regression excluding the n-octane data point with corresponding R^2 value.
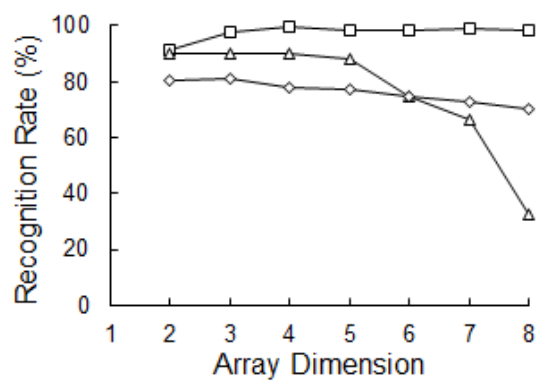
Figure 3-5. Recognition rates for a representative subset of three different binary vapor mixtures from the best-performing MT arrays of a given dimension (n = 2-8, ε=5%); TOL+OCT (unfilled squares); TOL+MEK (unfilled diamonds); NME+POH (unfilled triangles).

Chapter IV

Microfabricated Optofluidic Ring Resonator Structures

4.1 Introduction

The development of optical ring resonators as transducers for (bio)chemical analysis has been a topic of intensive investigation recently [1-2]. The optofluidic ring resonator (OFRR) is unique among the members of this class of sensors because it naturally integrates sensing and fluidic functions [3-6]. The OFRR consists of a narrow capillary, the (thinned) wall of which supports whispering gallery modes (WGMs) that circulate along the circumference and interact with analytes passing through the capillary. Over the past five years, OFRRs have been shown capable of highly sensitive label-free biosensing [3-4, 6-9] and vapor sensing [10-11].

Most OFRRs reported to date have been fabricated by one of two methods. The first involves drawing a capillary pre-form under heat [3-5]. While devices made in this way have yielded resonances with high Q-factors (i.e., $>10^6$), they are not well-suited for integration in lab-on-a-chip microsystems; only a single device is made at a time, there can be considerable variation in diameter and wall thickness, and the OFRRs tend to be fragile. The second method employs a strain-induced self-rolling process applied to semiconductor multi-layers [6, 12-15]. This method is amenable to mass production using standard microfabrication processes, and yields devices with precise and reproducible diameters and wall thicknesses. But Q-factors reported for devices made in this way have generally been low (i.e., 10^2-10^3) and the diameters, which are just a few

micrometers, pose significant challenges with respect to fluid throughput and interconnection with other components of integrated lab-on-chip microsystems in which we are interested.

In an attempt to address some of the shortcomings in existing OFRR designs, we have developed micromachined OFRR (µOFRR) structures suitable for ultimate integration in microanalytical systems such as the microscale gas chromatograph (µGC) prototypes on which we have reported recently [16-17]. Here, we describe the fabrication process and preliminary optical characterization of initial test structures as a prelude to evaluating their vapor sensitivity. Figure 4-1 shows a concept diagram of the basic configuration. Two designs were fabricated and tested: one with a straight-walled cylindrical shape, and one with a cylinder having an expansion region at its midsection, inspired by OFRR "microbubbles" [18-19] An etched alignment channel was incorporated beside the cylinder to facilitate intimate contact with the tapered optical fiber used to couple the laser light source and photodetector to the µOFRR. Focusing on the design with the midsection expansion, we measured the Q-factor and the free spectral range, *FSR*, of several devices of different diameters.

4.2 Fabrication

A detailed description of the fabrication procedure can be found in Appendix I. Fabrication entailed first creating high-aspect-ratio cylindrical wells in a <100> Si wafer by deep reactive ion etching (DRIE) through a photoresist mask. Then, a conformal layer of C_4F_8 ~1 µm thick was deposited, and subsequently removed from the floor of the etched wells using an extended anisotropic etch with SF_6. The masking layer of C_4F_8 remained on the sidewalls. In some devices the floors of the wells were then etched isotropically by XeF_2 at 3 torr to introduce an expansion in the cylinder. A second DRIE step continued the cylindrical fluidic path into the wafer with the original diameter. The initial photoresist mask and C_4F_8 layer were stripped in a bath of piranha

etch.   In the straight-walled devices a second lithographic step defined a photoresist mask on the back side of the wafer, and a final DRIE step was used to etch completely through the wafer.

For devices fabricated with the midsection expansion, a 2-µm thick conformal SiO_x layer was grown by means of an extended wet oxidation at 1100° C and then stripped in a bath of 1:1 HF and DI water. This step significantly reduced the surface roughness on the interior of the mold. Further details regarding the smoothing oxidation step can be found in Appendix II. Subsequently, a second 2-µm thick conformal SiO_x layer was grown and chemical/mechanical polishing was used to remove the SiO_x layer from the top surface of the wafer. Photoresist was then patterned to define a mask with openings for a 40-µm wide linear channel tangential to the cylinder, as well as annular trenches 90-240 µm wide (depending on cylinder diameter) surrounding the cylinder. These features were etched into the substrate with XeF_2 to a depth of 85 µm. Devices were then diced into chips 3×3 mm and cleaned to remove residual debris.

4.3 Optical characterization

To test the devices, a fused-silica optical fiber was tapered down to less than 2 µm in diameter over a 6 mm length by heating with a H_2 flame and pulling the fiber under constant tension with a set of motors. The fiber was glued across a fixture with parallel support surfaces and the fixture was secured to an adjustable stage with a Vernier micrometer (Series 462, Newport, Irvine CA) positioned above the µOFRR test chip. The fiber was lowered into the alignment channel in direct contact with the widest part of the µOFRR.

One end of the optical fiber was coupled to a 980 nm tunable diode-laser (Velocity 6320, New Focus, Irvine CA) and the other to a large-area IR photodetector (2033, New Focus, Irvine CA). Maintaining the laser output power between 2-6 mW, the wavelength was swept automatically from 980-990 nm at 0.25 nm/s and the detector voltage and wavelength were logged

on a laptop computer running a custom LabVIEW data acquisition program (National Instruments, Austin TX). Since the laser output and photodetector sensitivity varied independently with the wavelength, immediately following each measurement the fiber was decoupled from the device and a baseline sweep was recorded. Three devices of each diameter were tested.

Discrete data from the photodetector were interpolated into a continuous function of laser wavelength and then divided by the baseline signal to extract the resonant waveform, which was subsequently normalized as a fraction of the maximum transmitted intensity. The full width at half maximum (FWHM) and center wavelength (i.e., the wavelength of minimum transmitted intensity) of each resonance were measured following curve fitting to a Lorentzian function using Origin® software (OriginLab Corp., Northampton MA).

The Q-factor (i.e., center wavelength/FWHM), was evaluated for each device at each resonant wavelength within the 980-990 nm window. The average Q-factor for a given device was determined from all of the measured resonances and then averaged for the three devices of a given diameter. The *FSR* was calculated as the average difference between the center wavelengths of successive resonances for devices of a given diameter. The resonant cavity length was taken as the circumference of the cylinder measured along the widest part of the structure by SEM. By assuming a pure circulating mode, the effective ring radius, *r*, was calculated for each device from each measured *FSR* as $r = \lambda^2/(2\pi nFSR)$, where the index of refraction, *n*, for the thermal SiO_x was taken as 1.46 [20], and λ is the center wavelength of resonance. The average r value was then calculated.

Figure 4-2 shows SEM images of one representative μOFRR of each design. The μOFRR chips were easily manipulated, transported, and tested without breakage. The straight-walled cylindrical structures (Figure 4-2a) were made first and served to demonstrate the feasibility of the

fabrication process; however, tests of several devices failed to yield any resonances. We speculated that optical modes were propagating vertically from the point of contact and dissipating into the Si frame. So, a second set of devices was fabricated with midsection expansions, on the basis of previous reports suggesting that such contours can provide effective confinement of optical resonances [21-22]. These devices similarly failed to yield measurable resonances. Since SEM images revealed significant interior surface roughness and characteristic etch damage, our attention was drawn to this feature as a possible cause of device failure, and a third set of devices having midsection expansions was fabricated with an extra oxidation step added to smooth the interior surface prior to final growth of the μOFRR structures. These devices produced sharp resonances, and were amenable to further characterization.

The average Q-factor among all of the devices tested was 12,600, corresponding to a *FWHM* of 74 pm for a resonance centered at 985 nm. For devices with inlet diameters of 50, 100, 150 and 200 μm (midsection diameters of 73, 131, 184, and 239 μm, respectively), the average Q-factors were 9,300, 12,700, 15,000, and 13,500, respectively, which are apparently limited by the residual surface roughness incurred during the microfabrication. Relative standard deviations ranged from 17-34% indicating fairly good reproducibility. While the Q-factors observed here are lower than that of drawn-capillary OFRRs [23], they are comparable to those of planar ring-resonators used successfully as sensors of biomolecules [24] and volatile organic compounds [25]. (Note that another attribute of this μOFRR design is its use of SiO_x as the resonator material, which affords chemical inertness and low transmission loss over a wide range of wavelengths. SiO_x is not suitable for planar resonator designs because of strong coupling to the Si substrate.)

FSR values derived from the spacing of the resonances (e.g., Figure 4-3b) ranged from 0.87 to 2.76 nm for the largest and smallest devices, respectively. The radii (cavity lengths) calculated

on the basis of these measured *FSR* values differed by < 2% from those determined by SEM measurements of the device dimensions, indicating that pure circulating WGMs are being successfully confined within the midsection expansion regions of the devices.

4.4 Conclusion

In summary, we have demonstrated a facile process for creating hollow, three-dimensional SiO_x µOFRR structures with Q-factors exceeding 10^4. Measurements of the *FSR* confirm the presence of circulating WGMs similar to those induced in planar ring resonator devices. Advantages of this design over current drawn-capillary OFRRs include greater dimensional precision and ruggedness, batch fabrication, smaller size, thinner walls, and integral fiber-probe alignment, all of which should facilitate the implementation of µOFRR-based detectors in µGC and other lab-on-a-chip platforms. On-going work is focused on further reducing interior surface roughness, integrating micromachined fluidic interconnects with devices having completed fluidic channels, and testing vapor response characteristics with various sorptive interfacial films.

4.5 References

1 .   F. Vollmer and S. Arnold, *Nature Methods* **2008**, *5*, 591-596.
2 .   Y. Sun and X. Fan, *Anal. Bioanal. Chem.* **2011**, *399*, 205-211.
3 .   I. M. White, H. Oveys and X. Fan, *Opt. Lett.* **2006**, *31*, 1319-1321.
4 .   V. Zamora, A. Diez, M. V. Andres and B. Gimeno, *Opt. Express* **2007**, *15*, 12011-12016.
5 .   M. Sumetsky, Y. Dulashko and R. S. Windeler, *Opt. Lett.* **2010**, *35*, 898-900.
6 .   A. Bernardi, S. Kiravittaya, A. Rastelli, R. Songmuang, D. J. Thurmer, M. Benyoucef and O. G. Schmidt, *Appl. Phys. Lett.* **2008**, *93*, 094106.
7 .   H. Zhu, P. S. Dale, C. W. Caldwell and X. Fan, *Anal. Chem.* **2009**, *81*, 9858-9865.
8 .   X. D. Fan, S. I. Shopova, H. Y. Zhou and P. Zhang, *Applied Physics Letters* **2007**, *90*.
9 .   X. D. Fan, Y. Z. Sun, S. I. Shopova, C. S. Wu and S. Arnold, *Proceedings of the National Academy of Sciences of the United States of America* **2010**, *107*, 16039-16042.
10 .   S. I. Shopova, I. M. White, Y. Sun, H. Zhu, X. Fan, G. Frye-Mason, A. Thompson and S.-J. Ja, *Anal. Chem.* **2008**, *80*, 2232-2238.

11 .   Y. Sun, J. Liu, D. J. Howard, X. Fan, G. Frye-Mason, Shiou-jyh Ja and A. K. Thompson, *Analyst* **2010**, *135*, 165-171.
12 .   S. Vicknesh, F. Li and Z. Mi, *Appl. Phys. Lett.* **2009**, *94*, 081101.
13 .   I. S. Chun, K. Bassett, A. Challa and X. Li, *Appl. Phys. Lett.* **2010**, *96*, 251106.
14 .   E. J. Smith, S. Schulze, S. Kiravittaya, Y. Mei, S. Sanchez and O. G. Schmidt, *Nano Letters* **2010**, 11, 4037-4042.
15 .   G. S. Huang, V. A. B. Quinones, F. Ding, S. Kiravittaya, Y. F. Mei and O. G. Schmidt, *Acs Nano* **2010**, *4*, 3123-3130.
16 .   C. J. Lu, W. H. Steinecker, W. C. Tian, M. C. Oborny, J. M. Nichols, M. Agah, J. A. Potkay, H. K. L. Chan, J. Driscoll, R. D. Sacks, K. D. Wise, S. W. Pang and E. T. Zellers, *Lab on a Chip* **2005**, *5*, 1123-1131.
17 .   S.K. Kim, H. Chang and E.T. Zellers, *Analytical Chemistry*, **2010**, 83, 7198
18 .   M. Sumetsky, Y. Dulashko and R. S. Windeler, *Optics Letters* **2010**, *35*, 898-900.
19 .   H. Li, Y. B. Guo, Y. Z. Sun, K. Reddy and X. D. Fan, *Optics Express* **2010**, *18*, 25081-25088.
20 .   W. M. Haynes and D. R. Lide, *CRC handbook of chemistry and physics*, Taylor & Francis Group, Gaithersburg, **2010**, p.
21 .   M. Sumetsky, *Optics Letters* **2004**, *29*, 8-10.
22 .   Y. Louyer, D. Meschede and A. Rauschenbeutel, *Physical Review A* **2005**, *72*.
23 .   Y. Z. Sun, S. I. Shopova, G. Frye-Mason and X. D. Fan, *Optics Letters* **2008**, *33*, 788-790.
24 .   A. Yalcin, K. C. Popat, J. C. Aldridge, T. A. Desai, J. Hryniewicz, N. Chbouki, B. E. Little, O. King, V. Van, S. Chu, D. Gill, M. Anthes-Washburn and M. S. Unlu, *Ieee Journal of Selected Topics in Quantum Electronics* **2006**, *12*, 148-155.
25 .   N. A. Yebo, P. Lommens, Z. Hens and R. Baets, *Optics Express* **2010**, *18*, 11859-11866.
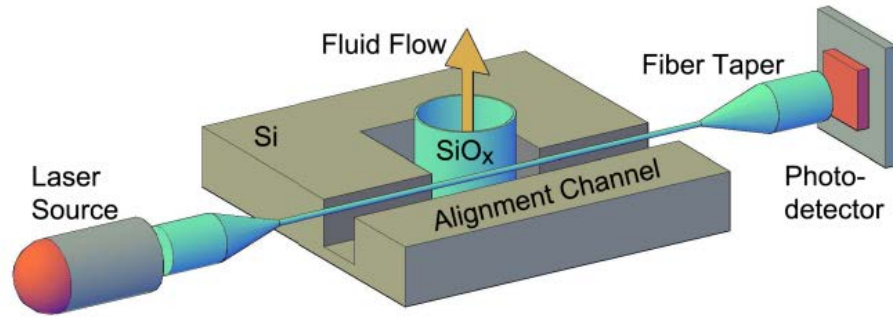
Figure 4-1. Diagram illustrating the basic structure and operation of the μOFRR.

(a)

50 µm

(b)

100 µm
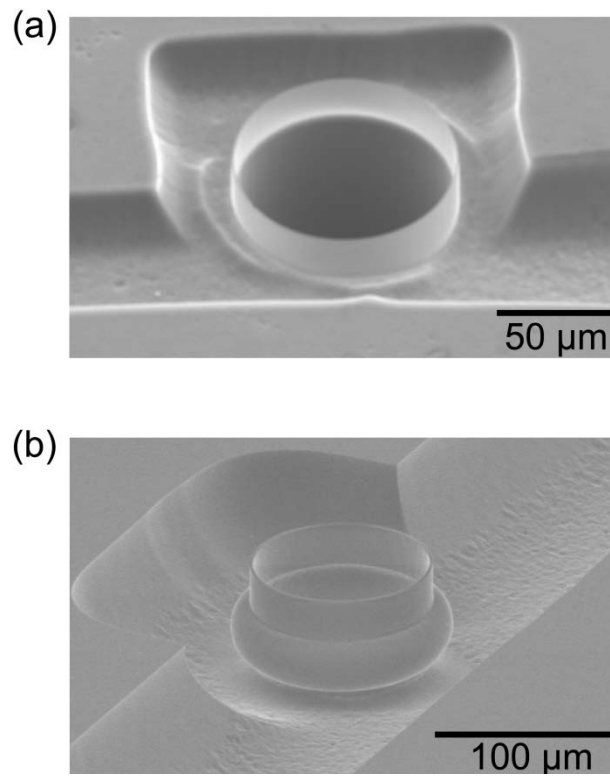
Figure 4-2. SEM images of µOFRRs with embedded fiber-optic alignment channel: a) 100-µm diameter straight-wall µOFRR; b) 100-µm diameter µOFRR with mode confinement feature.
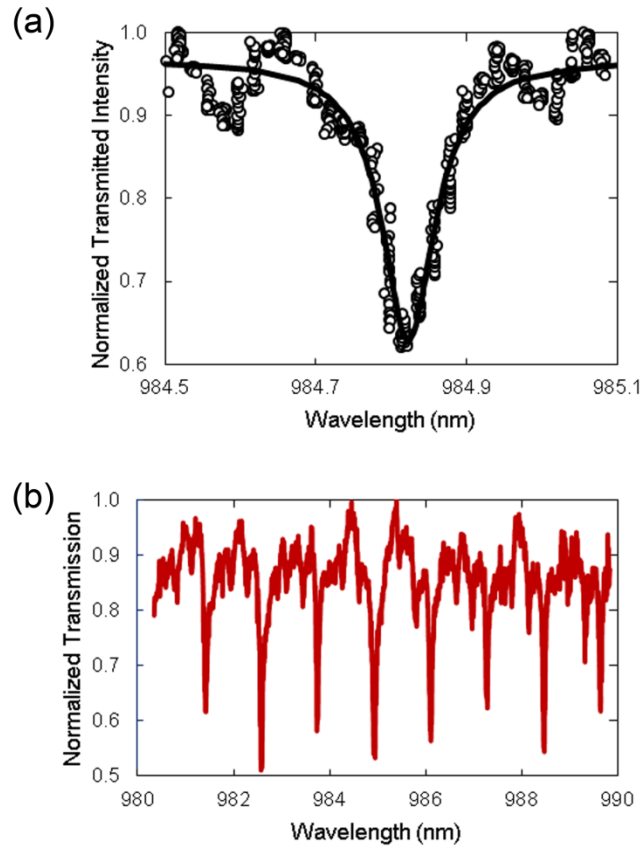
Figure 4-3. a) Normalized WGM resonance centered at 984.83 nm generated in a 200-µm diameter µOFRR with midsection expansion (239 µm). Smooth curve represents the fit of the data to a Lorentzian function; b) Normalized transmission across a fiber waveguide coupled to a 150-µm diameter µOFRR during 10 nm wavelength sweep of the laser source.

Chapter V

A Microfabricated Optofluidic Ring Resonator for Sensitive, High-Speed Detection of Volatile Organic Compounds

5.1 Introduction

Advances in photonics have yielded a new class of sensors adapted from whispering-gallery-mode (WGM) resonators [1-2]. These devices confine light at resonant wavelengths (λ_{WGM}) determined by the resonator material and dimensions, and the refractive index (RI) of the medium near the waveguide surface. Shifts in λ_{WGM} from changes in the composition of a bulk fluid [3-4], binding to surface-immobilized bio-receptors [5], or partitioning into a sorptive surface layer [6-7], afford label-free, RI-based detection of biological and chemical analytes. The typical sensor configuration comprises a narrow Si ridge in the shape of a loop (i.e., a micro-ring) that is sealed within a flow cell [4-5, 7], but sensors have also been made from disk [8] and toroidal [9] resonators on planar substrates. Although most commonly applied to liquid-phase analyses [1, 3-5, 8, 10], brief reports on gas-phase detection of single volatile organic compounds (VOC) with optical micro-ring resonators have also appeared [6-7]. The latter exhibit rather low sensitivities and long response times. Moreover, no studies of these devices have yet addressed the challenges of efficiently packaging the gas-phase fluidic and sensing components or integrating them into gas chromatographic microsystems (μGC) suitable for analyzing the trace-level components of complex VOC mixtures encountered in most real-world environmental or clinical applications.

The optofluidic ring resonator (OFRR) is a variant of such sensors that incorporates sensing and fluidic transport features into a single structure [11-14]. In such devices, WGMs are excited in the narrowed wall of a dielectric capillary by a coupled external waveguide. The evanescent component of the WGM extends into the fluid filled interior of the OFRR, and changes in RI within the evanescent field at the inner surface cause a shift in λ_{WGM} according to the following expression [13]: $\Delta\lambda_{WGM} = 2\pi r \Delta n_{eff}/m$, where r is the radius of the OFRR, m is an integer specifying the mode number, and n_{eff} is the effective RI that takes into account of the mode distribution in the air, wall, surface layer and fluid.

The first reported OFRR sensors were fabricated from heat-drawn glass capillaries that were etched to further thin the wall and then lined with sorptive polymer films [11-13]. Shifts in λ_{WGM} would occur from changes in the polymer film thickness and/or RI accompanying reversible partitioning of VOC analytes flowing through the capillary. With Q-factors as high as 10^6 and inner diameters ≤ 100 μm, such OFRRs could serve as sensitive, stand-alone VOC sensors [11], and as detectors downstream from conventional GC separation columns for the analysis of VOC mixtures [12, 14]. However, such OFRRs are not well-suited for microsystem integration because they are fragile and cumbersome, their diameters and wall thicknesses are difficult to control, and they are not amenable to batch fabrication either as individual sensors or as multi-sensor arrays. The enticing prospect of integrating OFRR detectors into μGC instrumentation demands an alternative design.

Here we introduce a fully functional *microfabricated* optofluidic ring resonator (μOFRR) sensor that addresses the limitations of capillary-based OFRR designs and has performance characteristics rivaling or exceeding those of other microsensor technologies that have been studied as (μ)GC detectors [15-28]. Fabricated from Si by batch-scalable micromachining

techniques, the device we describe here integrates a PDMS-coated, 250-µm i.d SiO_x µOFRR cylinder, a microfluidic interconnection channel, capillary insertion port, and an optical-fiber alignment structure on a 4-cm^2 Si chip. A quasi-toroidal expansion contour in the center of the cylinder serves to confine WGMs within a narrow region of the cylinder, thereby increasing sensitivity and reducing the effective sensing volume to ~45 pL. This device represents a refinement of µOFRR test structures described in Chapter 4 and previous publications [29], which had cylinder diameters ranging from 50 to 200 µm, wall thicknesses of ~2 µm, and Q-factors ranging from 9,200 to 15,000 (comparable to planar Si ring-resonator sensors [30]); those structures lacked a complete fluidic pathway (i.e., the floor of the cylinder was still intact) and they had not been coated or tested as VOC sensors. Note that this µOFRR differs from recently reported OFRRs produced by strain-induced self-rolling of SiO/SiO_2 bilayers [31-32], which have been adapted as on-chip detectors for liquid-phase analytes; with inner diameters of ~10 µm and comparatively low Q-factors. Such devices are not suitable for vapor detection or µGC integration.

After briefly describing the key features of the µOFRR chip design and operation, results of vapor-phase calibrations with five common VOCs are presented under steady-state conditions, and relative sensitivities are assessed with respect to the relative contributions of polymer swelling and RI changes. We then demonstrate the rapid responses and low limits of detection (LOD) achievable with the µOFRR sensor under transient exposure conditions, and finally show a high-speed separation of a simple VOC mixture with the µOFRR installed downstream from a µGC column.

5.2 Experimental methods

5.2.1. Materials

All test compounds were used as received (99% purity). Relevant physical properties are listed in Table 5-1. PDMS was obtained from Ohio Valley Specialty Company (OV-1, Marietta, OH).

5.2.2. Sensor fabrication

The sensor fabrication is described in greater detail in Appendix I. µOFRR devices were fabricated from Si by a combination of dry isotropic etching, deep reactive ion etching (DRIE), and thermal oxidation steps, as described in Chapter 4 and previous publications [29]. The DRIE cylindrical resonator extends through the Si substrate. It expands from 250 to 310 µm i.d. in a quasi-toroidal shape along its midsection. Successive oxidation steps reduced surface roughness and a final oxidation grew the SiO_x structure to the desired 1.2 µm thickness. It was partially released from its Si "mold" by an isotropic plasma etch. A DRIE alignment channel runs laterally across the entire 2×2 cm chip and facilitates tangential contact of the thinned optical fiber with the expanded section of the µOFRR cylinder (see Figure 5-1).

Fluidic interconnection structures include a tapered DRIE channel ($\sim380 \times 380 \times 5000$ µm) on the backside of the chip that secures the inserted capillary and conducts gas flow through a microfluidic path ($250 \times 250 \times 5000$ µm) to the backside aperture of the µOFRR. Following PDMS film deposition (see below), a 2×2 cm Pyrex cover plate was affixed to the backside of the chip with UV-curable adhesive to seal the fluidic channel. A short segment of deactivated fused-silica capillary (250 µm i.d.) was inserted in the channel and sealed with epoxy.

To coat the device (prior to applying the backside cover plate), the sensor chip was inverted and gently pressed into a rubber septum to form a tight seal. Then 10 µL of a 2.3 mg/mL solution

of PDMS in toluene was deposited over the backside port. The chip was placed in a vacuum chamber that was evacuated to allow the PDMS solution to fill the resonator cavity. Following evaporation of the solvent a ~300 nm layer of PDMS remained on the internal wall of the µOFRR (assuming uniform deposition). The presence of the film was apparent from the change in the appearance of the resonator expansion section by optical microscopy.

WGM resonances were excited by evanescently coupling to a 1550-nm laser source (CQF939/251, Philips, Amsterdam, NE) sweeping 375 pm at 10 Hz. An unclad section of an optical fiber (SMF-28, Corning Inc., Corning, NY) was drawn over a flame and tapered to ~1 µm o.d. [11]. The untapered segments of the fiber were glued to a horizontal frame, which was secured to an adjustable stage with a Vernier micrometer, and the tapered segment of the fiber was lowered into the alignment channel in direct contact with the expanded section of the µOFRR cylinder. The proximal end of the fiber was connected to the laser and the distal end of the fiber directed at an IR photoreceiver (Model 2033, New Focus, Irvine, CA). The power required to operate the detection system was very low: the µOFRR sensor is passive, the laser required < 30 mW from a bench scale power supply, and the photoreceiver was operated from a 9V battery.

5.2.3. Testing

Each WGM resonance formed a Lorentzian trough in the transmitted intensity; λ_{WGM} was defined as the wavelength of minimum transmission and recorded along with the FWHM value of the resonance. The shift of λ_{WGM} was monitored during VOC exposures. Responses of the µOFRR sensor were recorded for each of five VOCs individually over a 50-fold range of concentration. Test atmospheres were prepared in 3-L Tedlar® bags. Concentrations were confirmed by injecting aliquots into a pre-calibrated GC (Model HP-5890, Agilent Technologies, Palo Alto, CA) equipped with a 30-m PDMS-coated capillary column and flame-ionization detector (FID). The minimum

concentration ranged from 5 (m-xylene) to 68 (benzene) mg/m^3 (1.2 – 21 ppm). Samples from the test atmosphere were drawn into in a 1-mL sampling loop via a 6-port valve and injected through a 10-cm segment of deactivated fused silica capillary (100-µm i.d.) into the µOFRR sensor in dry air at 3 mL/min. This resulted in exposure times of ~20 s, which was sufficient for responses to reach steady state. Five replicates were measured at each of five or six bag concentrations of each VOC. Subsequently, tests with m-xylene were repeated with a 5-µL sample loop (3 mL/min) to evaluate responses to transient exposures.

The µOFRR sensor was then connected by deactivated capillary to an upstream separation µcolumn comprising 3.1 × 3.1 cm Si chip containing a 3-m-long DRIE square-spiral channel with a wall coating of PDMS [33-34]. The µcolumn was held at 63 °C using an on-chip resistive heater, and the µOFRR was at room temperature (~22 °C). A test atmosphere containing a mixture of benzene, toluene, n-octane and m-xylene was drawn through the 5-µL sample loop and injected into the µcolumn in dry air at 1.4 mL/min. Injected masses ranged from 20 (m-xylene) to 100 (benzene) ng.

5. 3 Results and discussion

5.3.1. VOC calibrations

Figure 5-1a illustrates the features and the operating configuration of this new µOFRR sensor. Figure 5-1b shows an SEM image of the µOFRR with an adjacent optical-fiber probe, prior to PDMS coating application, and Figure 5-1c shows a photograph of the entire chip with an external capillary affixed to the inlet port. The image shown in Figure 5-1d is a photomicrograph of the capillary installed in the Pyrex-capped, tapered channel on the backside of the µOFRR chip.

Figure 5-2 shows an isolated WGM mode at 1550 nm. The average Q-factor of the uncoated µOFRR, defined as the ratio of λ_{WGM} to the full-width-at-half-maximum (FWHM) value

of each of the resonances, was 11,500. It was unchanged following deposition of the PDMS film, which indicates a negligible optical loss of the mode resulting from PDMS absorption. This Q-factor is lower than those reported for some capillary-based OFRRs, most likely due to residual surface roughness from etching, despite successive oxidation steps intended to reduce such roughness. However, the line-width is sufficiently narrow to resolve small shifts in λ_{WGM}.

All vapor exposures caused red shifts in λ_{WGM} that were completely reversible. The rise and fall times for a given vapor exposure were remarkably short in all cases: < 2.5 s and 5.8 s, respectively, to and from steady-state. The lower inset in Figure 5-3a shows the response profile for 700 mg/m^3 (i.e., 190 ppm) of toluene vapor, which is typical of all profiles for the ~20 s exposures employed. Figure 5-3a presents the individual calibration curves for the five VOCs on the basis of steady-state responses. Replicate responses were highly reproducible (RSD ≤ 3%) and all curves were linear (R^2 > 0.99, forced zero y-intercept). Calculated slope sensitivities are presented in Table 5-1.

LODs, defined as 3σ/sensitivity, where σ (= 0.131 pm) is the standard deviation of the baseline signal, range from 2.2 to 22 mg/m^3 (0.51 to 6.9 ppm) among the five VOCs (Table 5-1). These steady-state LODs are 1-2 orders of magnitude lower than those reported for ethanol (vapor pressure, p_v = 8.8 kPa) with a polyethylene glycol coated capillary-based OFRR under similar exposure conditions [11]. Although several factors can affect LODs (see below), the thinner wall and mode confinement feature of the μOFRR, which increase the proportion of the WGM evanescently probing the PDMS film, undoubtedly contribute to the higher sensitivity observed.

5.3.2. Sensor mechanisms

Thermodynamically, the extent of partitioning into a non-polar polymer such as PDMS should be inversely proportional to the p_v value of the VOC [35]. Accordingly, using published

94

values of the partition coefficient, *K*, in PDMS (Table 5-1) for the analytes tested here, a plot of p_v vs. K is linear ($r^2 = 0.997$). By regressing sensitivity values (Table 5-1) onto those published K values, we can explore the extent to which the vapor pressures of the VOCs affect their μOFRR responses. Figure 5-3b presents such a plot. As shown, the aromatic compounds fall along the same trend line ($r^2 = 0.986$), while the alkane, n-octane, falls well below the line. This indicates that the relative responses among the aromatic vapors vary in proportion to their p_v values, whereas the relative response to n-octane vapor is affected by other factors.

To better understand this, we can express the response of the μOFRR as a function of two terms, as follows [13]:

$$\Delta\lambda_{WGM} = \frac{\partial\lambda_{WGM}}{\partial n_{PDMS}}\Delta n_{PDMS} + \frac{\partial\lambda_{WGM}}{\partial t}\Delta t \qquad \text{Eq. 5-1}$$

where *t* is the PDMS film thickness. Assuming that the evanescent field of the WGM extends into the interior beyond the PDMS coating, then $\partial\lambda_{WGM}/\partial t$ would be non-zero, because film swelling would increase the portion of the WGM in the PDMS, which has a higher RI value than that of air, regardless of the RI of the vapor. For operation in such a "thin-film" regime [36], the second ("swelling") term of Eq. 5-1 would always be positive, and λ_{WGM} would be red-shifted. Since we know that $\partial\lambda_{WGM}/\partial n_{PDMS}$ is finite and positive, the contribution of the first ("RI-shift") term of Eq. 1 to the net response depends on the RI value of the vapor relative to that of the PDMS: a vapor with a higher RI will red-shift λ_{WGM} while a vapor with a lower RI will blue-shift λ_{WGM}. In the former case the response due to swelling would be enhanced and in the latter case it would be diminished.

As stated above, red-shifts in λ_{WGM} were observed upon exposure to all vapors. The RI values (Table 5-1) for the aromatic VOCs are similar (i.e., 1.493-1.501 RIU) and are all greater than that of PDMS (i.e., 1.404 RIU) [37]. In contrast, the RI of n-octane (i.e., 1.394 RIU) is slightly

lower than that of PDMS. Thus, the sensitivities to the aromatic vapors are enhanced to a similar extent over that expected on the basis of swelling alone, whereas the sensitivity to n-octane is unaffected or slightly diminished. It is for this reason that the n-octane sensitivity falls below the trend line in Figure 5-3b. This also provides presumptive evidence that the device is operating in the thin-film regime.

To quantify the contribution attributable to ΔRI we used the published K values, the absolute air concentrations, and the (liquid) densities of the test compounds to calculate their volume fractions, φ, in the PDMS. Swelling-normalized sensitivity values, in pm/φ, were then calculated: for n-octane the value is 26,000 pm/φ and for the aromatic compounds the average value is 68,300 pm/φ (ratio = 2.6), reflecting the enhancement from ΔRI for the latter compounds.

The relative contributions of swelling and ΔRI to the net response can be estimated via Eq. 5-1. Assuming that $\partial\lambda_{WGM}/\partial t$ and $\partial\lambda_{WGM}/\partial n_{PDMS}$ are constant over the range of φ values considered, then $\partial\lambda_{WGM}/\partial n_{PDMS}$ = 416,000 pm/RIU and $\partial\lambda_{WGM}/\partial t$ = 101 pm/nm. For a sorbed vapor with an RI value that is, say, 0.1 RIU greater than that of PDMS, the RI-shift term will be 1.4 times the swelling term in Eq. 5-1. For the range of RI values spanned by most VOCs, i.e., from 1.35 to 1.55 [38], a red shift in λ_{WGM} is predicted in all cases for this PDMS-coated μOFRR, as observed. Although these results are unique to the specific film thickness considered here, they highlight that the μOFRR is both a volumetric and refractometric sensor, and that sensitivity and selectivity depend on both the K value and the contrast between the RI values of the VOC and the selected sorbent.

5.3.3. Detection limits and response time

To characterize the μOFRR response under transient exposure conditions, a second calibration was performed with m-xylene using 5-μL (loop) vapor injections of a series of test

atmospheres into an air carrier gas flowing at 3 mL/min through the sensor. This flow rate is typical of those used for μGC analyses. Both peak height and peak area varied linearly with injected mass over the range tested (i.e., 0.18 to 5.3 ng). The inset of Figure 5-4 shows the peak-height calibration curve (R^2 = 0.997). The calculated sensitivity for m-xylene under these conditions is 23% of that obtained from the steady-state calibration, reflecting the degree to which sorption fell short of the equilibrium value under these dynamic exposure conditions. In spite of this, an LOD of 49 pg was calculated using the peak-height sensitivity value. This μOFRR LOD is ~100 times lower than that reported for n-decane (i.e., 4.5 ng) with a polymer-coated capillary-based OFRR installed as an in-line detector [12], despite the use of a split injection and a relatively high flow rate for the n-decane analysis (note: m-xylene was not tested in that study).

In comparing performance among different types of sensors used as GC or μGC detectors, it must be recognized that the LOD, which is calculated on the basis of peak height, depends as much on system operating parameters and vapor properties as it does on the inherent sensor response characteristics. Kinetic and thermodynamic factors are both important. Among structurally similar compounds, those with lower vapor pressures always have larger K values in sorptive sensor-interface films, leading to higher sensitivities and lower LODs, all other factors being equal. Affinity also affects K values and is determined by the compatibility of the respective functional groups of the analyte and the interface material. However, lower vapor pressures and stronger vapor-interface interactions also reduce the rate of desorption from the interface film, which tends to broaden peaks and raise the LOD. The length of time an analyte spends on the upstream separation (μ)column is also important, as peaks invariably broaden with increasing retention time. Of course, the injection bandwidth is yet another critical factor, with sharper injections leading to taller peaks and lower LODs. This is one reason why split injections are often

used to evaluate sensor sensitivities [20, 24-26]. Although a large fraction of injected sample mass is lost (vented) by use of a high injection split ratio, the injection band becomes very sharp and the *concentration* of the injected sample is (ideally) unaffected, which can provide a significant enhancement in peak-height sensitivity and a commensurate reduction in the apparent LOD. The effects of temperature and flow rate on the factors presented above can also be significant [21, 28, 39].

The LOD we calculated for m-xylene with the μOFRR above is 1-3 orders of magnitude lower than those of chemiresistor or surface-acoustic-wave microsensors employing sorptive nanoparticle or polymer interface layers that have been used as portable GC or μGC detectors under similar operating conditions [16-17, 21, 40-41]; reported LODs were in the range of 0.5-14 ng for m-xylene, though for peaks that were wider than those measured here by virtue of having been injected from an adsorbent preconcentrator and/or separated on an upstream (μ)column. The Fabry-Perot (FP) sensors explored as (μ)GC detectors by Reddy, et al. [24-26], were not tested with m-xylene, but an LOD of 200 pg for toluene was obtained by probing a PDMS film under conditions that gave a relatively broad toluene peak (i.e., FWHM ≈ 1 s) [24]. The toluene LOD was reduced by as much as ~20-fold in subsequent studies by use of a split injector providing nominal split ratios up to 10^4:1 to decrease the peak width significantly, while maintaining the relatively high flow rate (i.e., 8 mL/min) used in the earlier study [24-26]. μGC separations performed at lower flow rates with splitless injection, however, gave broader peaks and consequent reductions in the FP-sensor S/N ratios [26].

Thus, although only rough comparisons are possible, the available data suggest that the LOD achievable with our PDMS-coated μOFRR may be considerably lower than those of other microsensors used as (μ)GC detectors under typical operating conditions. Since the μOFRR

sensitivity varies with the fraction of the WGM in the PDMS film, a reduction in the LOD could be achieved ostensibly by either increasing the thickness of the PDMS film or decreasing the wall thickness of the μOFRR. However, increases in the PDMS film thickness might also lead to peak broadening due to slower sorption/desorption rates, and would reduce the component of the response attributable to film swelling (vida supra). The SiO_x wall thickness could be reduced with the fabrication method employed here, but this might compromise the structural integrity of the device, and it could also increase baseline noise and decrease the Q-factor [13]. We speculate that any reductions in LOD realized by such changes in device design would be marginal.

The widths of the peaks for m-xylene from the μOFRR sensor here were limited by the injection volume and flow rate; a splitless injection of 5 μL at 3 mL/min was employed. For reference, analyses were repeated under identical separation conditions with an FID installed in place of the μOFRR. The FID is considered to have 'zero' dead time and to serve as an ideal reference for assessing detector band broadening. Figure 5-4 shows the response profile for a 180-pg injection of m-xylene, and that for a larger injection (~500 pg) of m-xylene from the FID, where the latter profile has been scaled to the same peak height as the former (note: for reference, 180 pg would correspond to a 0.1-L preconcentrated air sample containing 40 parts-per-billion of m-xylene). As shown, the peak from the μOFRR (FWHM = 0.71 s) is just 18% broader than that from the FID (FWHM = 0.60 s).

This performance is consistent with that reported in other studies where reference FID responses were also collected; peaks from microsensors are invariably wider than the corresponding peaks from an FID due to the finite vapor sorption/desorption rates in microsensor interface films [12, 15, 18, 20, 40, 42-43]. Accordingly, the difference in FWHM values increases as the vapor pressure of the analyte decreases [12, 43]. Although the fidelity of the FWHM value

of the μOFRR peak to that of the FID for such a narrow peak is noteworthy, it is not unprecedented (see, for example, refs. 12 and 20; also see below), and, generally speaking, will depend on most of the same factors affecting determinations of LODs discussed above. Regardless, this demonstrates that the μOFRR has a very low effective dead volume and a rapid response, which are certainly important attributes for use in μGC systems, but perhaps even more important for use in μGC × μGC systems [44-45], where very narrow modulated peaks are produced and extra-column sources of band broadening must be strictly minimized. Further reductions in response time should be possible by decreasing the PDMS film thickness or the diameter of the μOFRR, but with commensurate reductions in sensitivity or increases in flow resistance, respectively.

5.3.4. Performance in μGC subsystems

The chromatogram shown in Figure 5-5 is an isothermal separation of four of the VOCs obtained with a microfabricated GC column chip coupled to the μOFRR sensor using dry air as the carrier gas at 1.4 mL/min. This is the first instance of an OFRR sensor used as the detector for a μGC separation. The VOCs are easily separated in 36 s and the peaks are symmetric and sharp (FWHM = 0.33 to 1.17 s), indicative of excellent response dynamics from the sensor. It is clear from the time required for elution of the first peak (i.e., benzene) that the separation could be accelerated by use of temperature programming, a shorter μcolumn, or a higher flow rate.

5.4 Conclusions

In summary, the μOFRR is a new microsensor with several attributes that augur well for its use in micro-analytical systems for trace-level VOC determinations. Compared to capillary-based OFRRs, the μOFRR design reduces the size, increases structural integrity, affords precise

control of resonator dimensions, and, by virtue of better mode confinement and thinner walls, yields higher sensitivity. The integration of on-chip microfluidics and fiber alignment structures in the device described here minimizes the dead-space along the flow path and facilitates system integration and packaging. Responses are consistent with theory and, as shown, can be parsed into contributions from swelling and RI changes of the polymer interface films upon reversible vapor sorption. The high sensitivity and rapid response time permits the detection of peaks < 1 s wide containing pg quantities of vapor at flow rates compatible with efficient chromatographic separations, which is unprecedented. These features will facilitate advancements in high-speed µGC and µGC×µGC systems for complex VOC analyses. Arrays of such sensors, lined with different sorptive interface materials and integrated on a common Si substrate, can be envisioned. The resulting response patterns produced by the eluting vapors would enhance the reliability of VOC determinations [16-17, 22, 25-27, 46]. In on-going work we are pursuing the construction of such arrays. We have also assembled a compact module comprising a small laser, a diode detector, and a µOFRR sensor with the fiber probe and capillary interconnect securely fixed in position, which we plan to use in tests with our latest µGC and µGC×µGC prototypes.

5.5 References

1 . F. Vollmer and S. Arnold, *Nature methods* **2008**, *5*, 591-596.
2 . X. Fan, I. M. White, S. I. Shopova, H. Zhu, J. D. Suter and Y. Sun, *analytica chimica acta* **2008**, *620*, 8-26.
3 . I. M. White, H. Zhu, J. D. Suter, N. M. Hanumegowda, H. Oveys, M. Zourob and X. Fan, *Sensors Journal, IEEE* **2007**, *7*, 28-35.
4 . J. Wang and D. Dai, *Optics letters* **2010**, *35*, 4229-4231.
5 . A. L. Washburn, L. C. Gunn and R. C. Bailey, *Analytical chemistry* **2009**, *81*, 9499-9506.
6 . A. Ksendzov, M. Homer and A. Manfreda, *Electronics Letters* **2004**, *40*, 63-65.
7 . N. A. Yebo, P. Lommens, Z. Hens and R. Baets, *Optics Express* **2010**, *18*, 11859-11866.
8 . E. Krioukov, D. Klunder, A. Driessen, J. Greve and C. Otto, *Optics letters* **2002**, *27*, 512-514.

9 .   J. Zhu, S. K. Ozdemir, Y.-F. Xiao, L. Li, L. He, D.-R. Chen and L. Yang, *Nature Photonics* **2009**, *4*, 46-49.
10 .   J. H. Wade and R. C. Bailey, *Analytical chemistry* **2013**, *86*, 913-919.
11 .   Y. Sun, S. I. Shopova, G. Frye-Mason and X. Fan, *Optics letters* **2008**, *33*, 788-790.
12 .   S. I. Shopova, I. M. White, Y. Sun, H. Zhu, X. Fan, G. Frye-Mason, A. Thompson and S.-j. Ja, *Analytical chemistry* **2008**, *80*, 2232-2238.
13 .   Y. Sun and X. Fan, *Optics express* **2008**, *16*, 10254-10268.
14 .   Y. Sun, J. Liu, D. J. Howard, G. Frye-Mason, A. K. Thompson, S.-j. Ja and X. Fan, *Analyst* **2010**, *135*, 165-171.
15 .   Q.-Y. Cai and E. T. Zellers, *Analytical chemistry* **2002**, *74*, 3533-3539.
16 .   C.-J. Lu, J. Whiting, R. D. Sacks and E. T. Zellers, *Analytical chemistry* **2003**, *75*, 1400-1409.
17 .   C.-J. Lu, W. H. Steinecker, W.-C. Tian, M. C. Oborny, J. M. Nichols, M. Agah, J. A. Potkay, H. K. Chan, J. Driscoll and R. D. Sacks, *Lab on a Chip* **2005**, *5*, 1123-1131.
18 .   C. Y. Lee, R. Sharma, A. D. Radadia, R. I. Masel and M. S. Strano, *Angewandte Chemie International Edition* **2008**, *47*, 5018-5021.
19 .   S. Zampolli, I. Elmi, F. Mancarella, P. Betti, E. Dalcanale, G. Cardinali and M. Severi, *Sensors and Actuators B: Chemical* **2009**, *141*, 322-328.
20 .   M. Li, E. Myers, H. Tang, S. Aldridge, H. McCaig, J. Whiting, R. Simonson, N. Lewis and M. Roukes, *Nano letters* **2010**, *10*, 3899-3903.
21 .   Q. Zhong, W. H. Steinecker and E. T. Zellers, *Analyst* **2009**, *134*, 283-293.
22 .   S. K. Kim, H. Chang and E. T. Zellers, *Analytical chemistry* **2011**, *83*, 7198-7206.
23 .   S. Narayanan and M. Agah, *Microelectromechanical Systems, Journal of* **2013**, *22*, 1166-1173.
24 .   K. Reddy, Y. Guo, J. Liu, W. Lee, M. K. Khaing Oo and X. Fan, *Sensors and Actuators B: Chemical* **2011**, *159*, 60-65.
25 .   K. Reddy, Y. Guo, J. Liu, W. Lee, M. K. K. Oo and X. Fan, *Lab on a Chip* **2012**, *12*, 901-905.
26 .   K. Reddy, J. Liu, M. K. K. Oo and X. Fan, **2013**.
27 .   W. R. Collin, G. Serrano, L. K. Wright, H. Chang, N. Nuñovero and E. T. Zellers, *Analytical chemistry* **2013**, *86*, 655-663.
28 .   R.-S. Jian, R.-X. Huang and C.-J. Lu, *Talanta* **2012**, *88*, 160-167.
29 .   K. Scholten, X. Fan and E. T. Zellers, *Applied physics letters* **2011**, *99*, 141108.
30 .   M. Zourob and A. Lakhtakia, *Optical Guided-wave Chemical and Biosensors II: II*, Springer, **2010**, p.
31 .   G. Huang, V. A. Bolaños Quiñones, F. Ding, S. Kiravittaya, Y. Mei and O. G. Schmidt, *Acs Nano* **2010**, *4*, 3123-3130.
32 .   S. M. Harazim, V. A. B. Quiñones, S. Kiravittaya, S. Sanchez and O. G. Schmidt, *Lab on a Chip* **2012**, *12*, 2649-2655.
33 .   S. Reidy, D. George, M. Agah and R. Sacks, *Analytical chemistry* **2007**, *79*, 2911-2917.
34 .   G. Serrano, S. M. Reidy and E. T. Zellers, *Sensors and Actuators B: Chemical* **2009**, *141*, 217-226.
35 .   A. Hierlemann, A. J. Ricco, K. Bodenhöfer, A. Dominik and W. Göpel, *Analytical chemistry* **2000**, *72*, 3696-3708.
36 .   A. M. Kummer, A. Hierlemann and H. Baltes, *Analytical chemistry* **2004**, *76*, 2470-2477.

37 . Ohio Valley Specialty Company, (2014, February 24). [Online]. Available: http://www.ovsc.com/.

38 . D. R. Lide in *CRC Handbook of Chemistry and Physics*, *Vol.* CRC Press, Boca Raton, USA, **2013**.

39 . L. Wright and E. Zellers, *Analyst* **2013**, *138*, 6860-6868.

40 . C.-J. Lu and E. T. Zellers, *Analytical chemistry* **2001**, *73*, 3449-3457.

41 . C. J. Lu, C. Jin and E. T. Zellers, *Journal of Environmental Monitoring* **2006**, *8*, 270-278.

42 . W. H. Steinecker, M. Rowe, A. Matzger and E. Zellers, *TRANSDUCERS, Solid-State Sensors, Actuators and Microsystems, 12th International Conference on, 2003* **2003**, pp. 1343-1346.

43 . C. J. Lu and E. T. Zellers, *Analyst* **2002**, *127*, 1061-1068.

44 . G. Serrano, D. Paul, S.-J. Kim, K. Kurabayashi and E. T. Zellers, *Analytical chemistry* **2012**, *84*, 6973-6980.

45 . W. R. Collin, A. Bondy, D. Paul, K. Kurabayashi and E. T. Zellers, *in final preparation*.

46 . M.-D. Hsieh and E. T. Zellers, *Analytical chemistry* **2004**, *76*, 1885-1895.

47 . P. J. Linstrom and W. G. Mallard in *WebBook, NIST Standard Reference Database Number 69*, *Vol.* National Institute of Standards and Technology, Gaithersburg, MD.

48 . P. A. Martos, A. Saraullo and J. Pawliszyn, *Analytical chemistry* **1997**, *69*, 402-408.

Table 5-1. Physical properties and steady-state sensor response parameters for all VOC analytes.[a]

VOC	RI[b]	ρ (g/ml)[b]	p_v (kPa)[c]	K_{PDMS}[d]	Sensitivity (pm/(mg/m³))	LOD (mg/m³:ppm)
benzene	1.501	0.877	12.0	296	0.018	22:6.9
toluene	1.494	0.867	3.78	817	0.070	5.6:1.5
ethylbenzene	1.493	0.867	1.25	2020	0.181	2.2:0.51
m-xylene	1.494	0.860	1.10	2190	0.174	2.3:0.53
n-octane	1.394	0.703	1.71	1486	0.055	7.2:1.5

[a] refractive index (RI), density (ρ), vapor pressure (p_v) and partition

coefficient (K) values at 25 °C; [b] ref. 38; [c] ref. 47; [d] ref.48
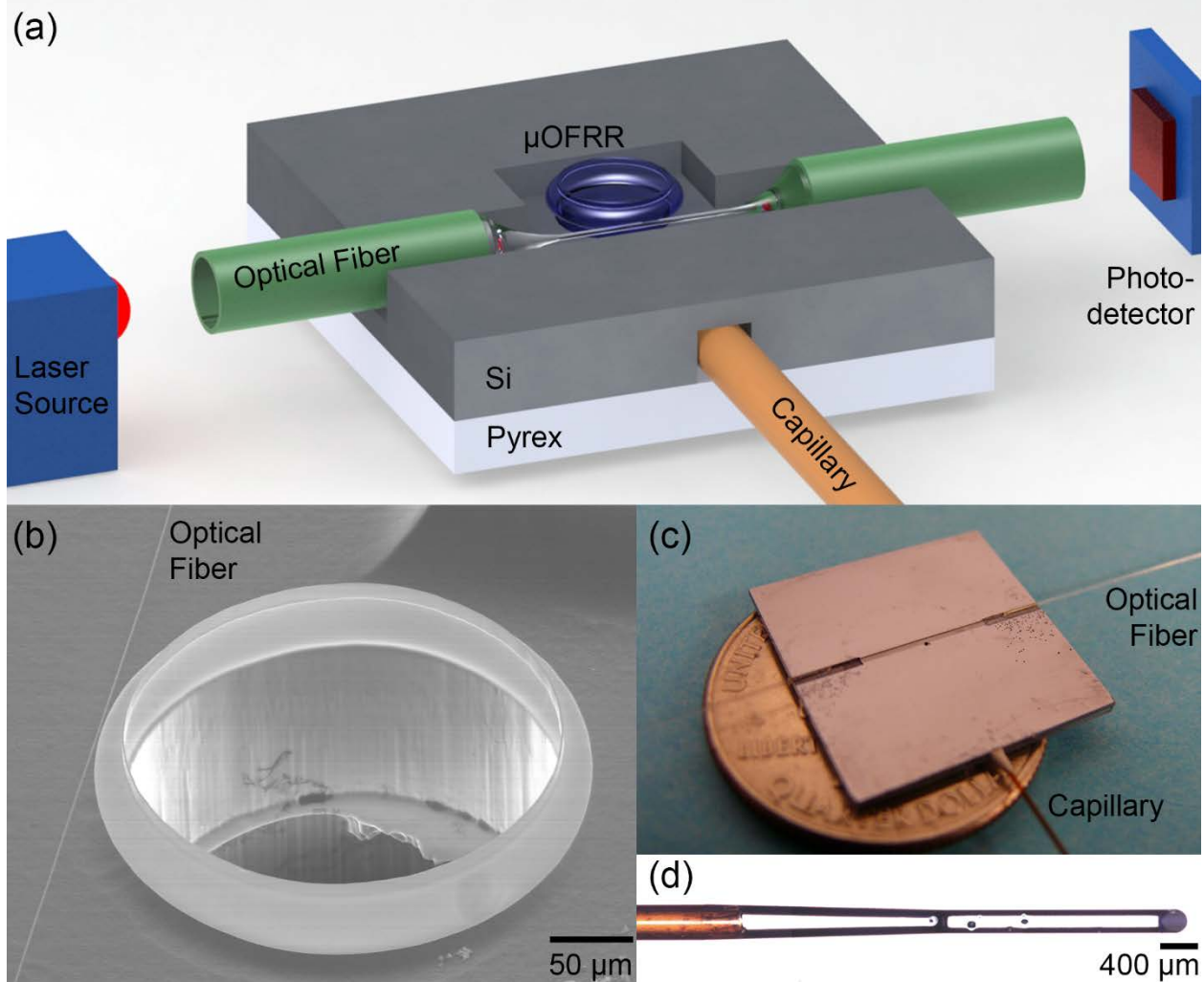
Figure 5-1. µOFRR sensor (a) Illustration depicting the µOFRR sensor in its operating configuration. (b) SEM image of µOFRR with tapered fiber (left) in contact with the toroidal expansion section. (c) Photograph of the µOFRR sensor chip with a fiber waveguide in the alignment channel and a capillary in the fluidic interconnection port. (d) Backside image of the µOFRR sensor chip showing a capillary (amber color to the left) inserted into the Pyrex-sealed fluidic intrconnection channel leading to the µOFRR inlet port to the right.
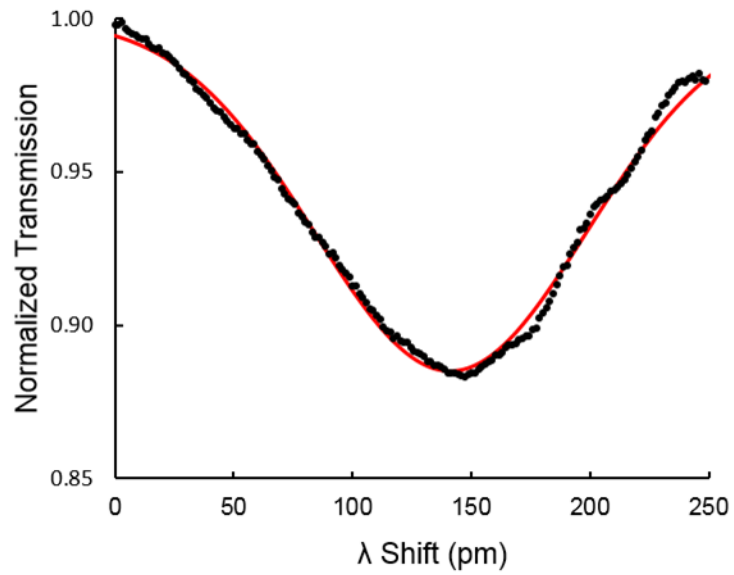
Figure 5-2. A normalized WGM resonance centered at 1550 nm generated in a PDMS coated μOFRR. Smooth (red) curve represents the fit of the data to a Lorentzian function. Q-Factor $(\lambda_{WGM}/FWHM_{WGM}) = 11,500$.
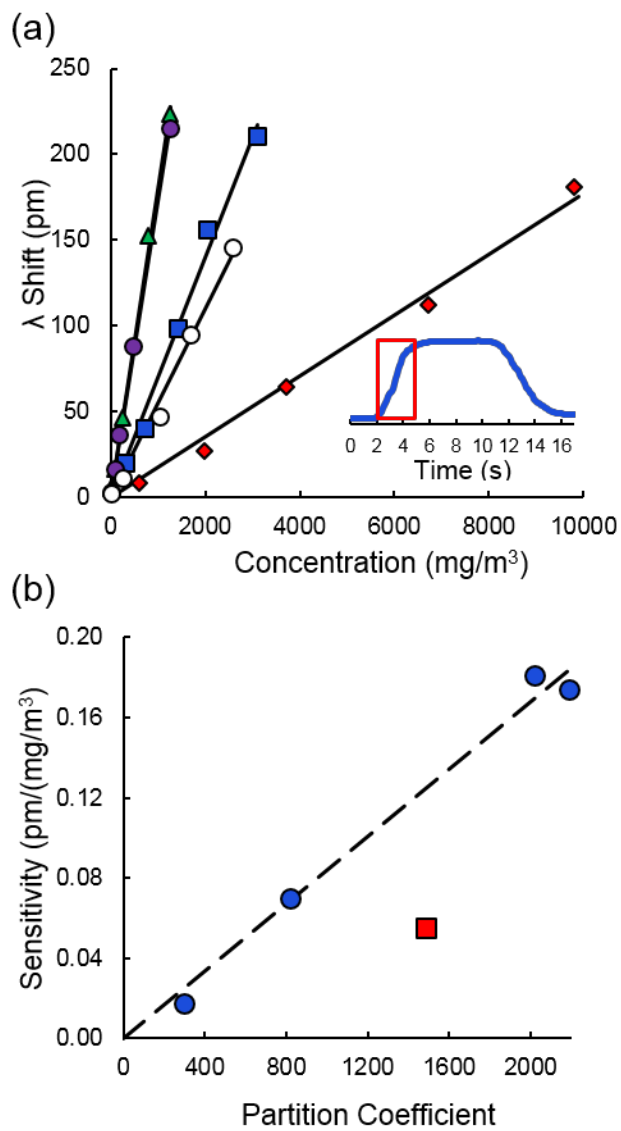
Figure 5-3. PDMS-lined μOFRR sensor responses to steady-state exposures. (a) Calibration curves for benzene (diamond), toluene (square), ethylbenzene (triangle), m-xylene (filled circle), and n-octane (unfilled circle) vapors. Each data point represents the average of 5 replicates. Inset shows the response profile to 700 mg/m^3 (190 ppm) of toluene; red square shows a rise time of less than 2.5 s. (b) Sensitivities of benzene, toluene, ethylbenzene and m-xylene (BTEX, blue circles) and n-octane (red square) as a function of their respective partition coefficients, K (Table 1). Trend line shows linear regression for the BTEX analytes.
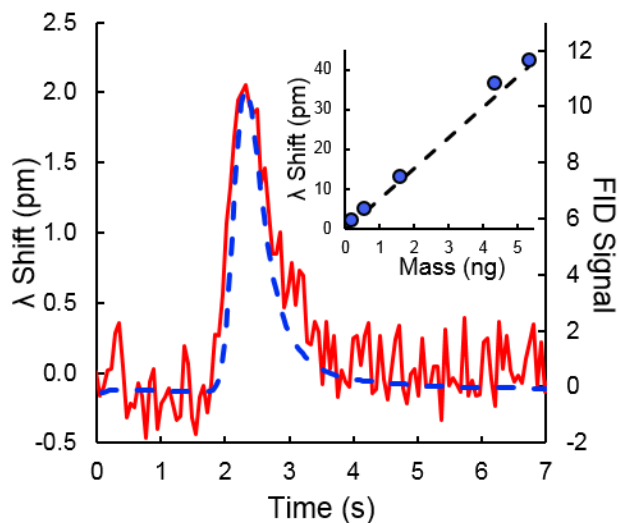
Figure 5-4. Rapid response of the μOFRR to transient VOC exposure. Response profiles from the μOFRR (solid red line, left axis) for a 180-pg injection of m-xylene vapor and the FID (dashed blue line, right axis) for a ~500-pg injection of m-xylene vapor under the same analytical conditions. The FID profile has been scaled down to match the peak maximum from the μOFRR for comparison of the FWHM values, which were 710 (μOFRR) and 600 ms (FID). Inset shows the μOFRR calibration curve for m-xylene from a series of similar injections at higher vapor concentrations.
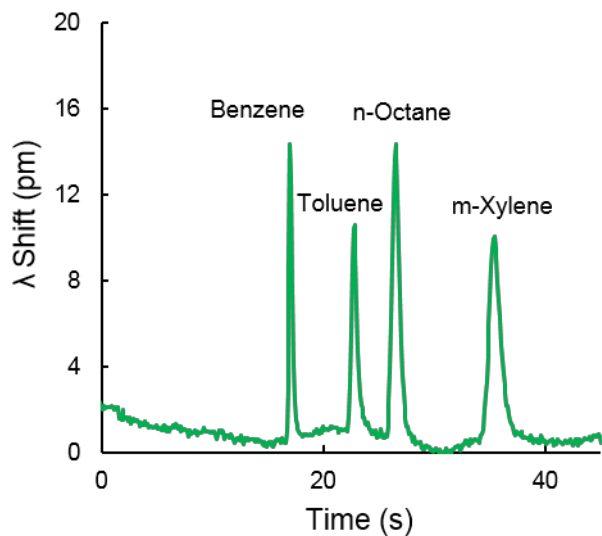
Figure 5-5. µGC separation with µOFRR sensor as detector. Separation of benzene, toluene, n-octane and m-xylene using a 3.1 × 3.1 cm µcolumn chip containing a 3-m long PDMS-coated channel at 63 °C and the (downstream) µOFRR sensor at 22 °C. Injected masses were approximately 53 ng (benzene), 21 ng toluene, 26 ng (n-octane), and 11 ng (m-xylene). Dry air at 1.4 mL/min was used as carrier gas.

Chapter VI

A Microfabricated Comprehensive Two-Dimensional Gas Chromatographic Subsystem Employing a Polymer-Coated Micro-Optofluidic Ring Resonator

6. 1 Introduction

Research over the past decade or so on Si-microfabricated gas chromatographic microsystems (μGC) has led to several improvements in design and operation, moving us closer to realizing low-cost, low-power instrumentation capable of analyzing the components of airborne volatile organic compounds (VOC) mixtures at low concentrations in near-real time [1-10]. Such air monitoring capabilities are not possible with stand-alone sensors or sensor arrays [11-12]. Unfortunately, the maximum lengths and minimum diameters of μGC separation columns are subject to practical constraints which, in turn, constrain the complexity of VOC mixtures that can be reliably analyzed by such microsystems.

Microscale comprehensive two-dimensional gas chromatography ($\mu GC \times \mu GC$) represents one approach to overcoming these limitations. By analogy with its macro-scale counterpart, in $\mu GC \times \mu GC$, a first-dimension (^{1}D) μcolumn is connected through a micro-scale thermal or pneumatic modulator to a shorter second-dimension (^{2}D) μcolumn that has retention properties

differing from those of the ^{1}D µcolumn. As the peak from each mixture component elutes from the ^{1}D µcolumn it is re-injected piecewise into the ^{2}D µcolumn at a rate high enough to maintain the ^{1}D elution sequence. Ideally, then, the peak capacity is increased significantly over thatprovided by a one-dimensional separation column of similar length, and both the resolution and detectability of the eluting peaks can be improved [13-14].

Thermal modulation offers some advantages over pneumatic modulation [ref]. It entails continuous, rapid thermal cycling during the course of an analysis: cooling to trap peak segments from the ^{1}D µcolumn and then heating to remobilize/reinject them into the ^{2}D µcolumn [15-16]. Kurabayashi, et al. developed the first microfabricated thermal modulator (µTM) [17]. It contains a series of two spiral Pyrex-capped deep-reactive-ion-etched (DRIE) Si microchannel sections (stages) with independent thin-metal-film heaters. Mounted just above a compact stack of thermoelectric coolers (TEC), this µTM can be heated to at least 250 °C and then cooled to $\leq$ -20°C in rapid succession. By virtue of the focusing that occurs in the modulator and the rapid subsequent injection, the modulated peak segments are compressed, which decreases their width and increases their height and leads to commensurate improvements in resolution and detectability.

Recently, this type of device has been used to perform GC × GC separations with conventional capillary columns [18-19] and µGC × µGC separations with microfabricated ^{1}D and ^{2}D columns [20], but in all cases using a conventional, bench-scale flame ionization detector (FID). Due to nature of the modulation process, the short length of the ^{2}D µcolumn, and the relatively high linear velocity of the carrier gas, the peaks generated at the outlet of separation module can be very narrow. Therefore, a detector with a low dead volume and short response time, such as the FID, is required. For ultimate application in field or clinical settings, a more compact, portable detector is needed.

Whiting et al. reported the first GC × GC analysis using microfabricated separation and detection components [21]. Micromachined separation columns and polymer coated cantilever sensors were used with a conventional pneumatic modulation valving system to achieve ultra-rapid separation and detection of dimethylmethylphosphonate in a mixture with three other VOCs. Other multi-dimensional separation subsystems made using microfabricated columns and different sensing technologies have been reported recently that embody different approaches to enhancing peak capacity in GC microsystems [22-23]. However, there has yet to be a report of a fully microfabricated µGC × µGC system encompassing microfabricated separation columns, sensor and modulator.

The microfabricated optofluidic ring resonator (µOFRR) sensor is a new sensor we recently developed and demonstrated as a µGC detector [24-25]. It is modeled after the OFRR sensors developed by Fan et al. using thinned glass capillaries, which have also been applied to µGC detection [26-27]. It consists of a hollow, vertical SiO_x cylinder (250-µm i.d.) with an expanded midsection. It is grown from a Si mold the top portion of which is subsequently etched away to leave the sensing region of the µOFRR cylinder extending above the surface of the etched Si substrate. The device also integrates on-chip fluidic-interconnection and fiber-optic probe alignment features. Resonant whispering gallery modes are generated in the cylinder wall by coupling to a tunable 1550-nm laser by means of a thinned optical fiber. Rapid, reversible shifts in resonant wavelength result from swelling and refractive index changes of a thin polymer film lining the cylinder due to vapor sorption and desorption [25]. Initial tests of a PDMS-coated µOFRR were described in Chapter 5. Those tests, performed with the µOFRR connected downstream from a single µGC column, showed remarkably fast responses and low detection limits under typical operating conditions. These results suggested that this device might have

sufficiently high sensitivity and sufficiently rapid response times to serve as the detector for µGC × µGC analyses.

Here, we report on initial performance characterization tests of a µGC × µGC separation module with this polymer-coated µOFRR sensor installed as the detector. Figure 6-1 shows a block After describing the methodology employed, results are presented from µGC × µGC separations of three VOC mixtures under isothermal conditions and with a modest temperature ramp applied to the separation module. The tradeoff between peak width and sensitivity attributable to the volatility of the analytes is highlighted, and it is shown for analytes with high volatility that peak widths are exceptionally narrow, ultimately limited by the injection bandwidth of the µTM. The prospects of using µOFRRs or µOFRR arrays in portable µGC × µGC instrumentation are assessed.

6.2 Experimental methods

6.2.1 Materials

All solvents and test compounds were >98% pure (Sigma-Aldrich, Milwaukee, WI) and used without further purification. The PDMS (OV-1) and poly(trifluoropropylmethyl)siloxane (PTFPMS, OV-215) polymers used as stationary phases and/or sensor coatings were obtained from Ohio Valley Specialty Chemicals (Marietta, OH).

6.2.2. Devices

The µTM mounting scheme, operation, and fabrication has been described previously [17-20]. Briefly, the Si chip (1.3 x 0.6 cm) contains a Pyrex-sealed deep-reactive-ion-etched (DRIE) Si µchannel (250 × 140 µm cross section) arranged in two thermally isolated convolved square-

spiral segments, 4.2 cm (upstream) and 2.8 cm (downstream) long, separated by a 1.0 mm long straight segment. Each stage, as well as each rim, has a Ti/Pt heater patterned on the Pyrex channel cap. RTDs are patterned in close proximity to the heaters to measure the temperature of each zone.

Fluidic connections to the µTM and upstream/downstream µcolumns was achieved through ~5-cm sections of deactivated fused silica capillary (250 µm i.d., upstream; 100 µm i.d., downstream) inserted into expansion ports on the chip and sealed with epoxy (Hysol 1C, Rocky Hill, CT). The device was then wire-bonded, heater side up, to a custom printed circuit board (PCB) with a hole cut out beneath the device for thermal isolation. Two Si spacers with integral air gaps were affixed to the µTM using photoresist (AZ9260, AZ Electronics Material, Luxembourg) in such a manner as to create a 19 µm air gap between the heaters of each stage and the top surface of the spacer. Two small slabs of Si were then attached to the top of these spacers using thermal grease. The entire assembly was mounted in close proximity to the TEC with thermal grease ensuring thermal contact between the Si spacers and the TEC. A plastic enclosure through which a stream of dry air is passed during operation is then secured around the µTM to prevent atmospheric water condensation on the device.

Each µcolumn consists of a DRIE-etched Si convolved square spiral channel with an anodically bonded Pyrex cap, the basic design and fabrication of which have also been described previously [28-30]. The ^{1}D separation stage assembled for this study consisted of two 3 m long, series-coupled, µcolumn chips (3.1 × 3.1 cm chip, 250 × 140 µm cross section) wall-coated with a PDMS stationary phase. The ^{2}D separation stage consisted of a single 0.5 m µcolumn chip (1.2 × 1.2 cm chip, 46 × 150 µm cross section) wall-coated with OV-215. Fluidic connections to the µTM were made through ~5-cm segments of fused silica capillary (250 µm i.d. for 3-m µcolumns,

100 μm i.d. for 0.5-m μcolumns) epoxied into expansion ports in the Si chips, and attached through fused silica press fit connectors.

The μOFRR structure and fabrication have been described in Chapters 4 and 5 as well as published work [24-25]. The resonator is a hollow SiOx cylinder with a 250 μm i.d. and 1.2 μm thick walls, partially released from a Si substrate diced into 2×2 cm chips. The resonator protrudes 80 μm from the annular trench etched into the Si substrate and has a 30 μm tall toroidal expansion region at the midsection. The cylinder creates a fluidic conduit through the Si substrate terminating on an aperture on the underside of the chip. Backside DRIE was used to create a tapered expansion port along the underside of the chip for capillary insertion, and a microfluidic channel connecting the capillary port and backside μOFRR aperture. A final front-side DRIE step created an optical-fiber alignment channel running laterally across the surface tangential to the μOFRR.

6.2.3 Stationary phase deposition

A PDMS stationary phase was deposited on the interior of the ^{1}D μcolumns and μTM using a static coating method published previously [28, 31]. 1% (w/w) dicumyl peroxide was added to the PDMS solution as a crosslinking agent. Calculated wall-coating thickness was 0.20 μm for the ^{1}D μcolumn and 0.30 μm for the μTM. The PDMS films in the μcolumn and μTM were cross-linked at 180 °C for 1h under N_2; the μcolumn was heated in an oven, the μTM was heated using the on-chip resistive heater to avoid rupturing the capillary-chip union. OV-215 was deposited on the interior of the ^{2}D μcolumn using static coating, calculated thickness was 0.08 μm.

To coat the interior wall of the μOFRR the resonator cavity was filled with a toluene solution of PDMS and the solvent was evaporated by placing the device in a vacuum chamber for 10 minutes. The PDMS film thickness was estimated from the solution concentration and the

interior volume of the cylinder to be approximately 0.3 μm assuming uniform deposition. The film was not cross-linked.

Following PDMS deposition, the backside fluidic channels were sealed with a 2×2 cm Pyrex coverplate using UV curable glue (NOA 81, Norland Optical, Cranbury, NJ). A short section of fused-silica capillary (250 μm i.d.) was then sealed into the completed device for external fluidic connection.

6.2.4 System integration

The two 3-m ^{1}D μcolumns were bonded to individual carrier PCBs with epoxy and connected in series by way of the attached capillaries using a press-fit union. The ^{2}D μcolumn was attached to a polyimide resistive heater pad (Omega Engineering, Inc., Stamford, CT) using thermal grease and polyimide tape. A wire thermocouple was inserted between the ^{2}D μcolumn and the heater pad to monitor temperature during operation.

The μTM was connected by the affixed capillaries between the ^{1}D and ^{2}D μcolumns using a press-fit union. The μGC × μGC subsystem was placed within the oven of a bench scale GC (Agilent 6890, Agilent Technologies, Palo Alto, CA). The temperature of the oven determined the temperature of the ^{1}D μcolumns as well as the ambient conditions of the TEC. The temperature of the ^{2}D μcolumn was controlled by the polyiminide heater pad, and was set at temperatures above that of the GC oven. The outlet capillary of the ^{2}D μcolumn extended outside the oven and connected to the μOFRR.

An optical fiber (SMF-28, Corning Inc., Corning, NY) was drawn over a hydrogen flame and a 1.4-cm segment was tapered down to an outer diameter of ~1 μm. The fiber was positioned in the on-chip alignment channel using a Vernier micrometer such that the thinnest part of the fiber contacted the expanded section of the μOFRR. The fiber was secured in place using a UV curable

adhesive applied on the far left and right sides of the chip. This assembly, as well as a photodiode (InGaAs Pin, Marktech optoelectronics, Latham, NY) and a fiber splice (fiberlok II, 3M, Saint Paul, MN), were mounted on a 3D-printed frame as depicted in Figure 6-2. One end of the optical fiber terminated at the photodiode while the other was inserted into the fiber splice for easy connection to the external laser.

The entire assembly was placed inside a small oven with a thermocouple and resitstive heater which was maintained at a temperature of 25 °C to thermostat the sensor temperature. The µOFRR input capillary was connected to the output of the ^{2}D column by a press-fit union. Optical input came from a 1550 nm fiber-coupled laser (CQF939/251, Philips, Amsterdam, NE); both the laser and the photodiode were connected to a DAQ card and controlled by custom-developed Labview software. Two separate µOFRRs were tested: one for the tests with the n-alkane mixture and a second identical device for the more complex VOC mixtures, after an optical fiber broke on the first device.

6.2.5 System testing

A test atmosphere of a mixture of C_7-C_{10} n-alkane vapors was generated in a 10-L FlexFilm® bag (SKC Inc., Eighty Four, PA) pre-filled with N_2 into which liquid samples of each mixture component were injected and allowed to evaporate. The injected volumes (40 µL for C_7 and C_8; 20 µL for C_9 and C_{10}) correspond to nominal vapor concentrations ranging of 250 to 660 parts-per-million (ppm) by volume. A test atmosphere was similarly generated for analyses run subsequently with a 7- and 11-component vapor mixture. The 7- component mixture contained 1,4, dioxane, 4-methyl-2-pentanone, toluene, n-octane, ethylbenzene, 3-heptanone, and n-nonane. Cyclopentanone, hexanal, m-xylene, and cumene were added to create the 11-component mixture that was tested. For these test atmospheres, 40 µL of each neat liquid was injected, except for

cyclopentanone, hexanal, and 3-heptanone, for which 80 µL was injected. The resulting concentrations ranged from 548 to 2210 ppm. Samples were drawn by a small diaphragm pump through a 112-µL sample loop via a 6-port valve maintained at 30 ℃, and then injected into the ^{1}D µcolumn through a 10-cm segment of capillary.

A modulation period, P_m, of 7 s was used for the n-alkane tests and a P_m 5 s was used for the analysis of the more complex mixtures. The µTM was operated similar to previous description [18, 20]; Temperature was modulated between T_{min} of -22 and -28°C for stage 1 and 2, respectively, and a T_{max} of 180°C, with a 500 ms offset between heating of the first and second stages. A custom Visual C# program was used to control the timing of the applied voltages and to read the temperature sensors via a DAQ card (NI USB-6212, National Instruments, Austin, TX). The laser was swept over a wavelength of 330 pm at a rates between 26 and 56 hertz, while the output of the photodiode was monitored. Resonant wavelength was defined as the wavelength at the output minimum and was calculated and recorded in real time by a peak finding algorithm in the Labview software. OriginPro 9.1 (OriginLab, Northampton, MA) and GC Image (Rev 2.2, Zoex, Houston, TX) were used for chromatographic data processing and display of 2-D chromatograms, respectively. The FID was operated at 250 °C and a data sampling rate of 200 Hz. Chromatographic data were collected by ChemStation software (Rev.B.01.01, Agilent Technologies, Santa Clara, CA).

6.3 Results and discussion

6.3.1 n-Alkane mixture separation

Initial tests entailed isothermal separations of C_7 through C_{10} with the ^{1}D µcolumns and µTM set at 30° C, the ^{2}D µcolumn at 50° C, the µOFRR at 25 °C, and the He carrier gas flow rate

at 1.5 mL/min. The raw $\mu GC \times \mu GC$ chromatogram is presented in Figure 6-3. The total elution time was ~25 min. In all cases, vapor exposure resulted in λ_{WGM} shifting to longer wavelengths, which indicates an increase in n_{eff} of the PDMS film. Since the difference between any of the n-alkane RI values (Table 6-1) and that of the PDMS (n = 1.404) is small, and two of the alkanes (i.e., C_7 and C_8) have RI values *lower* than that of PDMS, evidently film swelling dominates the net responses. This follows from the fact that the nominal initial PDMS film thickness of 300 nm is much less than the penetration depth of the evanescent field of the WGM extending from the interior wall of the $\mu OFRR$, given that the laser operates at 1550 nm. In this so-called "thin-film" regime [25, 32], any polymer swelling will increase the fraction of the probed interior volume occupied by the polymer. The observation of red shifts λ_{WGM} is consistent with previous reports on polymer-coated $(\mu)OFRR$ sensors [25-26]. All responses were reversible

The modulation number, M_N, i.e., the number of modulations per peak, is one variable used to adjust operating conditions of any $\mu GC \times \mu GC$ separation. It is a function of the width of the peak eluting from the ^1D μcolumn and the selected P_m value. Early eluting peaks are invariably narrower and hence usually have lower M_N values. For effective $\mu GC \times \mu GC$ it is generally recommended to adjust conditions to get M_N values of 3-4 for as many peaks as possible [33]. Higher M_N values provide diminishing returns, and temperature programming is typically used to decrease the retention time, and therefore the peak width, of mixture components eluting later in separation from the ^1D column.

The M_N values for the n-alkanes are listed in Table 6-1. As shown in Figures 6-3, the M_N increases from 2 to 6 (C_7 to C_{10}, respectively), which is similar to results reported earlier for this set of alkanes under similar conditions with FID used in place of the $\mu OFRR$. There is no evidence

of breakthrough, as the baseline is relatively stable and all modulated peaks return to baseline with little tailing.

Table 6-1 also presents the values of the full width at half maximum (FWHM) for the largest modulated peak for each alkane. This variable is primarily a function of the efficiency of remobilization from the µTM but can also be affected by retention on the ^{2}D µcolumn as well as the rates of sorption and desorption into and out of the PDMS interface film on the µOFRR. Since retention of alkanes on the polar OV-215 stationary phase of the ^{2}D column is minimal, the on-column band broadening contribution should be negligible. Both of the other factors will be affected by the vapor pressure of the analyte which, in turn, dictates the desorption rates from the PDMS films in the µTM and in the µOFRR. Figure 6-4 shows the inverse relationship between FWHM and p_v and although we cannot separate the contributions from the µTM and µOFRR to the net FWHM values, we note that the values here are significantly larger than those reported using an FID for a similar separation under nearly identical conditions [20].

The sensitivity of the µOFRR to each alkane was determined by dividing the total area under all modulated peaks (in pm·s) by the injected mass (in ng). The latter was taken as the product of the test atmosphere concentration and the sample loop volume and is considered approximate because it was not independently confirmed. Figure 6-4b plots the sensitivity of the µOFRR to each analyte against the corresponding PDMS partition coefficient, K, obtained from the literature [34]. The observed linear relationship ($R^2 = 0.988$) reflects the fact that K is ideally inversely proportional to p_v [35], and that alkane sorption into PDMS should approach ideal behavior in the absence of kinetic factors, such as slow desorption rates from the PDMS interface film for the less volatile compounds. To be precise, it is the sorbed volume (not mass) that dictates the swelling response in the µOFRR, which would warrant dividing the K values by the respective

densities of the alkanes, and account should also be taken of the alkane-PDMS RI value differences. But since the RI values and densities spanned by the alkanes are very small (Table 6-1), they would have a negligible effect on the correlation plotted in Figure 6-4b. The strength of this correlation provides presumptive evidence that even C_{10} diffusion out of the PDMS sensor interface film is rapid relative to the residence time of the peak in the sensing zone of the μOFRR.

Nonetheless, peak width and sensitivity both increase as the analyte vapor pressure decreases. Since the resolution between two peaks is inversely proportional to the average peak width, this explains the inherent tradeoff faced in trying to optimize peak-area sensitivity and resolution simultaneously. Of course peak-height sensitivity can increase significantly by thermal modulation but it is a little unreliable because small shifts in the timing of the modulation relative to the elution of the peak leads to large changes in peak height among the modulated peaks. In any case, with the μOFRR, as with other sensors employing sorptive interface films, sensitivity generally varies with K.

6.3.2 VOC Mixture separation

A mixture of seven VOCs from several different functional group classes was then analyzed. In this case the ^1D μcolumns and μTM were set at 50° C, the ^2D μcolumn at 80° C, the μOFRR at 25 °C, and the He carrier gas flow rate was increased to 2.5 mL/min. P_m was set as 5 s. The raw μGC × μGC chromatogram is presented in Figure 6-5. The total elution time was < 2 min. Once again vapor exposure resulted in λ_{WGM} shifting to longer wavelengths for all analytes. RI of tested analyes ranged from 1.394 (noctane) to 1.494 (m-xylene) [36], the same range spanned by the analytes tested in Chatper 5, and the observed red-shifts are consistent with the analysis presented there. All analytes were fully resolved, but the reduction in retention times accompanying operation at higher temperatures and a higher flow rate led to lower values of M_N.

For comparison, under these conditions n-C$_9$ eluted in 111 sec with M$_N$ = 2, whereas above it eluted in 549 sec with M$_N$ = 4. Figure 6-5a shows the raw chromatograms for sequential separations using first the µOFRR sensor and then a reference FID under identical conditions, plotted with injection times aligned. For the less volatile compounds (peaks 4-7) the FID captured multiple modulations, and the largest modulated peak is offset from the µOFRR peak by a single modulation period (5 s).

The FID is considered a 'zero dead volume' instrument, and the comparison is useful in identifying band broadening within the µOFRR. Figure 6-5b and 6-5c overlay the FID and µOFRR response profiles of the largest modulated peak of 2,4-methyl-2-pentanone (peak 2) and C$_9$ (peak 7). For the more volatile analyte (2,4-methyl-2-pentanone) the response profile of the µOFRR closely matches that of the FID: the µOFRR peak is just 5.1% broader (FWHM = 160 ms). For the less volatile C$_9$ the µOFRR peak is considerably broader (FWHM = 723 ms) while the reference FID profile is still narrow (FWHM = 195 ms). This data confirms that the increases in peak width seen in the initial experiment is a result of sorption kinetics into and out of the PDMS sensing layer within the µOFRR film, and is not a result of any upstream components. Unfortunately a comparison could not be made between the response profiles of the most volatile analyte (1,4-dioxane, peak 1) as the compound broke through the µTM cold-stage when recording with the FID, and we did not observe the expected modulated peak. The narrowest peak width for the µOFRR was observed for 1,4-dioxane (FWHM = 125 ms); no peak in the FID chromatogram had a lower FWHM, which suggests that this width is primarily limited by the injection bandwidth of the µTM, and not the time required to fill and purge the µOFRR volume. This indicates the µOFRR may be capable of resolving even narrower peaks for analytes of similar volatility given sharper injections.

The next analysis was performed with a lower flow rate (1.5 ml/minute) to increase retention time on the ^{2}D column and demonstrate separation along both dimensions. The lower flow rate increased separation between peaks and an additional 4 compounds were added to the mixture to take advantage of the increased peak capacity. Figure 6-6a shows the raw µGC × µGC chromatogram for the separation. All 11 components were well resolved and eluted in 165 seconds. Figure 6-6b shows the contour plot derived from the raw chromatogram, the plot shows separation of analytes along both retention indices. Polar VOCs such as 2,4-methyl-2-pentanone (peak 2), cyclopentane (peak 4), hexanal (peak 5), and 3-heptanone (peak 9) clearly separate along the second dimension, while nonpolar compounds such as the alkanes (C_8, peak 6; C_9 peak 10) separated only along the first dimension, and were not retained on the OV-215 coating of the ^{2}D column. This is the first successful demonstration of comprehensive µGC × µGC using a microsensor as the detector and a microfabricated modulator.

6.4 Conclusions

This study demonstrated an important advance in µGC × µGC technology, VOC separation and analysis using micro-fabricated modulator, columns and sensor. The inclusion of a microsensor facilitates future development of a fully integrated µGC × µGC analysis system by removing the need for lab-bench detectors and enabling rapid separations of complex mixtures with a miniaturized device. Several important factors affecting the operation and performance of such a microsystem were revealed such as the constraint placed on chromatographic resolution by sorption/desorption time into the microsensor interface film. Though experiments showed a low dead-volume sensor design and narrow bandwidth injection from the µTM can produce sharp peaks for volatile analytes, room temperature detection will yield broad peaks with decreasing

vapor pressure. Use of temperature controls should be pursued in future μGC x μGC work with any sorptive microsensor.

The integration of the μOFRR with embedded optical fiber waveguide and miniaturized ancillary components is a first, and a critical step in enabling optofluidic microsensors. Further efforts will focus on the development of μOFRR arrays, to provide sensor patterns for analyte identification, and improving the resilience of the packaged μOFRR detector assembly.

6.5 References

1 . W. R. Collin, G. Serrano, L. K. Wright, H. Chang, N. Nuñovero and E. T. Zellers, *Analytical Chemistry* **2013**, *86*, 655-663.

2 . R.-S. Jian, Y.-S. Huang, S.-L. Lai, L.-Y. Sung and C.-J. Lu, *Microchemical Journal* **2013**, *108*, 161-167.

3 . S. K. Kim, H. Chang and E. T. Zellers, *Analytical chemistry* **2011**, *83*, 7198-7206.

4 . P. R. Lewis, R. P. Manginell, D. R. Adkins, R. J. Kottenstette, D. R. Wheeler, S. S. Sokolowski, D. E. Trudell, J. E. Byrnes, M. Okandan and J. M. Bauer, *Sensors Journal, IEEE* **2006**, *6*, 784-795.

5 . J. Liu, N. K. Gupta, K. D. Wise, Y. B. Gianchandani and X. Fan, *Lab on a Chip* **2011**, *11*, 3487-3492.

6 . C.-J. Lu, W. H. Steinecker, W.-C. Tian, M. C. Oborny, J. M. Nichols, M. Agah, J. A. Potkay, H. K. Chan, J. Driscoll and R. D. Sacks, *Lab on a Chip* **2005**, *5*, 1123-1131.

7 . C.-J. Lu, J. Whiting, R. D. Sacks and E. T. Zellers, *Analytical chemistry* **2003**, *75*, 1400-1409.

8 . R. P. Manginell, J. M. Bauer, M. W. Moorman, L. J. Sanchez, J. M. Anderson, J. J. Whiting, D. A. Porter, D. Copic and K. E. Achyuthan, *Sensors* **2011**, *11*, 6517-6532.

9 . S. C. Terry, J. H. Jerman and J. B. Angell, *Electron Devices, IEEE Transactions on* **1979**, *26*, 1880-1886.

10 . Q. Zhong, W. H. Steinecker and E. T. Zellers, *Analyst* **2009**, *134*, 283-293.

11 . C. Jin and E. T. Zellers, *Analytical chemistry* **2008**, *80*, 7283-7293.

12 . M.-D. Hsieh and E. T. Zellers, *Analytical chemistry* **2004**, *76*, 1885-1895.

13 . T. Górecki, J. Harynuk and O. Panić, *Journal of separation science* **2004**, *27*, 359-379.

14 . J. Dallüge, J. Beens and U. A. T. Brinkman, *Journal of Chromatography A* **2003**, *1000*, 69-108.

15 . J. B. Phillips, R. B. Gaines, J. Blomberg, F. W. van der Wielen, J. M. Dimandja, V. Green, J. Granger, D. Patterson, L. Racovalis and H. J. de Geus, *Journal of High Resolution Chromatography* **1999**, *22*, 3-10.

16 . M. Libardoni, C. Fix, J. H. Waite and R. Sacks, *Analytical Methods* **2010**, *2*, 936-943.

17 .   S.-J. Kim, S. M. Reidy, B. P. Block, K. D. Wise, E. T. Zellers and K. Kurabayashi, *Lab on a Chip* **2010**, *10*, 1647-1654.

18 .   G. Serrano, D. Paul, S.-J. Kim, K. Kurabayashi and E. T. Zellers, *Analytical chemistry* **2012**, *84*, 6973-6980.

19 .   S.-J. Kim, G. Serrano, K. D. Wise, K. Kurabayashi and E. T. Zellers, *Analytical chemistry* **2011**, *83*, 5556-5562.

20 .   W. Collin, A. Bondy, D. Paul, K. Kurabayashi and E. T. Zellers, **2015**. *In Review*.

21 .   J. J. Whiting, C. S. Fix, J. M. Anderson, A. W. Staton, R. P. Manginell, D. R. Wheeler, E. B. Myers, M. L. Roukes and R. Simonson, *Solid-State Sensors, Actuators and Microsystems Conference, 2009. TRANSDUCERS 2009. International* **2009**, pp. 1666-1669.

22 .   J. Liu, M. K. Khaing Oo, K. Reddy, Y. B. Gianchandani, J. C. Schultz, H. M. Appel and X. Fan, *Analytical chemistry* **2012**, *84*, 4214-4220.

23 .   J. Liu, J. H. Seo, Y. Li, D. Chen, K. Kurabayashi and X. Fan, *Lab on a Chip* **2013**, *13*, 818-825.

24 .   K. Scholten, X. Fan and E. T. Zellers, *Applied physics letters* **2011**, *99*, 141108.

25 .   K. Scholten, X. Fan and E. T. Zellers, *Lab on a Chip* **2014**, *14*, 3873-3880.

26 .   Y. Sun, S. I. Shopova, G. Frye-Mason and X. Fan, *Optics letters* **2008**, *33*, 788-790.

27 .   S. I. Shopova, I. M. White, Y. Sun, H. Zhu, X. Fan, G. Frye-Mason, A. Thompson and S.-j. Ja, *Analytical Chemistry* **2008**, *80*, 2232-2238.

28 .   G. Serrano, S. M. Reidy and E. T. Zellers, *Sensors and Actuators B: Chemical* **2009**, *141*, 217-226.

29 .   M. Agah, J. A. Potkay, G. Lambertus, R. Sacks and K. D. Wise, *Microelectromechanical Systems, Journal of* **2005**, *14*, 1039-1050.

30 .   G. Lambertus, A. Elstro, K. Sensenig, J. Potkay, M. Agah, S. Scheuering, K. Wise, F. Dorman and R. Sacks, *Analytical chemistry* **2004**, *76*, 2629-2637.

31 .   S. Kendler, S. M. Reidy, G. R. Lambertus and R. D. Sacks, *Analytical chemistry* **2006**, *78*, 6765-6773.

32 .   A. M. Kummer, A. Hierlemann and H. Baltes, *Analytical chemistry* **2004**, *76*, 2470-2477.

33 .   J. Beens, H. Boelens, R. Tijssen and J. Blomberg, *Journal of High Resolution Chromatography* **1998**, *21*, 47-54.

34 .   P. A. Martos, A. Saraullo and J. Pawliszyn, *Analytical Chemistry* **1997**, *69*, 402-408.

35 .   A. Hierlemann, A. J. Ricco, K. Bodenhöfer, A. Dominik and W. Göpel, *Analytical Chemistry* **2000**, *72*, 3696-3708.

36 .   J. L. a. W. G. Mallard in *NIST Chemistry WebBook, NIST Standard Reference Database Number 69*, *Vol.* National Institute of Standards and Technology, Gaithersburg MD, 20899.

37 .   G. Baysinger in *CRC Handbook of Chemistry and Physics*, *Vol.* National Institute of Standards and Technology, **2014**.

Table 6-1 Physical properties and sensor response parameters for n-alkanes analytes[a]

VOC	RI[b]	ρ (g/ml)[b]	p_v (kPa)[c]	K_{PDMS}[d]	M_N[e]	FWHM (s)	Sensitivity (pm•s/(ng))
Heptane	1.386	0.680	6.01	564.9	2	0.34	0.032
Octane	1.394	0.699	1.73	1485	2	0.56	0.075
Nonane	1.406	0.718	0.459	3908	4	1.0	0.359
Decane	1.409	0.723	0.123	10280	6	2.0	0.813

[a] refractive index (RI), density (ρ), vapor pressure (p_v) and partition coefficient (K) values at 25 °C; [b] ref. 25; [c] ref. 26; [d] ref. 27; [e] The criterior applied to the small modulatoed peaks is that their height must exceed 3 times the standard deviation of the baseline signal (0.42 pm).
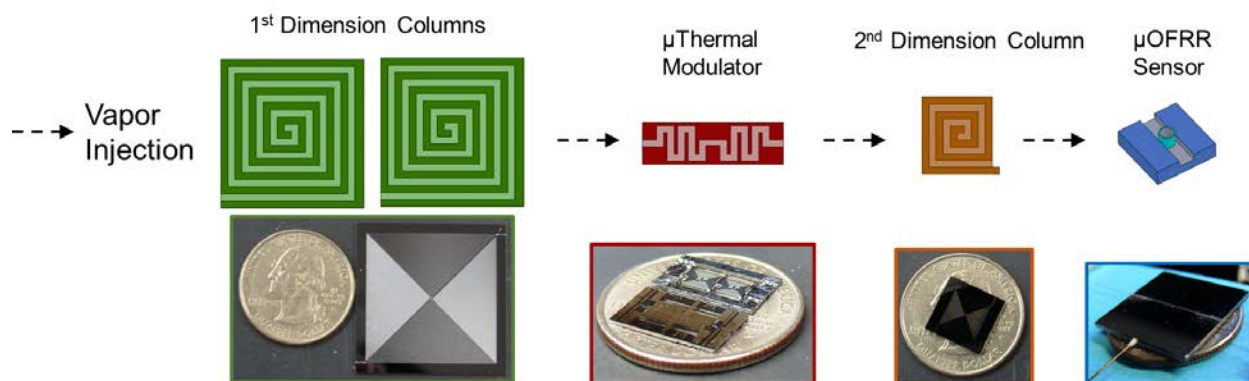
Figure 6-1. Illustration depicting the four separate components of the μGC × μGC system and their operation.
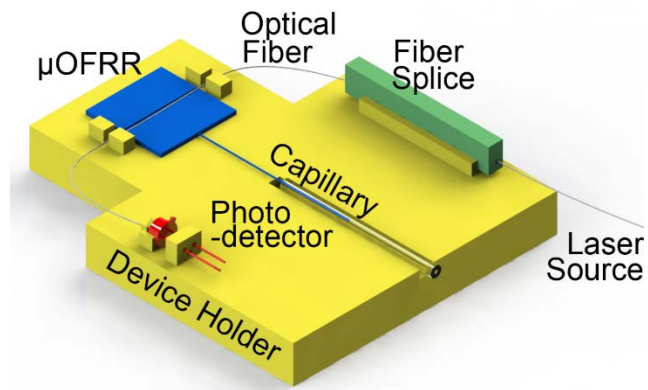
Figure 6-2. Diagram of the μOFRR sensor, photodetector and fiber splice mounted on a 3D printed frame.
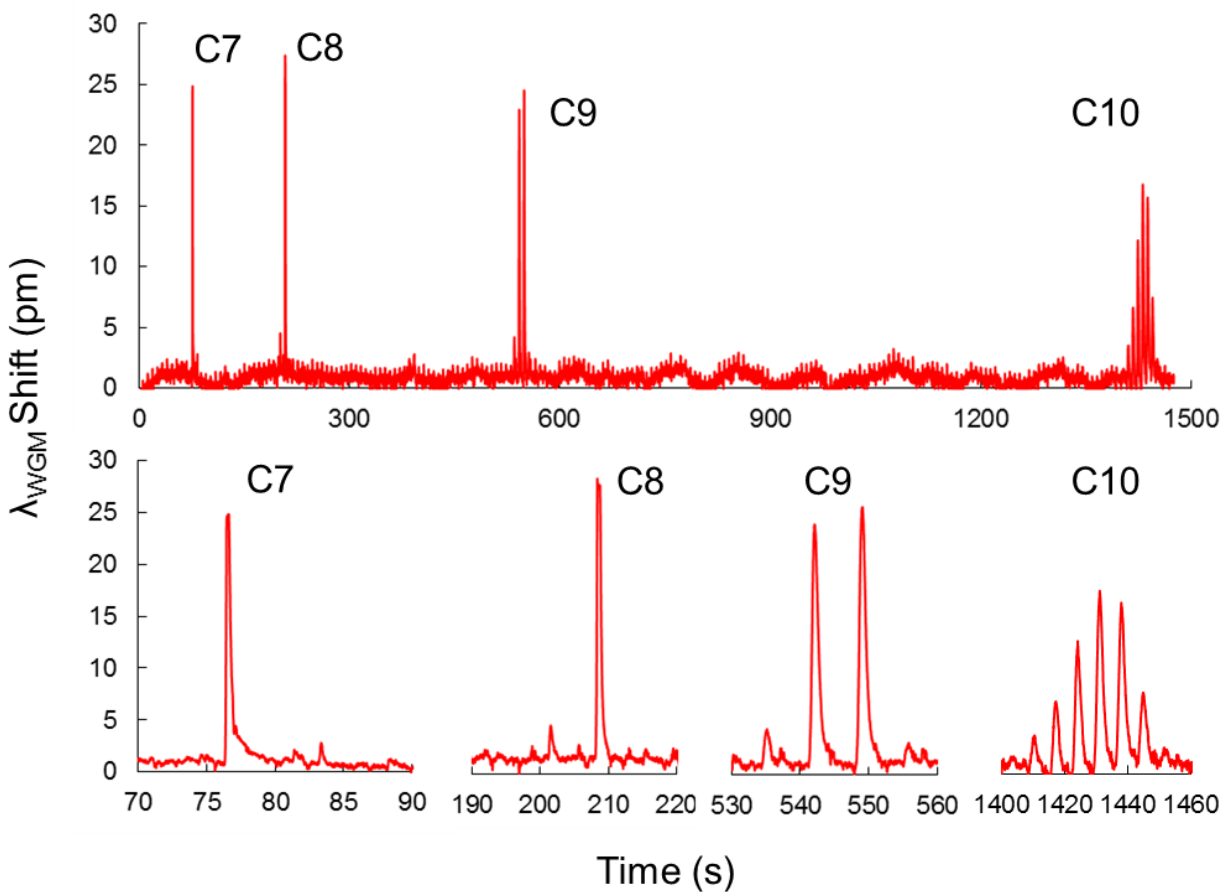
Figure 6-3. Raw µGC × µGC chromatogram showing isothermal separation of C_7-C_{10} using a µOFRR sensor as the output detector. Close up view of each analyte shown below (below).
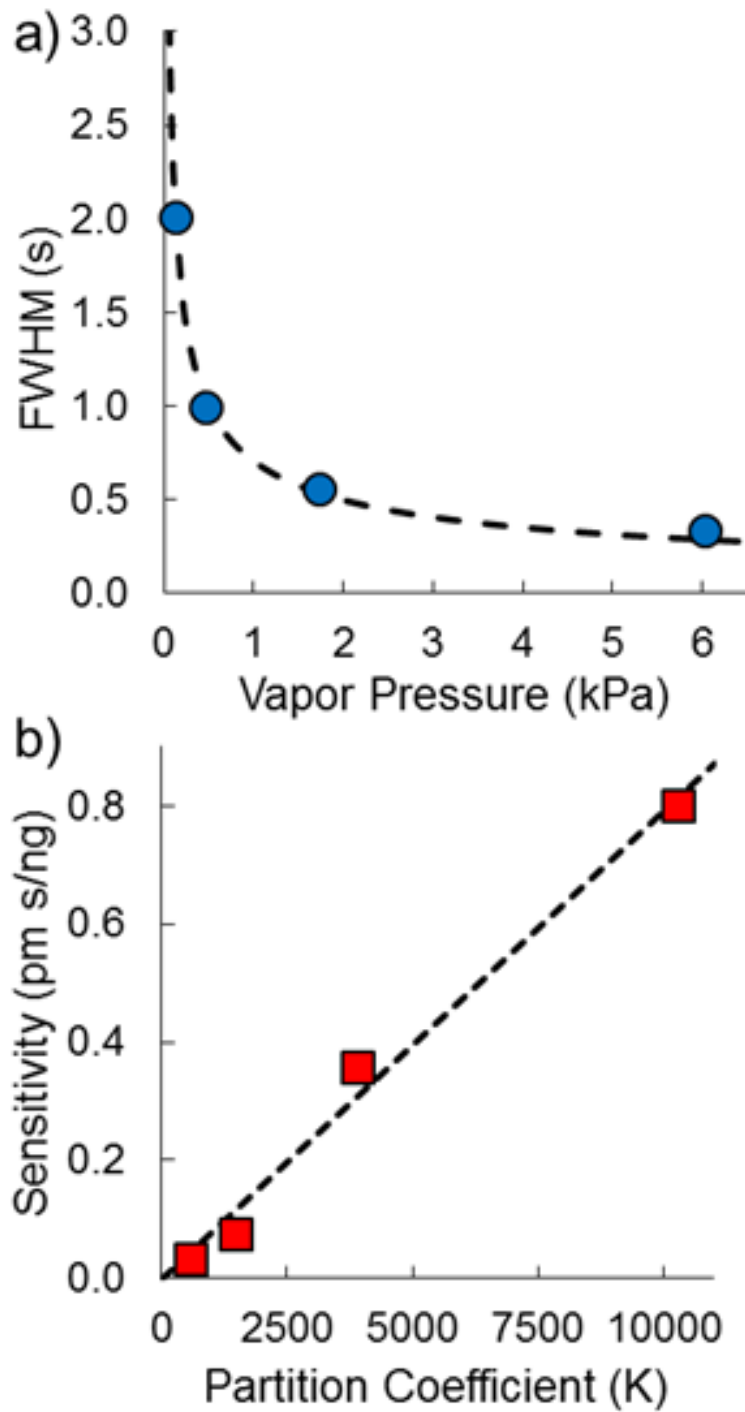
Figure 6-4. (a) Plot of full width at half maximum of the largest modulated peak in C_7-C_{10} separation versus analyte vapor pressure. (b) Plot of μOFRR sensitivity in peak area over injected mass versus partition coefficient in PDMS.
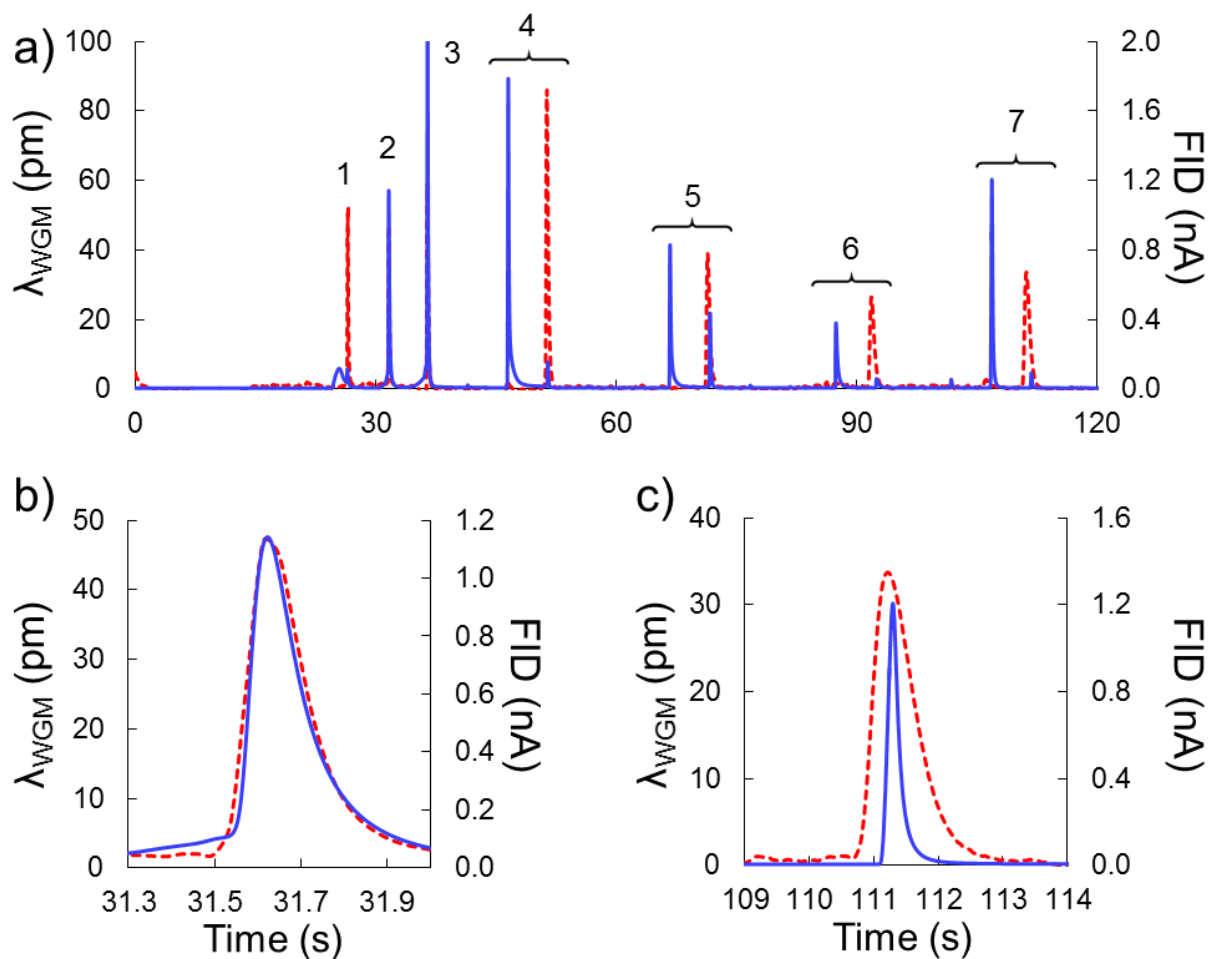
Figure 6-5. (a) Raw µGC × µGC chromatogram of 7-component VOC mixture. µOFRR (dotted line) and FID (solid line) used as detector in serial runs under identical conditions. Conditions: ^{1}D µcolumn 6 m, PDMS (0.20 µm thickness), 50 °C; ^{2}D µcolumn 0.50 m, OV-215 (0.08 µm thickness) 80 °C (oven); F = 2.5 mL/min. Compounds: 1,4, dioxane; 2, 4-methyl-2-pentanone; 3, toluene; 4, octane; 5, ethylbenzene; 6, 3-heptanone, 7, nonane; (b) Response profile for 2,4-methyl-2-pentanone (peak 2); (c) Response profile for the largest modulation of nonane (peak 7), with the FID peak shifted to be coincident with the µOFRR peak.
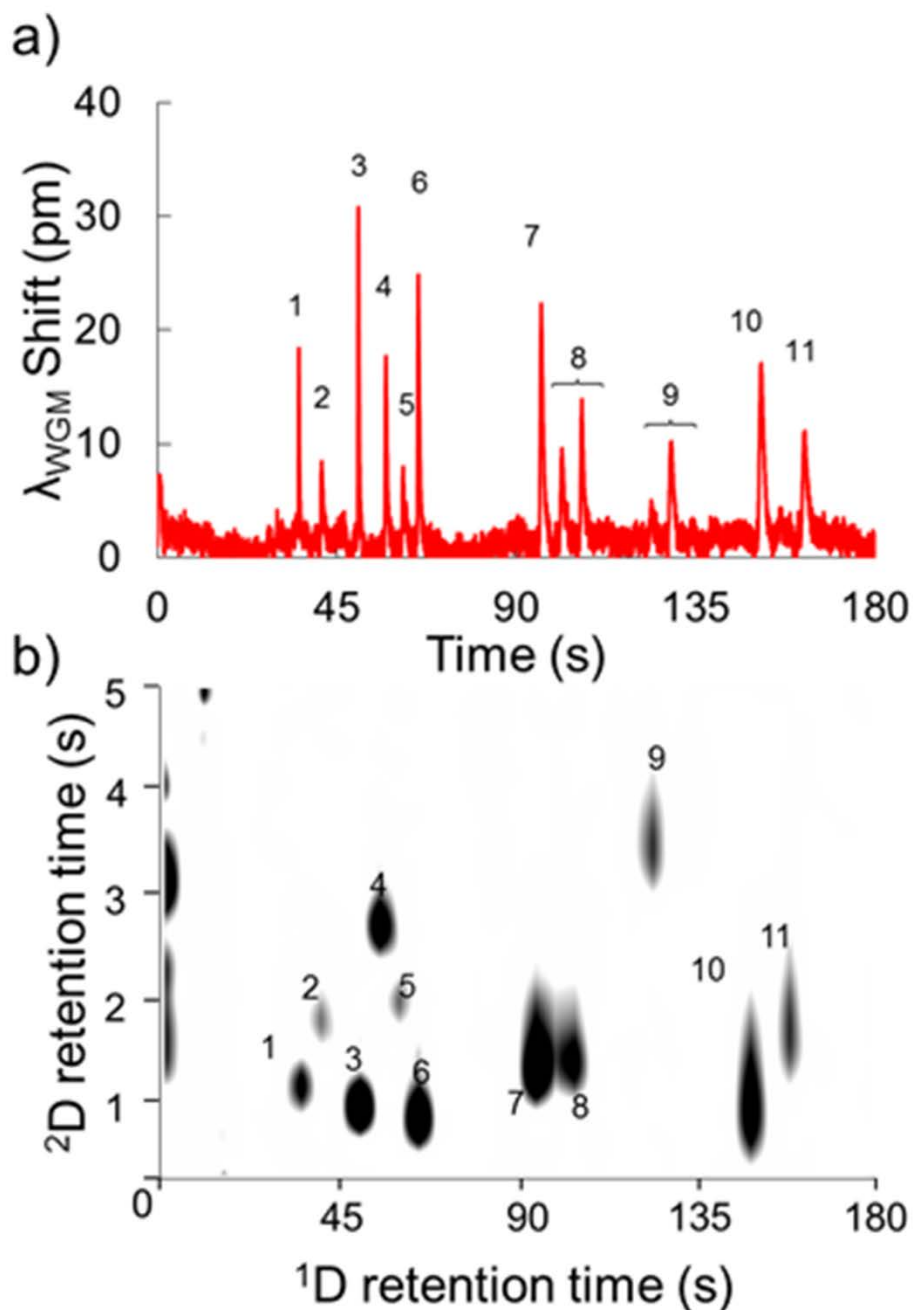
Figure 6-6. (a) Raw µGC × µGC chromatogram of 11-component VOC mixture with detector. Conditions: ^{1}D µcolumn 6 m, PDMS (0.20 µm thickness), 50 °C; ^{2}D µcolumn 0.50 m, OV-215 (0.08 µm thickness) 80 °C (oven); F = 1.5 mL/min. Compounds: 1,4, dioxane; 2, 4-methyl-2-pentanone; 3, toluene; 4, cyclopentanone; 5, hexanal; 6, octane; 7, ethylbenzene; 8, m-xylene; 9, 3-heptanone; 10, nonane; 11, cumene; (b) Contour plot of the same chromatogram showing separation of 11-component mixture along two dimensions.

Chapter VII

Vapor Discrimination by Laser Reflectance Sensing of a Single Functionalized Nanoparticle Film

7-1. Introduction

Optical sensing of biological and chemical analytes by means of devices and/or materials with engineered nanoscale features has been studied extensively [1-2]. In regard to the measurement of airborne volatile organic compounds (VOC), sensing on the basis of absorbance, reflectance, or Raman scattering has been implemented using metallic [3-4], organometallic [5-7], and polymeric nanoparticles [8], as well as photonic crystals [9] and lamellar gratings or reflectors [10]. The utility of localized surface plasmon resonances (LSPR) in liquid-phase (bio)chemical analyses has been recognized for some time [2, 11-12], but has only recently been applied to VOC detection.

By use of unmodified grating structures [10] or surface-patterned metal nano-islands with either polymer overlay films [3] or thiolate-monolayer functionalization [13], it has been shown that LSPR spectral shifts differ among VOCs on the basis of differential changes in the refractive index (RI) of the interstitial matrix accompanying vapor sorption. For example, Potyrailo *et al*. measured visible reflectance changes due to vapor exposure in unmodified naturally occurring lamellar gratings (i.e., Morpho butterfly wings), and extracted responses at four selected wavelengths to discriminate among high concentrations of methanol, ethanol and water vapor, and

among the three isomers of dichloroethylene [10]. Karakouz *et al*. reported on polymer-coated gold nano-islands, showing differences in the magnitude of LSPR maxima (λ_{max}) shifts with polar and non-polar polymers according to vapor affinity [3], and Chen et al. used thiolate-monolayer functionalized gold nano-islands to detect terpene vapors [13].

Others have used films of discrete thiolate-monolayer-protected gold nanoparticles (MPN) as plasmonic interface materials [5-7], complementing the well-documented use of MPNs as vapor-sorptive layers on chemiresistors (CR) and thickness shear mode resonators (TSMR) [14-20]. For example, Lu *et al*. used monolayer films of various metal MPNs to detect several VOCs by measuring changes in total absorbance or shifts in λ_{max} [5]. In their subsequent study of functionalized Ag, Au, and Au core-shell MPN films, they showed that sorption-induced changes in absorbance in the vicinity of λ_{max} among several films could be used for VOC discrimination [6]. More recently, Dalfovo et al. attributed observed differences in the shifts of the LSPR λ_{max} of tetraoctylammonium bromide (TOAB) functionalized MPN films upon exposure to saturated headspace concentrations of toluene and ethanol to differences in film swelling/shrinkage and RI changes by the two VOCs [7].

The results of these studies suggest that discriminating among VOCs by use of a single MPN-coated optical sensor should be possible, and that it could be achieved by probing the MPN film at as few as two wavelengths. Here, we describe such a device and present preliminary results demonstrating such capabilities. The visible absorbance spectra of an *n*-octanethiolate (C8) MPN film before, during, and after exposure to vapors of toluene and n-heptane are presented first to characterize the nature of the spectral changes and to confirm reversibility of the vapor-film interaction. Then laser reflectance measurements at two discrete wavelengths are presented, demonstrating the discrimination of the two VOCs on the basis of the ratios of responses at these

wavelengths. The relative importance of changes in the film RI and film swelling to the differential responses at different wavelengths are discussed as well as methods by which diversity of responses might be further enhanced.

7.2 Experimental methods

7.2.1. Materials

C8-MPNs were synthesized according to the method of Rowe *et al*. [14], with an average Au core diameter of 4.3 ± 0.9 nm. Polydimethylsiloxane (PDMS, Fluka, St. Louis, MO) was used as a reference material. Toluene and *n*-heptane (99%, Sigma Aldrich, St. Louis, MO) were used as received. The values of RI, density, and vapor pressure for these two test vapors are as follows [21]: toluene, 1.496, 0.867 g/mL, and 2.91 kPa (20º C); *n*-heptane, 1.387, 0.684 g/mL, and 4.63 kPa (20º C). The RI of the octanethiol monolayer was assumed to be the RI of 1-octanethiol, 1.45 [21].

A glass slide was diced manually to dimensions of 45×10 mm to fit inside a 3-mL plastic cuvette, and 8×8 mm chips of <100> Si were diced from a 4-inch wafer with a dicing saw. Substrates were cleaned sequentially in acetone and isopropanol while immersed in an ultrasonic bath, blown dry, and then exposed to vapors of hexamethyldisilazane (HMDS) to promote adhesion of the C8-MPN or PDMS films. Films were deposited from dilute (5 mg/ml) solutions of C8-MPNs in toluene by spray coating with an airbrush ~30 cm from the substrate using with air at approximately 140 kPa as the propellant. Thickness and uniformity were assessed by optical microscopy and laser interferometry (LEXT, Olympus, Tokyo, Japan). PDMS was spin-coated at 7600 rpm onto a Si chip from a toluene solution (5 mg/mL). The thickness was estimated to be 1-1.2 µm.

7.2.2. Transmission spectroscopy

The MPN-coated glass slide was placed vertically in the plastic cuvette and the visible absorbance spectrum was measured (DU800 UV-Vis spectrophotometer Beckman Coulter, Brea, CA). The effects of vapor exposure were assessed initially by placing ~1.5 µL of liquid VOC in the lid of the cuvette and quickly capping it so that the film was exposed to a high concentration of the vapor. The spectrum was collected and then the lid was removed to allow the vapor to dissipate for 20 min prior to collecting another spectrum. A blank spectrum was collected with an uncoated slide similarly in a sealed cuvette. Separate exposures to toluene and n-heptane were performed in duplicate. Replicate spectra were superimposable.

7.2.3. Reflectance sensor

A microfluidic enclosure, 1 mm deep and 0.85 mm wide, was formed from three glass slides using UV-curable glue and sealed to the underlying MPN-coated Si chip with adhesive. An identical microfluidic enclosure was affixed to the PDMS coated Si chip. The ensemble was mounted to an adjustable metal stage with double sided tape. The upstream end of a 5-m-long, fused silica capillary (250-µm i.d., Restek, Bellefonte, PA) was attached to the injection port of a benchscale gas chromatograph (3800, Varian, inc., Palo Alto, CA) and the downstream end was inserted into the inlet of the microfluidic enclosure and sealed. Helium was used as the carrier gas at 8 ml/min.

Figure 7-1 depicts the measurement configuration. The coated Si chip was illuminated sequentially by a 785-nm tunable diode laser and a 488-nm diode pumped solid state laser, and the intensity of the reflected beam was measured by a CMOS detector (Thor Labs DCC1240M, Newton, NJ) with an acquisition time of 1-4 µs and a save rate of 20 frames/s. The 783-nm laser had a 0.8 mW output while the 488 nm laser had a 10.8 mW output filtered down to 0.15 mW.

These wavelengths were selected because they bracket λ_{max} for the C8-MPN film. A 30º angle of incidence was found to give the largest responses, and was fixed for all experiments. Reflected intensity at each wavelength was recorded during separate dynamic exposures to toluene and *n*-heptane over a five-fold range of concentration by injecting 40, 80, 150 and 200 µL (corresponding to 4.3-22 µg of toluene and 8.6-43 µg of n-heptane) of headspace above the liquid solvents by gas-tight syringe into the GC injection port at 250º C. Injected mass was calculated assuming saturation of the headspace at 20 °C. Due to higher sensitivity of the PDMS film, calibrations were performed with a 10,000:1 injection split. Measurements were taken at each wavelength sequentially, with 4-5 replicates collected at each exposure level.

Data were analyzed using Origin software (v. 8.5.1, OriginLab, Northampton, MA). A 20-point fast Fourier transform algorithm was used to smooth the data. Sensor response was defined as the integrated peak area (detector counts × seconds) averaged across all replicates. A set of calibration curves plotting sensor response as a function of injection mass was generated, and the sensitivity was defined as the slope of the resulting line as determined by least-squares regression with forced zero.

7.3 Results and discussions

7.3.1. Absorbance spectra

Spray-coated C8-MPN films appeared homogeneous by visual inspection but microscopically were shown to comprise dense, multilayer coated sections surrounded by areas of uncoated substrate (Figure 7-2a). Laser interferometry at five locations (each 130 × 130 µm) of one representative film indicated an average film thickness (coated regions) of 260 nm with a standard deviation (SD) of 90 nm. The visible absorbance spectrum in Figure 7-2b shows a broad

LSPR peak with λ_{max} at 536.0 nm. The spectrum of C8 MPNs of similar Au-core size in toluene solution was reported to give a λ_{max} of 517 nm [14]. The red shift in λ_{max} and broadness of the absorbance of the airbrushed film reflects the expected increase in optical coupling between the Au cores associated with the smaller inter-particle spacing [22].

Blue shifts in λ_{max} to 530.6 nm and 533.4 nm were observed during separate, static exposures of a C8-MPN film to near-saturated concentrations of toluene and *n*-heptane vapors, respectively. In general, shifts in λ_{max} can arise from two separate phenomena: an increase in the inter-particle distance due to film swelling and a change in the RI of the medium surrounding the nanoparticles [22]. The former will cause a blue shift in λ_{max} and the effect of the latter will depend on the RI difference between the inter-particle matrix of the MPN film and the sorbed vapor; if the RI of the sorbed vapor is higher than that of the organic matrix, then a red shift is expected, and if it is lower, then a blue shift is expected. The blue shift in λ_{max} for *n*-heptane is consistent with its RI being lower than that of the C8 monolayer (bulk value) and its ability to swell the film. The blue shift in λ_{max} for toluene, the RI of which is slightly higher than that of C8, indicates that swelling dominates the optical response. A similar result (and explanation) was reported by Dalfovo *et al*. for 4.4-nm TOAB-MPN films exposed to saturated toluene vapor [7], in spite of the RI for TOAB (i.e., n = 1.42) being lower than that of toluene. The larger shift in λ_{max} for toluene, compared to *n*-heptane, observed here can be attributable to its larger partition coefficient and swelling efficiency (see below) [19]. Although λ_{max} returned to its pre-exposure value upon subsequent venting of the cuvette with room air in the experiments above, we have also observed that extended exposure to saturated concentrations of toluene led to a persistent loss of the LSPR absorbance, which was recovered only after re-casting the same film from liquid toluene (see Appendix III).

In addition to shifts in λ_{max}, absorbance changes within selected spectral regions occurred that differed between the two VOCs: for all $\lambda > \lambda_{max}$ exposure to either VOC reduced the magnitude of the absorbance, while for all $\lambda < \lambda_{max}$ toluene increased the absorbance and *n*-heptane decreased the absorbance. This analyte-dependent difference in sorption-induced changes in spectral features implies that selective sensing would be possible by probing the MPN film at multiple discrete wavelengths.

7.3.2. Reflectance measurements

Toward that end, a C8-MPN film was coated on a clean Si substrate, enclosed in a glass microfluidic cell, and exposed to discrete injections of each VOC over a range of vapor concentrations while laser reflectance measurements were collected at 488 and 785 nm. At both wavelengths and for both analytes, the reflected intensity decreased with increasing injected analyte mass. Figures 7-3a and b show the calibration curves for both vapors after converting transmittance to (effective) absorbance, which fit a linear model well ($r^2 > 0.97$, standard errors of the slopes $< 6\%$) (note: what we refer to as absorbance here is, in fact, a combination of absorbance, reflectance, and scattering). Calculated sensitivities (absorbance peak area per µg of injected vapor) at 785 nm are 9.5×10^{-3} and 3.2×10^{-3} for toluene and *n*-heptane, respectively, and at 488 nm are 14×10^{-3} and 4.0×10^{-3}, respectively. The representative response profiles shown in the inset of Figure 7-3a document the reversibility and repeatability of the responses.

The relative magnitudes of the sensitivities can be assessed in light of a previous study by Steinecker *et al.* of vapor uptake by films C8-MPNs with ~4.3-nm Au-core diameters on CR and TSMR sensors [23]. Partition coefficients (K_{voc}) and fractional film swelling efficiencies (Ψ_{voc}) for both toluene and *n*-heptane in C8-MPN films were derived from their data. Values of $K_{tol} = 1000$

and K_{hep} = 410 were reported along with values of Ψ_{tol} = 0.32 and Ψ_{hep} =0.23. From these values we calculate a net swelling ratio of 3.4 (i.e., $K_{tol}/K_{hep} \times \Psi_{tol}/\Psi_{hep}$).

Since the dynamic exposures in this study were conducted under the same conditions for both VOCs, producing similar peak widths, the vapor concentrations should be similar for a given injected mass. The toluene:n-heptane sensitivity ratios are 2.97 and 3.60 at 785 nm and 488 nm, respectively, which are remarkably close to the swelling ratio of 3.4. This suggests that the relative responses are dictated primarily by the relative volumetric changes of the film. That the sensitivity ratio at 488 nm is somewhat larger, and the sensitivity ratio at 785 nm is somewhat smaller, than the calculated swelling ratio is qualitatively consistent with the differences in absorbance between toluene and n-heptane noted above for the spectral regions flanking λ_{max}. Such wavelength-dependent differences reflect the contributions of the RI changes to the optical responses.

In the reflectance measurements, the toluene sensitivity was higher at 488 nm than at 785 nm, which is consistent with the transmittance data that showed an increase in absorbance at $\lambda <$ λ_{max}. But, whereas the reflectance measurements showed *increases* in absorbance at the longer wavelength for toluene and at both wavelengths for n-heptane, the transmittance measurements showed absorbance *decreases* for these exposures. This discordance can be ascribed to differences in these two optical configurations; specifically to an increase in the extent of scattered and reflected light from the air-film and substrate-film interfaces in the reflectance measurements [24-25].

Limits of detection (LOD) were calculated as 3σ/(sensitivity) where σ was the standard deviation of the baseline signal and the sensitivity was re-calculated using peak height instead of area. LODs at 785 nm are 0.20 and 0.49 µg for toluene and heptane, respectively, and at 488 nm are 1.1 and 3.3 µg, respectively. The LODs are higher at 488 nm, despite the higher sensitivities

at this wavelength, because of the increased noise from the 488-nm laser; the baseline noise at 785 nm was eight times lower than at 488 nm. No effort was made to optimize the set-up for sensitivity.

Measurements were also collected in the same manner with a reference Si substrate coated with PDMS. Since PDMS has no absorbance in the visible range, changes in reflected light intensity arise only from changes in the film thickness. This phenomenon is exploited in vapor sensors that are based on Fabry-Perot interferometry [26]. Responses were proportional to injected vapor mass and calibration curves were linear ($r^2 > 0.97$, standard slope error $< 5\%$). Since the PDMS exposures were performed with split injections from the GC and the PDMS film was ~4-5 times thicker than the MPN film, a direct comparison of sensitivities and LODs is not possible. However, it can be stated that the PDMS film showed much higher sensitivities than did the MPN film, with LODs in the sub-ng range for both VOCs, consistent with previous reports of similarly configured PDMS-coated optical sensors [26].

The bar charts in Figure 7-3c present the ratios of the sensitivities at the two wavelengths for toluene and *n*-heptane for both films, normalized to that at 488 nm, which gave the highest sensitivity in all cases. For the C8-MPN film the average ($\pm$ SD) ratios are 0.68 ± 0.035 and 0.80 ± 0.053 for toluene and *n*-heptane. The corresponding ratios for the PDMS reference film are 0.082 ± 0.005 and 0.088 ± 0.006. The difference between the MPN ratios is statistically significant ($p < 0.05$), whereas the difference between the PDMS ratios is not ($p > 0.20$), confirming that vapor discrimination is a function of the optical properties of the MPN film.

7.4 Conclusions

In conclusion, we have shown that dual-wavelength optical reflectance sensing of a single MPN film exhibiting LSPR affords quantitative and qualitative information about airborne VOCs. In this proof-of-concept study, the discrimination of two non-polar VOCs on the basis of wavelength-specific differences in reflected light intensity was demonstrated with a simple platform comprising a microfluidic cell, two laser sources, and a photodetector. Miniaturization into a compact portable system would be relatively straightforward.

Reversible blue shifts in the LSPR λ_{max} were observed for high-concentration exposures to both toluene and *n*-heptane, despite their RI values flanking that of the C8 monolayers in the MPNs tested here. These results, coupled with estimates of swelling ratios derived from independent data, suggest that responses are determined primarily by increases in the average inter-particle distance of the MPNs accompanying sorption-induced film swelling, and secondarily by changes in the local RI. In contrast, LSPR sensing approaches that employ immobilized gold nano-islands are only sensitive to shifts in the local RI of the surrounding medium [3, 14].

The use of multiple, discrete, optical probes of individual plasmonic sensing films shown here is an example of what might be termed multi-variable (MV) sensing. Other examples have been reported by Potyrailo, *et al.* [10, 27]. Creating an array of such MV sensors in which multiple films of MPNs with different core sizes, shapes, and/or monolayer structures are probed at two or more wavelengths shows promise for increasing the diversity of responses one can obtain from a VOC sensor array. This, in turn, should lead to improvements in performance over current single-transducer (ST) and multi-transducer (MT) arrays, which provide only a single response from each sensor in the array and, consequently, have only limited capabilities for VOC-mixture analysis [28-29].

Although the sensitivity achieved with the C8-MPN sensing film here was quite low, enhanced sensitivity should be possible by use of high-quality-factor optical resonators, in which optical signals are amplified by photon recirculation [30]. A parallel effort in our laboratory on the development of microfabricated optofluidic ring resonators (μOFRR) as platforms for multi-wavelength sensing with MPN interface films has shown some promising results in preliminary testing [31-32].

7.5 References

1 .   A. N. Shipway, E. Katz and I. Willner, *ChemPhysChem* **2000**, *1*, 18-52.
2 .   M. E. Stewart, C. R. Anderton, L. B. Thompson, J. Maria, S. K. Gray, J. A. Rogers and R. G. Nuzzo, *Chemical reviews* **2008**, *108*, 494-521.
3 .   T. Karakouz, A. Vaskevich and I. Rubinstein, *The Journal of Physical Chemistry B* **2008**, *112*, 14530-14538.
4 .   M. K. K. Oo, C.-F. Chang, Y. Sun and X. Fan, *Analyst* **2011**, *136*, 2811-2817.
5 .   C.-S. Cheng, Y.-Q. Chen and C.-J. Lu, *Talanta* **2007**, *73*, 358-365.
6 .   K.-J. Chen and C.-J. Lu, *Talanta* **2010**, *81*, 1670-1675.
7 .   M. C. Dalfovo, R. C. Salvarezza and F. J. Ibañez, *Analytical chemistry* **2012**, *84*, 4886-4892.
8 .   T. Endo, Y. Yanagida and T. Hatsuzawa, *Sensors and Actuators B: Chemical* **2007**, *125*, 589-595.
9 .   T. L. Kelly, A. Garcia Sega and M. J. Sailor, *Nano letters* **2011**, *11*, 3169-3173.
10 .   R. A. Potyrailo, H. Ghiradella, A. Vertiatchikh, K. Dovidenko, J. R. Cournoyer and E. Olson, *Nature Photonics* **2007**, *1*, 123-128.
11 .   N. Nath and A. Chilkoti, *Analytical Chemistry* **2002**, *74*, 504-509.
12 .   A. Kabashin, P. Evans, S. Pastkovsky, W. Hendren, G. Wurtz, R. Atkinson, R. Pollard, V. Podolskiy and A. Zayats, *Nature materials* **2009**, *8*, 867-871.
13 .   B. Chen, C. Liu and K. Hayashi, **2014**.
14 .   M. P. Rowe, K. E. Plass, K. Kim, C. Kurdak, E. T. Zellers and A. J. Matzger, *Chemistry of materials* **2004**, *16*, 3513-3517.
15 .   F. I. Bohrer, E. Covington, C. a. Kurdak and E. T. Zellers, *Analytical chemistry* **2011**, *83*, 3687-3695.
16 .   C.-L. Li, Y.-F. Chen, M.-H. Liu and C.-J. Lu, *Sensors and Actuators B: Chemical* **2012**, *169*, 349-359.
17 .   J. W. Grate, D. A. Nelson and R. Skaggs, *Analytical chemistry* **2003**, *75*, 1868-1879.
18 .   N. Krasteva, I. Besnard, B. Guse, R. E. Bauer, K. Müllen, A. Yasuda and T. Vossmeyer, *Nano Letters* **2002**, *2*, 551-555.
19 .   L. Wang, L. Wang, X. Shi, N. N. Kariuki, M. Schadt, G. R. Wang, Q. Rendeng, J. Choi, J. Luo and S. Lu, *Journal of the American Chemical Society* **2007**, *129*, 2161-2170.

20 .   S. K. Kim, H. Chang and E. T. Zellers, *Analytical chemistry* **2011**, *83*, 7198-7206.
21 .   G. Baysinger in *CRC Handbook of Chemistry and Physics*, *Vol.* National Institute of Standards and Technology, **2014**.
22 .   A. C. Templeton, J. J. Pietron, R. W. Murray and P. Mulvaney, *The Journal of Physical Chemistry B* **2000**, *104*, 564-570.
23 .   W. H. Steinecker, M. P. Rowe and E. T. Zellers, *Analytical chemistry* **2007**, *79*, 4977-4986.
24 .   G. Gauglitz, A. Brecht, G. Kraus and W. Mahm, *Sensors and Actuators B: Chemical* **1993**, *11*, 21-27.
25 .   G. Daaboul, R. Vedula, S. Ahn, C. Lopez, A. Reddington, E. Ozkumur and M. Ünlü, *Biosensors and Bioelectronics* **2011**, *26*, 2221-2227.
26 .   K. Reddy, Y. Guo, J. Liu, W. Lee, M. K. Khaing Oo and X. Fan, *Sensors and Actuators B: Chemical* **2011**, *159*, 60-65.
27 .   R. A. Potyrailo and W. G. Morris, *Analytical chemistry* **2007**, *79*, 45-51.
28 .   C. Jin, P. Kurzawski, A. Hierlemann and E. T. Zellers, *Analytical chemistry* **2008**, *80*, 227-236.
29 .   C. Jin and E. T. Zellers, *Analytical chemistry* **2008**, *80*, 7283-7293.
30 .   F. Vollmer and S. Arnold, *Nature methods* **2008**, *5*, 591-596.
31 .   K. Scholten, X. Fan and E. T. Zellers, *Applied physics letters* **2011**, *99*, 141108.
32 .   K. Scholten, K. Reddy, X. Fan and E. Zellers, *Solid-State Sensors, Actuators and Microsystems (TRANSDUCERS & EUROSENSORS XXVII), 2013 Transducers & Eurosensors XXVII: The 17th International Conference on* **2013**, pp. 850-853.
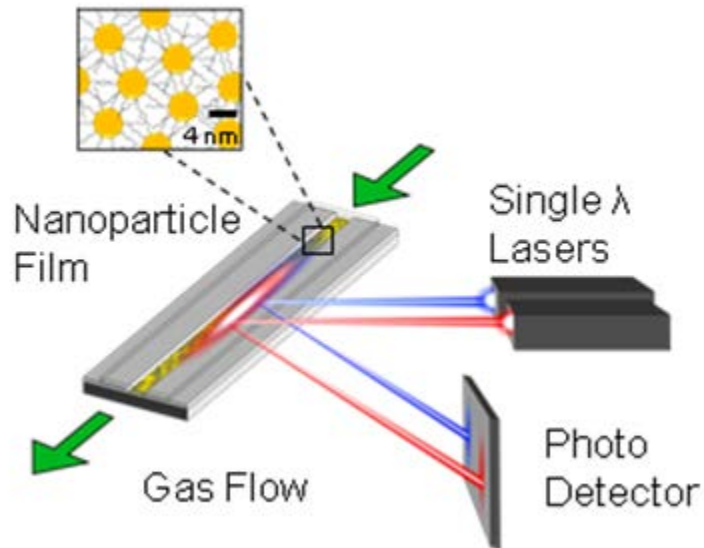
Figure 7-1. Illustration of the apparatus used for laser reflectance measurements of C8-MPN and PDMS films during calibrations with toluene and *n*-heptane. Discrete injections of different quantities of each vapor were made via a heated GC injection port and were routed through the microfluidic cell via de-activated capillary at 8 mL/min (carrier gas was He).
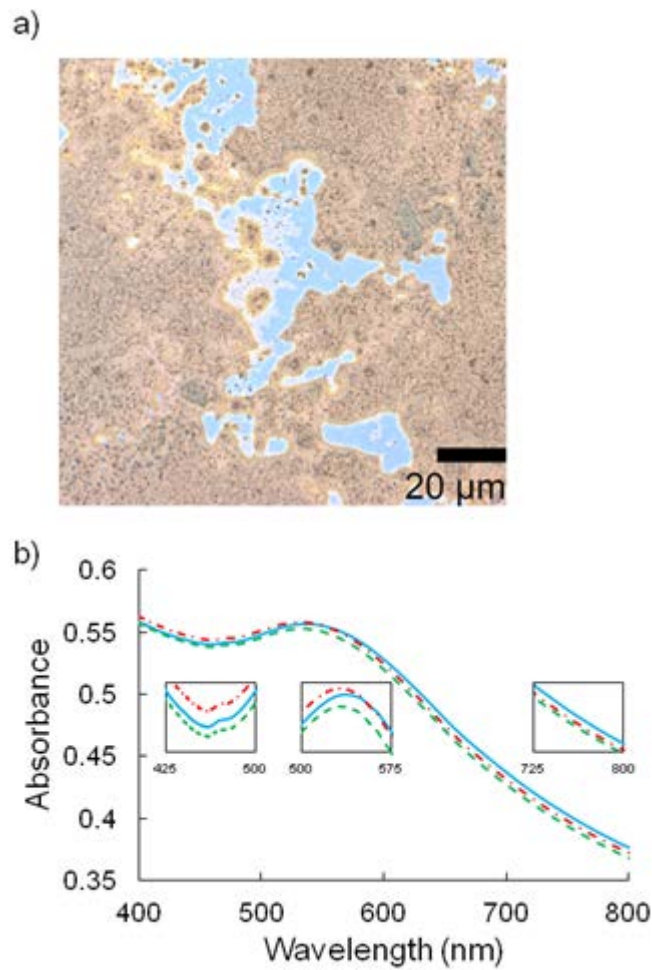
Figure 7-2. (a) Optical micrograph (1000×) of a C8-MPN film on a Si substrate; (b) visible absorbance spectrum of a C8-MPN coated glass slide prior to exposure (solid blue line), during static exposure to n-heptane (dashed green line), and during static exposure to toluene (dashed-dotted red line). Insets show enlargements of selected spectral regions. Absorbance was measured with reference to a blank glass slide.
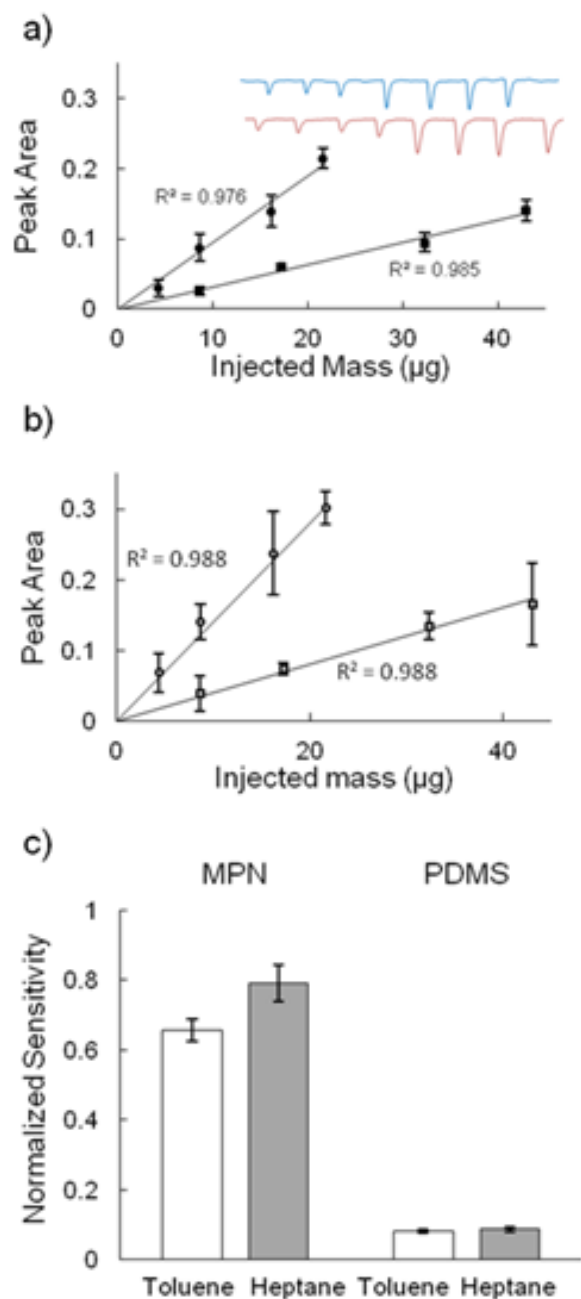
Figure 7-3. (a) 785 nm and (b) 488 nm laser reflectance calibration curves for vapors of toluene (circles) and n-heptane (squares) from a single C8-MPN coated Si device. Effective absorbance is plotted versus the injected mass of vapor. Error bars designate ± 1 standard deviation (n = 4 or 5 injections) and R2 values are from linear regression with a forced-zero intercept. Inset in a) shows a representative series of response profiles (peaks) for n-heptane (upper trace) and toluene (lower trace) at 785 nm. The bar charts in (c) show sensitivities to each vapor (as indicated) at 785 nm for the C8-MPN and PDMS coated devices (as indicated) normalized to the sensitivity at 488 nm. Error bars indicate ± one standard error of the slope.

147

Chapter VIII

A Micro-Optofluidic Ring Resonator Employing a Gold Nanoparticle Interface for Detection of Volatile Organic Compounds

8. 1 Introduction

As described in Chapter 7, thiolate monolayer gold nanoparticle (MPN) films are not only of value as interface films on chemiresistor sensors [1-4], but they also have interesting optical properties that make them good candidates as interface films in optical sensors. The optical absorbance and refractive index (RI) of MPN films are influenced by a localized surface plasmon resonance (LSPR), which arises from the interaction of light with free electrons on the surface of the gold nanoparticle cores. The absorption and RI of an MPN film at a given wavelength are affected by a number of variables, including the MPN core size and shape, packing order and intercore spacing, and the RI of the intercore matrix [5]. Sorption of volatile organic compounds (VOC) into the thiolate ligands which comprise the intercore matrix can induce changes in RI of the matrix as well as film volume and particle spacing. The resulting changes in optical properties of the film can be measured by optical transducers, such as the µOFRR described in Chapters 5 and 6, and enables detection of VOCs.

In previous studies of MPN interface films in optical sensors spectrophotometers were used to collect signals transmitted through or reflected from the films through free space [6-10]. A similar approach has been used for gas and VOC detection using gold nano-islands embedded in a polymer film [11]. Alternative sensor designs have been demonstrated, Chen et al. coated an MPN film on the interior of a long glass tube and used an LED to probe the film down its entire length (via internal reflectance) while monitoring changes in transmitted intensity with a photo-detector [12]. In all such studies, the sensitivity of measurements was quite low, leading to relatively high limits of detection for the VOC analytes explored. None of these configurations is well suited for miniaturization or incorporation with the components of microscale gas chromatography (µGC) for analysis of VOC mixtures.

Here we report on the assembly and characterization of MPN-coated µOFRR as a µGC detector. First, we present initial attempts to create a vapor sensor by coating an octane-thiolate (C8) MPN film on the interior of both a drawn-capillary OFRR and a µOFRR. These attempts failed to produce functioning devices. Next, we describe success creating an MPN-coated device using MPN material with better film forming properties, i.e., one with ligands derived from 1-mercapto-(triethylene glycol) methyl ether (TEG). Whispering gallery mode (WGM) resonance was excited in the µOFRR by evanescently coupling a laser source from a tapered fiber waveguide, and monitoring the output spectrum with a photo-detector. The device was connected downstream from two µGC separation columns and calibrated responses were generated for a 5-component VOC mixture and analyzed with respect to expectations on the basis of the vapor-ligand interactions and the known variables affecting responses from the µOFRR.

8.2 Experimental methods

8.2.1 Materials

Octane-thiolate (C8) MPNs were taken from existing stocks, which were synthesized according to the method of Rowe et al. [30] and had an average Au core diameter of 4.3 ± 0.9 nm. TEG-MPNs were purchased from Sigma Aldrich (Aldrich, St. Louis, MO) with a reported Au core diameter of 3.5-5.5 nm. The test compounds Isopropyl alcohol (IPA), heptane (C7), toluene (Tol), perchloroethylene (PCE), ethylbenzene (ETB), and all organic solvents were used as received (99%, Sigma Aldrich, St. Louis, MO. The vapor pressures of the test compounds (in kPa) are as follows (25 °C) [13]: IPA, 6.03; C7, 6.01; TOL, 3.81; PCE, 2.47; ETB, 1.26.

8.2.2. Device fabrication: Drawn-capillary OFRR

Capillary-drawn OFRRs were prepared using previously described methods [14-15]. The device consisted of a thinned silica capillary (final dimensions: i.d. ~50 μm, o.d. 55 μm) 3 cm in length with each end inserted into sections of larger connecting capillaries (i.d. 155 μm, o.d. 360 μm, 10 cm length) and sealed with adhesive (Hysol Epoxy Patch 1C, Rocky Hill, CT). The thinned capillary was stretched taut between two vertical posts mounted to an optics table and fixed in position with double-sided tape. A nanoparticle film was deposited on the interior of the thinned capillary using a static-coating method similar to that used to coat gas chromatography separation columns [16]. The OFRR was filled with a solution of C8 MPNs (24 mg mL^{-1}) dissolved in equal parts hexane and dichloromethane. The distal end of the OFRR was sealed with a small piece of heated paraffin wax ensuring no air bubbles remained in the device, and the proximal end was connected to a vacuum and held at a pressure of 21 kPa until the solvent had evaporated. The final nanoparticle film thickness was estimated at approximately 100 nm.

8.2.3 Device fabrication: µOFRR

The design and fabrication of the µOFRR was described in detail Chapters 4 and 5 as well as in previously published work [17-18]. The device comprises a hollow, SiO_x cylinder with a 250 µm i.d. and 1.2 µm thick walls, partially released from a Si substrate. The µOFRR is located in the center of a 2×2 cm chip, and provides a fluidic circuit from the top-side to the under-side. On the under-side of the chip is a plasma etched microfluidic channel that connects the µOFRR aperture to an expansion port. An etched channel running laterally across the top-side of the chip facilitates alignment of a fiber waveguide for evanescent coupling to the resonator. Figure 8-1 shows an illustration of the packaged sensor and an SEM image of the µOFRR.

C8 MPN films were deposited on the interior of µOFRR devices by adapting the procedure described in Chapter 5 for deposition of PDMS films. The front-side aperture of the resonator was sealed with a rubber septum and the volume of the resonator was filled with C8 MPN dispersed in toluene (2.5 mg mL^{-1}). The device was placed in a vacuum chamber and the solvent evaporated under low pressure. The presence of the MPN film on the interior of the device was confirmed with optical microscopy, however no WGM resonance was observed in C8 MPN coated devices.

A TEG MPN layer was deposited on the interior of the µOFRR by drop casting. TEG MPNs were dispersed in ethanol (2 mg mL^{-1}) and 5 µL of the solution was deposited over the under-side port of the µOFRR. The solution filled the resonator cavity without flowing out of the device due to surface tension at the µOFRR aperture. The solvent evaporated under ambient conditions. During initial optical characterization (described below) WGM resonance could not be detected with the coated device. A 5 µL drop of pure ethanol was placed on the backside port, filling the resonator, and re-dissolving then re-depositing the MPN film. Subsequent testing revealed WGM resonance. Assuming no loss of material during the re-deposition process, the final film thickness

is estimated as ~100 nm. The μOFRR backside fluidic channels were sealed with a 2×2 cm Pyrex coverplate using UV curable glue (NOA 81, Norland Optical, Cranbury, NJ). A short section of fused-silica capillary (250 μm i.d.) was sealed into the completed device for external fluidic connection.

8.2.4 OFRR characterization

WGM resonance was excited and measured within the walls of both types of devices by evanescently coupling laser light from an optical fiber waveguide. Details of this procedure are documented in Chapters 4, 5, and 6 as well as in previous publications [14-15, 17-18]. Light from a laser source (980 nm for drawn-capillary, 1550 nm for μOFRR) varied in wavelength over a range of several hundred pm while the output intensity across the fiber was measured with a photodetector and recorded by custom developed LabView software. During testing the inlet of the drawn-capillary OFRR was connected to the injection port of a benchscale gas chromatograph (3800, Varian, Inc., Palo Alto, CA) by a 1 m long connecting section of deactivated guard column. Helium was used as the carrier gas with flow rates ranging from 1-3 ml/minute. The resonant wavelength of each detected WGM was measured during injections of saturated VOC headspace and neat liquid analyte.

The μOFRR sensor was connected by deactivated capillary to an upstream separation μcolumn comprising two 3 m-long DRIE square spiral channels etched into Si chips, with a wall coating of PDMS [16, 19]. The μcolumn was held at 40 °C using an on-chip resistive heater, and the μOFRR was at room temperature (~22 °C). Test atmospheres containing a mixture of five VOCs were prepared in 3 L Tedlar bags. Four test atmospheres were prepared spanning a 10 fold range in concentrations for all analytes. 100 μL aliquots were drawn through a sample loop, and injected by way of a six-port valve into the separation column in dry air at 2.0 mL/minute. Each

injection was repeated 5 times. A single WGM resonance was recorded at a read rate of 16.7 hz, and λ_{WGM} was recorded during all exposures. Chromatograph data was analyzed using ORIGIN ® software (OriginLab Corp., Northampton, MA).

8.3 Results and discussion

8.3.1 Drawn-capillary OFRR

Numerous closely spaced resonances were measured with Q-factors (λ_{WGM}/FWHM) on the order of 10^5, comparable to data collected for bare and polymer coated drawn-capillary OFRRs [14-15]. However, no shift in λ_{WGM} was ever observed during exposure to VOC. Optical microscopic imaging of the MPN coated OFRR revealed poor uniformity of the nanoparticle coating (Figure 8-2). We hypothesized that heterogeneity or surface roughness in the nanoparticle film was scattering light at the glass-nanoparticle film interface, and degrading the circumferential modes which traveled around the inner surface of the OFRR. Therefore the resonant modes observed on the coated devices were strongly confined to the bulk or exterior of the glass, and were not sensitive to changes in the thickness or RI of the MPN film. Several aspects of the fabrication and deposition processes were experimentally varied to create a more uniform film: this included changes in choice of organic solvent, changes in nanoparticle concentration, use of surface passivating pre-treatment prior to coating, and use of a water bath to thermostat the OFRR during coating. Despite these efforts no attempt produced observable improvements in film uniformity or yielded a functioning MPN coated OFRR sensor.

8.3.2 μOFRR

The failure to excite resonance in the drawn-capillary OFRR motivated experiments with the μOFRR and a new choice of MPN. TEG was chosen to replace the C8 MPN as previous reports

suggested it assembled into more uniform films [6]. Still, devices as initially prepared did not support WGM resonance, only following re-deposition of the TEG film was a WGM successfully excited. The output spectrum of the coupled fiber is shown in Figure 8-3, and a ~8,000 Q-factor resonance is clearly visible. This value is lower than that of bare and PDMS coated devices described in Chapters 4 and 5 (typical Q-factor ~12,000), however it is sufficient for VOC sensing applications.

The success of this approach may be due to a confluence of factors. The TEG MPN forms more uniform and continuous films during solvent casting than C8, and therefore may not suffer from the same scattering and loss of resonance hypothesized to be responsible for earlier difficulties. The need to redeposit the original film confirms that loss of resonance can occur due to relatively small changes in film morphology, and that a homogeneous film is not guaranteed even with this type of MPN. Differences in geometry may also play a critical role. The µOFRR confines a single WGM in the narrow circumference of the small (3 nL) resonator volume; as such, depositing a MPN film in the µOFRR requires uniformity over only a very small surface area. Differences in cavity volume and geometry may also impact solvent evaporation rate and as a result casting of the film. Choice of excitation wavelength may also have been a key difference, the use of a longer wavelength (1550 nm vs 980 nm) reduces the degree of absorption by the MPN film and the degree of scattering by residual surface roughness. Further experiments are needed with drawn-capillary OFRRs to determine which set of experimental factors were key to sustaining resonance.

8.3.3 µOFRR as VOC detector

λ_{WGM} increased (red-shifted) during exposure to every VOC. The dashed spectrum displayed in Figure 8-3 depicts a representative shift in λ_{WGM} due to VOC sorption into the MPN

film. The analysis of μOFRR responses in Chapter 5 (5.3.2) reveals that red-shifts in λ_{WGM} arise from increases in the RI and/or in the thickness of the interface layer. Swelling of MPN films during VOC exposure is a well-documented phenomenon [9-10, 20], however there are no available measurements of TEG MPN refractive index and few available measurements of MPN refractive indices in general. Mallouk et al. modeled changes in the RI of gold nanoparticle dispersions in organic media for particles of similar size and volume fraction [21]. This model predicted RI in the infrared would increase with lower volume fraction (greater intercore distance) or increases in the dielectric constant of the organic medium. VOC sorption into MPN films has been shown to increase intercore spacing and to create measurable shifts in the dielectric constant of the thiolate meshing determined by the dielectric constant of the VOC [20, 22]. The observed red-shifts in λ_{WGM} are likely due to a combination of increasing film thickness and increasing intercore distance and the associated impact on RI, however the relative size of each contribution cannot be estimated from this data set.

Figure 8-4 shows a representative chromatogram with the MPN coated μOFRR functioning as a VOC detector. All five compounds eluted within 120 seconds and were well separated from one another, however isopropyl alcohol consistently co-eluted with an interferent we believed to be water vapor that permeated into the test atmosphere bags. In subsequent tests, samples of water vapor and ambient air at background humidity were injected into the μOFRR. Large responses confirmed high sensitivity to water vapor, a result of the polar/hydrophilic ether groups in the TEG ligand. Average peak widths ranged from 0.83 s (IPA) to 3.3 s (ETB) measured at half peak maximum for the largest injections. Peak widths increased with retention time and decreasing vapor pressure, a result of on-column band-broadening. These peaks were significantly broader than those reported in Chapter 5, a result of the lower column temperature.

The average responses to each vapor were calculated as chromatograph peak area, and are plotted against estimates of injected mass in Figure 8-5a and fit to linear regressions ($R^2 > 0.977$). Figure 8-5b contains a bar graph of the µOFRR sensitivity to each VOC, defined as the slope of the calibration regression. Of the five tested compounds the MPN µOFRR is most sensitive to ETB, confirming once again the dominant role analyte vapor pressure plays in dictating response in sorptive sensors. However, vapor pressure was not the sole determinant of sensitivity, as evident from the insensitive responses to C7. Figure 8-5c shows a bar graph with the sensitivity to each analyte normalized by saturated vapor pressure, noticeably the values are dissimilar between compounds, unlike the data presented in Chapters 5 and 6 for PDMS coated devices. Both C7 and PCE have responses comparatively lower than would be expected if response varied primarily due to analyte volatility. The low sensitivity to C7 may be a result of the polar TEG ligand having greater affinity for polar analytes and little affinity for non-polar C7, and the low sensitivity to PCE may be a result of the higher density minimizing the degree of volumetric swelling in the MPN film.

The sensitivity for C7 was ~12 times lower than the sensitivity measured in Chapter 6 by a PDMS coated µOFRR under similar conditions. Though direct comparisons are not available for other analytes, in general the MPN µOFRR proved less sensitive than PDMS coated µOFRR. The limit of detection (LOD) for each analyte was calculated using linear regressions of peak height against injected mass; LOD was defined as slope/3σ where σ is the standard deviation of the baseline ($\sigma = 0.514$ pm). Values for LOD ranged from 38 ng of ETB to 325 ng of C7. Though orders of magnitude higher than LODs found in Chapter 5 using a polymer sorptive layer, these values are considerably lower than those found using MPN films in reflection and transmission transducers for VOC sensing (Chapter 7) [9-10].

8.4 Conclusions

In summary, we have produced the first MPN coated WGM resonator and demonstrated its use as a VOC microsensor. The device requires smooth, uniform films to prevent degradation of the resonator Q-factor which can be accomplished through careful choice of nanoparticle functionalization and deposition method. Selecting materials which assemble into continuous, homogeneous films should reduce scattering and avoid difficulties exciting resonance in coated devices. We found the TEG MPN film suitable for achieving the necessary film uniformity within the μOFRR geometry. Q-factors of the coated device exceeded 8,000.

The λ_{WGM} of the TEG coated μOFRR red-shifted during VOC exposure, indicating that the WGM evanescently probed the MPN film and was sensitive to changes induced by VOC sorption. Shifts in λ_{WGM} were due to changes in the effective refractive index of the coated resonator, which can be attributed to changes in the MPN films refractive index due to increases in intercore spacing, and/or changes in the dielectric properties of the thiolate meshing, and possibly increases in the total thickness of the film.

Responses were reversible and proportional to VOC concentration. The magnitude of the response was driven by the amount of VOC that partitioned into the MPN film, and dependent on a combination of VOC vapor pressure and polarity. Sensitivity to VOCs was lower than sensitivities measured with PDMS coated devices, but higher than other optical sensors using MPNs as interface layers. As a result of the high Q-resonator the MPN film is probed several thousand times by circulating photons, amplifying the response to small changes in structure of the film. This establishes the μOFRR as a more sensitive platform for probing the optical responses of MPNs to organic vapors.

Future efforts will focus on probing nanoparticle coated devices at shorter wavelengths, closer to the LSPR maximum of the MPN film. MPN films are known to give differentiable responses when probed at multiple wavelengths, however this has not yet been demonstrated using an optical resonator. Coupling the WGM resonance to the nanoparticle film LSPR may offer enhanced selectivity, and if confirmed this phenomenon would allow for selective arrays of MPN coated µOFRR sensors probed at several discrete wavelengths.

8.5 References

1 .   F. I. Bohrer, E. Covington, C. Kurdak and E. T. Zellers, *Analytical chemistry* **2011**, *83*, 3687-3695.
2 .   Q.-Y. Cai and E. T. Zellers, *Analytical chemistry* **2002**, *74*, 3533-3539.
3 .   R.-S. Jian, R.-X. Huang and C.-J. Lu, *Talanta* **2012**, *88*, 160-167.
4 .   E. García-Berríos, T. Gao, M. D. Woodka, S. Maldonado, B. S. Brunschwig, M. W. Ellsworth and N. S. Lewis, *The Journal of Physical Chemistry C* **2010**, *114*, 21914-21920.
5 .   J. C. Love, L. A. Estroff, J. K. Kriebel, R. G. Nuzzo and G. M. Whitesides, *Chemical reviews* **2005**, *105*, 1103-1170.
6 .   R. A. Potyrailo, M. Larsen and O. Riccobono, *Angewandte Chemie International Edition* **2013**, *52*, 10360-10364.
7 .   C.-S. Cheng, Y.-Q. Chen and C.-J. Lu, *Talanta* **2007**, *73*, 358-365.
8 .   K.-J. Chen and C.-J. Lu, *Talanta* **2010**, *81*, 1670-1675.
9 .   K. Scholten, K. Reddy, X. Fan and E. T. Zellers, *Anal. Methods* **2013**, *5*, 4268-4272.
10 .   M. C. Dalfovo, R. C. Salvarezza and F. J. Ibañez, *Analytical chemistry* **2012**, *84*, 4886-4892.
11 .   T. Karakouz, A. Vaskevich and I. Rubinstein, *The Journal of Physical Chemistry B* **2008**, *112*, 14530-14538.
12 .   F.-Y. Chen, W.-C. Chang, R.-S. Jian and C.-J. Lu, *Analytical chemistry* **2014**.
13 .   P. J. Linstrom and W. G. Mallard in *WebBook, NIST Standard Reference Database Number 69*, *Vol.* National Institute of Standards and Technology, Gaithersburg, MD.
14 .   Y. Sun and X. Fan, *Optics express* **2008**, *16*, 10254-10268.
15 .   Y. Sun, J. Liu, D. J. Howard, G. Frye-Mason, A. K. Thompson, S.-j. Ja and X. Fan, *Analyst* **2010**, *135*, 165-171.
16 .   G. Serrano, S. M. Reidy and E. T. Zellers, *Sensors and Actuators B: Chemical* **2009**, *141*, 217-226.
17 .   K. Scholten, X. Fan and E. T. Zellers, *Applied physics letters* **2011**, *99*, 141108.
18 .   K. Scholten, X. Fan and E. T. Zellers, *Lab on a Chip* **2014**, *14*, 3873-3880.
19 .   S. Reidy, D. George, M. Agah and R. Sacks, *Analytical chemistry* **2007**, *79*, 2911-2917.

20 .   W. H. Steinecker, M. P. Rowe and E. T. Zellers, *Analytical Chemistry* **2007**, *79*, 4977-4986.

21 .   S. Kubo, A. Diaz, Y. Tang, T. S. Mayer, I. C. Khoo and T. E. Mallouk, *Nano letters* **2007**, *7*, 3418-3423.

22 .   W. H. Steinecker, M. Rowe, A. Matzger and E. Zellers, *TRANSDUCERS, Solid-State Sensors, Actuators and Microsystems, 12th International Conference on, 2003* **2003**, pp. 1343-1346.
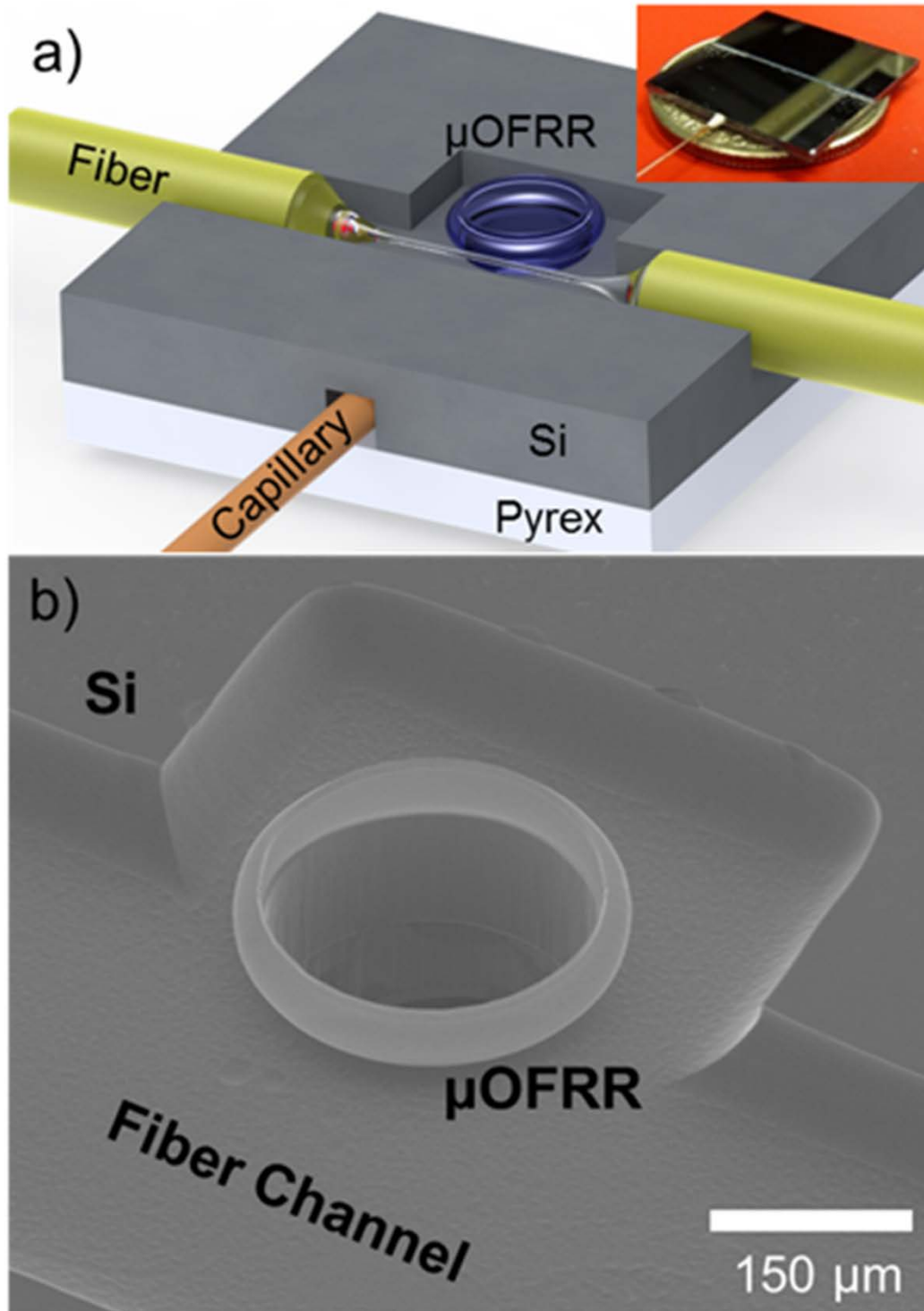
Figure 8-1 (a) Diagram of μOFRR with attached optical fiber and capillary connection. Inset shows photograph of device. (b) Scanning electron microscope image of a μOFRR, with 250 μm inner diameter and 1.2 μm thick walls.

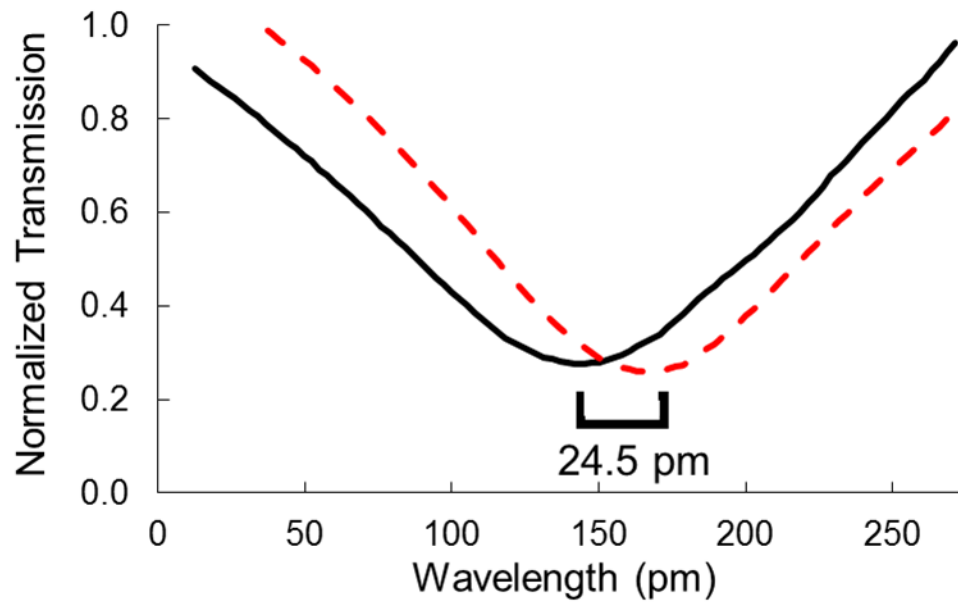Figure 8-2. Darkfield optical microimage of drawn-capillary OFRR with C8 MPN coating.

Figure 8-3. Normalized transmission across a tapered optical fiber coupled to MPN coated µOFRR displaying WGM resonance near 1550 nm for a device under a flow of dry, clean air (Black, solid line) and exposure to Ethylbenzene (red, dashed line).
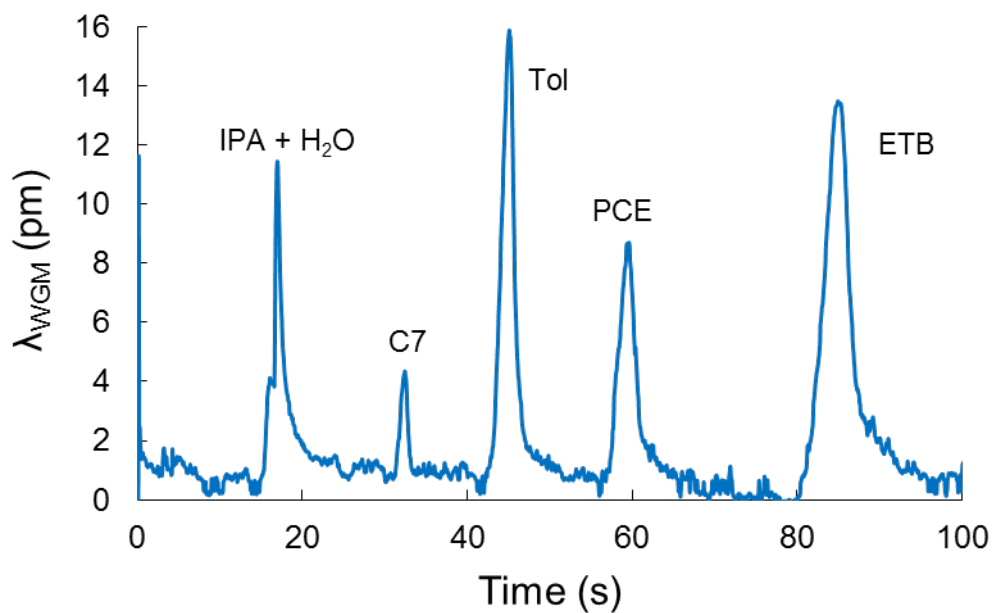
Figure 8-4. µGC separation of five VOCs with TEG coated µOFRR sensor as detector, using two 3-m long PDMS coated µcolumns at 40 °C and the (downstream) µOFRR sensor at 22 C. Injected masses were approximately 1.2 µg isopropyl alcohol, 2.0 µg heptane, 2.5 µg toluene, 2.4 µg perchloroethylene, and 1.3 µg ethylbenzene.
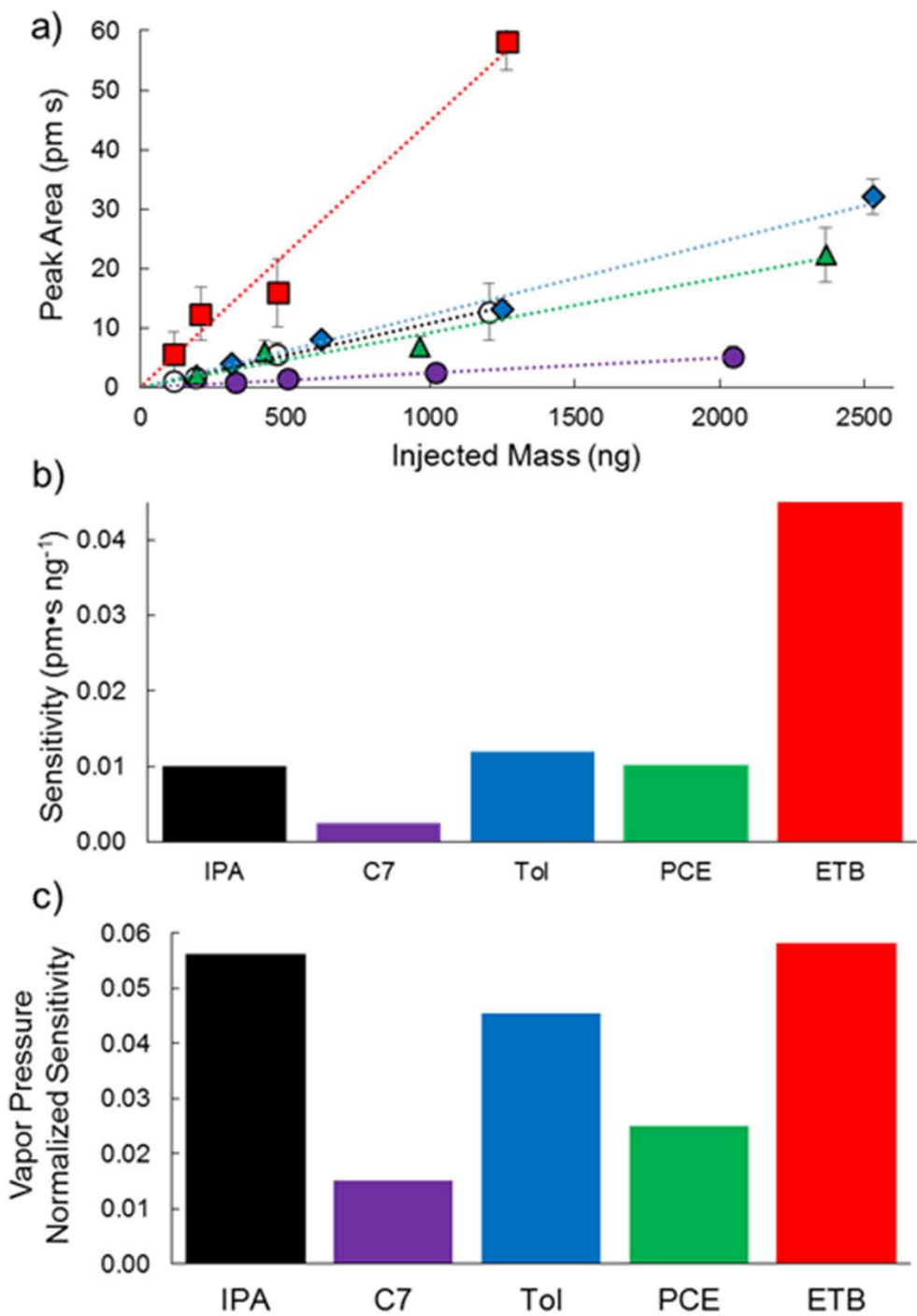
Figure 8-5. (a) Calibration curves for heptane (filled circles), PCE (triangles), isopropyl alcohol (unfilled circles), toluene (diamonds), and ethylbenzene (squares). Error bars represent +/- one standard deviation from 5x replicates. (b) µOFRR sensitivity to each VOC analyte derived from regression slope. (c) µOFRR sensitivity normalized to analyte saturated vapor pressure in kPa.

164

Chapter IX

Summary and Conclusions

This dissertation describes the development of microfabricated sensors and sensor arrays for volatile organic compounds (VOC) and their evaluation as detectors in micro-scale gas chromatographic (µGC) instrumentation. A primary focus was placed on the creation and characterization of a new type of optical vapor sensor: the microfabricated optofluidic ring resonator (µOFRR). The principal results from this highly successful project include the following: 1) the microfabrication of robust, high aspect-ratio, optofluidic resonator structures with novel adaptations of Si micromachining; 2) the invention, demonstration and analysis of a µOFRR VOC detector exhibiting < ng detection limits and rapid response times; 3) the demonstration of VOC differentiation with multi-wavelength responses from a single MPN film; 4) the creation and study of a MPN coated µOFRR sensor.

This research was motivated by the need, in µGC development, for VOC microsensor arrays that provide rapid, sensitive, diverse, and reversible responses to a variety of analytes. Initial efforts focused on existing microsensor designs: MPN coated chemiresistors, tin-oxide nanowires (NW) chemiresistors, and thickness-shear mode resonators (TSMR). Two separate studies examined the classification of VOCs and VOC mixtures using hybrid multi-material arrays (MPN chemiresistors and NW chemiresistors) and hybrid multi-transducer arrays (MPN chemiresistors and MPN TSMRs). The former study (Chapter 2) explored organic vapor discrimination using chemiresistors employing contact-printed mats of NW on micro-hotplate membranes and solvent

cast films of MPNs on interdigital electrodes operated at room temperature. We compared the performance and the 'complementarity' of these two types of sensors. Calibrated responses from a NW chemiresistor operated at two different temperatures and from a set of four different MPN-chemiresistors were generated for three test vapors. This pooled data set was then analyzed using principal components regression classification models with varying degrees of random error superimposed on the responses via Monte Carlo simulation in order to estimate the rates of recognition/discrimination for arrays comprising different combinations of sensors. Results indicate that the diversity of most of the dual MPN-chemiresistor arrays exceeded that of the dual NW-chemiresistor array. Additionally, in assessing all possible arrays of 4-6 sensors, the recognition rates of the hybrid arrays (i.e., MPN+NW) were no better than that of the 4-sensor array containing only MPN-chemiresistors.

The success with the MPN devices inspired a study (Chapter 3) exploring whether arrays of vapor sensors assembled from two different types of transducers provide greater response diversity than arrays of a single transducer (ST) type. Calibrated sensitivities to five vapors on chemiresistors (CRs) and TSMRs coated with matching interface films of four different MPNs were considered. A pooled set of 40 vapor-sensor sensitivities was analyzed using principal components regression models in conjunction with Monte Carlo simulations to evaluate the classification performance with different levels of error superimposed on the sensor responses. Recognition rates (RR) were estimated for the individual vapors and their binary mixtures with virtual arrays consisting of all possible combinations of MPNs and transducer types. The best overall performance was obtained with a multi-transducer (MT) array of n = 4 sensors, which provided average RRs of 99.7% for individual vapor discrimination and 74.7% for discrimination of the 10 binary mixtures from their components, both with 5% superimposed error. MT-array RR

values did not improve for n > 4. Results demonstrated that MT arrays can provide modestly greater diversity than ST arrays of similar dimension.

The studies in Chapter 2 and Chapter 3 confirmed the limited ability of microsensor arrays to correctly identify even two VOCs when presented simultaneously, and highlighted the need for a microsensor which would preserve chromatographic separation in a µGC system. Motivated by reports of drawn-capillary optofluidic ring resonators (OFRR) used in GC applications, subsequent work focused on the creation of a µOFRR, to improve upon the sensitivity and form-factor of the existing devices. Chapter 4 describes the fabrication and preliminary optical characterization of rugged, Si-micromachined µOFRR structures consisting of thin-walled SiOx cylinders with expanded midsections designed to enhance the three-dimensional confinement of whispering gallery modes (WGMs). These µOFRR structures were grown thermally at wafer scale on the interior of Si molds defined by deep-reactive-ion etching and pre-treated to reduce surface roughness. Devices 85-µm tall with 2-µm thick walls and inner diameters ranging from 50-200 µm supported pure-mode WGMs with Q-factors $>10^4$ near 985 nm. Devices proved robust despite the thin walls and high aspect ratio, and Q-factors were sufficiently high for sensing applications while not dependent on device circumference.

Chapter 5 details the creation and characterization of a µOFRR sensor, which combines vapor sensing and fluidic transport functions in a monolithic microstructure. The device is a variation of the designs presented in Chapter 4; the sensor comprises a hollow, vertical SiOx cylinder (250-µm i.d., 1.2-µm wall thickness; 85-µm height) with a central quasi-toroidal mode-confinement section, grown and partially released from a Si substrate. The device also integrates on-chip fluidic-interconnection and fiber-optic probe alignment features. High-Q WGMS generated with a tunable 1550-nm laser exhibited rapid, reversible shifts in resonant wavelength

arising from polymer swelling and refractive index changes as vapors partition into the ~300-nm

PDMS film lining the cylinder. Steady-state sensor responses varied in proportion to concentration

over a 50-fold range for the five organic vapors tested, provided calculated detection limits as low

as 0.5 ppm (v/v) (for m-xylene and ethylbenzene). In dynamic exposure tests, responses to 5-µL

injected m-xylene vapor pulses 710 ms wide were only 18% broader than those from a reference

flame-ionization detector and also varied linearly with injected mass; 180 pg was measured and

the calculated detection limit was 49 pg without use of preconcentration or split injection, at a flow

rate compatible with efficient chromatographic separations. In a preliminary demonstration, the

µOFRR was connected downstream from a micromachined gas chromatographic separation

column, and the device was successfully used as a µGC detector for a simple VOC mixture

analysis.

Chapter 6 describes the development and characterization of a microanalytical system

comprising the µOFRR sensor and a comprehensive two-dimensional µGC subsystem (µGC ×

µGC). The µOFRR was packaged into a detector assembly with miniaturized ancillary components

including photodetector and optical fiber connections, and connected downstream from Si-

micromachined first- and second-dimension separation columns and a Si-micromachined thermal

modulator (µTM). The first dimension µcolumn consisted of two 3.1×3.1 cm chips with an etched

channel 6 m long coated with a PDMS stationary phase. The second dimension consists of a 1.2

$\times$ 1.2 cm µcolumn chip with an etched channel 0.5-m long coated with a commercial

poly(trifluoropropylmethyl siloxane) (OV-215) stationary phase. The 2-stage µTM chip contained

two series coupled, square spiral channels 4.2 and 2.8 cm long coated with PDMS. Isothermal

separations of a simple alkane mixture (C7-C10) produced symmetric peaks and modulation

numbers ranging from 2-6; early eluting peaks had narrow widths, however the widths became

larger as the volatility of the analyte decreased. A 7-component mixture was separated using the μOFRR detector and a FID reference. For high volatility analytes the μOFRR peak responses were no broader than the FID reference, and modulated peaks as sharp as 125 ms were achieved. An 11-component mixture was analyzed in this first demonstration of a μGC × μGC separation incorporating a microsensor for VOC detection and microfabricated modulator.

The lack of selectivity provided by the PDMS coated μOFRR sensor motivated study of alternative interface layers. In Chapter 7, sorption-induced changes in the localized surface plasmon resonance (LSPR) of an n-octanethiolate-MPN film were exploited to differentiate two organic vapors with a single sensor. Absorbance spectra of the film were recorded during exposure to toluene and n-heptane; sorption of each analyte induced unique spectral changes. Probing the film with 488-nm and 785-nm lasers gave reflectance sensitivity ratios at the two wavelengths of 0.68 and 0.80 for toluene and n-heptane, respectively, permitting their discrimination without reliance on spectroscopy. Analysis revealed swelling-induced increases in inter-particle distance appeared to predominate over changes in the refractive index of the inter-particle matrix in the reflectance responses.

Chapter 8 describes the creation of an MPN coated μOFRR sensor. Initial attempts to create a drawn-capillary OFRR coated with an n-octanethiolate-MPN film proved unsuccessful and subsequent efforts focused on producing a μOFRR coated with a 1-mercapto-(triethylene glycol) methyl ether (TEG) MPN film. This was the first demonstration of a WGM resonator coated with a MPN film. The improved film uniformity achieved with the TEG MPN film proved critical to maintaining WGM resonance with the nanoparticle coating. The MPN coated device functioned as a VOC detector with sensitivities considerably higher than the LSPR-MPN reflectance sensor. The sensor was attached downstream from a μGC separation column and calibrated responses

were generated from a 5-component VOC mixture across a 10 fold range of analyte concentrations. Responses were dominated by analyte vapor pressure and polarity, the TEG ligand exhibited strong affinity, and correspondingly strong responses, to polar analytes.

There are several additional tasks and experiments that could be performed in the future to improve upon or further validate this work. One such task is the creation of an array of µOFRR sensors, arranged in series or in parallel, each coated with a different interface layer (polymer or MPN). A small array used as the detector in a µGC or µGC $\times$ µGC systems would facilitate the recognition/discrimination of VOC mixture components separated or partially separated by the upstream columns.

Additional work could focus on improvements to the µOFRR fabrication. Alternative methods to reducing surface roughness, such as H_2 Si annealing, could potentially improve the quality factor (and as a result LOD) by an order of magnitude, and reduce cost and fabrication time significantly. LODs may also be improved by further reducing the µOFRR wall thickness.

Future work should also examine the response (sensitivity and peak width) of MPN- or polymer-coated µOFRR sensors as a function of temperature. The work presented in Chapters 5, 6, and 8 demonstrates that µOFRR sensitivity and response time is strongly dependent on volatility of analytes, which can be controlled through changes in temperature. Temperature programming a µOFRR during a µGC separation may significantly improve peak capacity without significantly decreasing sensitivity by reducing peak widths of less-volatile compounds for which the peak width is broadened by slow desorption kinetics.

Finally, MPN coated µOFRRs should be tested with WGMs excited at shorter wavelengths. VOC sensitivity should be measured at several (visible) wavelengths to test if the selectivity

demonstrated in Chapter 7 can be reproduced with the resonator sensor. This would create a new type of optical sensor that can exploit the response diversity of plasmonic films with the sensitivity of WGM resonators.

In conclusion, several advancements in the state-of-the-art in VOC microsensors as well as micro-optics have been described in this dissertation. The µOFRR is a novel WGM resonator that improves upon existing designs for OFRRs in several ways, and the fabrication method represents a new approach for creating optical micro-cavities. This dissertation includes the first demonstration of a microfabricated optofluidic resonator for VOC sensing, the first demonstration of an optical resonator for µGC detection, and the first demonstration of a microsensor of any sort for µGC $\times$ µGC detection with microfabricated modulator. Characterization of the µOFRR revealed several properties that augur well for use in VOC detection, including high sensitivity, very low dead-volume, and fast response times. The use of a plasmonic interface film offers an intriguing way to increase response diversity, and could open new avenues of research into selective and sensitive VOC microsensors.

APPENDICES

Appendix I. Fabrication procedure for µOFRR structures and resonators

1. **(A)** Begin with double-sided polished wafers with oxide layer (1.5 µm thick) on both sides
   a. If not available grow oxide layer on double-sided polished wafers with wet thermal oxide growth
2. Clean wafer(s)
   a. Piranha (3:1 Sulfuric:H_2O_2) or Nanostrip to remove any organic contamination. 5 minutes.

Etch insertion port, microfluidic channel and backside aperture of the µOFRR

3. **(B)** Photoresist **Mask I** (Mask I defines the features of the insertion port)
   a. Spin SPR 220-3 to 4 µm thickness using ACS cluster tool or photoresist spinner.
4. Expose shadow mask I
   a. 8 seconds UV exposure, soft contact, with MA6 aligner
5. Post exposure bake
   a. 90s on 115 °C hotplate
6. **(C)** Develop PR mask I
   a. 60 seconds AZ300 MIF developer spray
7. O_2 plasma clean
   a. 60 second descum with YES plasma stripper
8. Wafer mount to protect backside oxide
   a. Spin 1827 resist @ 2k rpm for 5 seconds on dummy wafer
   b. Align flats and mount wafer (Feature side up)
   c. Place mounted wafers on 110 °C hotplate for 2 minutes
9. **(D)** Buffered HF etch
   a. ~850 seconds in recirculating BHF tank set @ 20 °C
10. **(E)** Strip resist/unmounts wafers
    a. Hot PRS 2000 for 10 minutes
    b. Separate wafers
    c. Hot PRS 2000 for 10 minutes
    d. Rinse and Spin Rinse Dry

11. Clean wafer(s)
    a. Piranha (3:1 Sulfuric:H_2O_2) or Nanostrip to remove any organic contamination. 5 minutes.Short HF dip
        i. ~30s in 100:1 HF to remove oxide grown by oxidizers
12. **(F)** Photoresist **Mask II** (Mask II defines the backside aperture of the µOFRR)
    a. Spin SPR 220-3 to 4 µm thickness using ACS cluster tool or photoresist spinner.
13. Expose shadow mask II
    a. 8 seconds UV exposure, soft contact, with MA6 aligner –
        requires alignment with mask I
14. Post exposure bake
    a. 90s on 115 °C hotplate
15. **(G)** Develop PR mask II
    a. 60 seconds AZ300 MIF developer spray (ACS cluster tool)
16. O_2 plasma clean
    a. 60 second descum with YES plasma stripper
17. Wafer mount to protect backside oxide
    a. Spin 1827 resist @ 2k rpm for 5 seconds on dummy wafer
    b. Align flats and mount wafer (Feature side up)
    c. Place mounted wafers on 110 °C hotplate for 2 minutes
18. **(H)** Buffered HF etch
    a. ~850 seconds in recirculating BHF tank set @ 20 °C
19. **(I)** Strip photoresist/un-mount wafers
    a. Hot PRS 2000 for 10 minutes
    b. Separate wafers
    c. Hot PRS 2000 for 10 minutes
    d. Rinse and Spin Rinse Dry
20. Clean wafer(s)
    a. Piranha (3:1 Sulfuric:H_2O_2) or Nanostrip to remove any organic contamination. 5 minutes.
    b. Short HF dip
        i. ~30s in 100:1 HF to remove oxide grown by oxidizers
21. **(J)** Photoresist **Mask II+III** (Mask III defines the insertion port and the microfluidic channel, mask II defines backside aperture of the µOFRR)
    a. Spin SPR 220-3 to 4 µm thickness using ACS cluster tool or photoresist spinner.
22. Expose shadow mask II and III consecutively
    a. ~12 seconds UV exposure, soft contact, with MA6 aligner -
        requires alignment with previous masks
23. Post exposure bake
    a. 90 seconds on 115 °C hotplate

24. **(K)** Develop PR mask II + III
    a. 60 seconds AZ300 MIF developer spray (single development step)
25. HF dip
    a. 30 second 100:1 HF dip to remove any residual oxide layer prior to plasma etch
26. Mount wafer for use in Pegasus DRIE deep etcher

     a. 80 °C hotplate, ~3-3.3 g crystal bond 555,

     b. 5 minute vacuum degas, 5 minute vacuum to seal

27. **(L)** Deep Reactive Ion Etch (DRIE)

     a. 'LNF recipe 1' for ~19.4 minutes

         i. 130 μm etch at rate of 6.7 μm a minute, will need to adjust time for different etch rate

28. Inspect, measure etch depth with Zygometer

29. Un-mount wafers

     a. Heat wafers up on 90 °C hotplate for a few seconds, carefully slide apart wafers

     b. DI water bath to remove crystal bond

30. O_2 plasma clean

     a. 60 second descum with YES plasma stripper

31. Optional: measure oxide thickness with Nanospec tool

32. Mount wafer (photoresist) to protect backside oxide

33. Wafer mount to protect backside oxide

     a. Spin 1827 resist @ 2k rpm for 5 seconds on dummy wafer

     b. Align flats and mount wafer (Feature side up)

     c. Place mounted wafers on 110 °C hotplate for 2 minutes

34. **(M)** Buffered HF etch

     a. ~550 seconds in recirculating BHF tank set @ 20 °C

         i. Time in this step will depend on value measured in step 31 and etch rate of BHF bath

     b. DI water rinse

35. **(N)** Strip photoresist/un-mount wafers

     a. Hot PRS 2000 for 10 minutes

     b. Separate wafers

     c. Hot PRS 2000 for 10 minutes

     d. Rinse and Spin Rinse Dry

36. Clean wafer(s)

     a. Piranha (3:1 Sulfuric:H_2O_2) or Nanostrip to remove any organic contamination. 5 minutes.

     b. Short HF dip

         i. ~30s in 100:1 HF to remove oxide grown by oxidizers

37. Mount wafer for use in Pegasus DRIE deep etcher

     a. 80 °C hotplate, ~3-3.3 g crystal bond 555,

     b. 5 minute vacuum degas, 5 min vacuum to seal

38. **(O) DRIE**

     a. Recipe 'LNF Recipe 1' on Pegasus deep etcher for 35:45

         i. Desired etch depth ~250 μm

             1. Adjust etch time as needed based on etch rate

39. Inspect, measure etch depth with Zygometer

FINAL DESIRED ETCH DEPTHS:
Insertion port: ~375 μm
μOFRR aperture: ~350 μm
Microfluidic channel: ~250 μm

40. Un-mount wafers
    a. Heat wafers up on 90 °C hotplate for a few seconds, carefully slide apart wafers
    b. DI water bath to remove crystal bond
41. Clean wafer(s)
    a. Piranha (3:1 Sulfuric:H_2O_2) or Nanostrip to remove any organic contamination. 5 minutes.
    b. Short HF dip
        i. ~30s in 100:1 HF to remove oxide grown by oxidizers

42. XeF_2 etch
    a. 5 cycles of 60 seconds @ 3 Torr
        i. This etch step serves to remove residual Si 'ledge' between insertion port/microfluidic channel, and around the lip of the μOFRR aperture

Define μOFRR and large section of alignment channel using front side etch

43. **(P)** For the rest of the steps, features will be defined on the opposite side
44. Measure total thickness of wafer(s)
45. Measure thickness of oxide on the front
46. **(Q)** Photoresist **Mask IV+II** (Mask IV defines the features of the deepest part of the alignment channel, Mask II defines the front aperture of the μOFRR)
    a. Spin SPR 220-3 to 4 μm thickness using ACS cluster tool or photoresist spinner.
47. Expose shadow mask IV+II
    a. 12 seconds UV exposure, soft contact, with MA6 aligner
    b. This will require backside alignment with previous masks
        i. Recommend checking alignment to backside features as well as to oxide etched features of Mask IV
48. Post exposure bake
    a. 90s on 115 °C hotplate
49. **(R)** Develop PR mask IV+II
    a. 70 seconds AZ300 MIF developer spray (ACS cluster tool) (single developer step)
50. O_2 plasma clean
    a. 60 second descum with YES plasma stripper
51. Wafer mount to protect backside oxide
    a. Spin 1827 resist @ 2k rpm for 5 seconds on dummy wafer
    b. Align flats and mount wafer (Feature side up)
    c. Place mounted wafers on 110 °C hotplate for 2 minutes
52. **(S)** Buffered HF etch
    a. ~750 seconds in recirculating BHF tank set @ 20 °C
        i. This time will need to be adjusted based on results of measurement in step #44

53. **(T)** Strip photoresist/un-mount wafers
    a. Hot PRS 2000 for 10 minutes
    b. Separate wafers
    c. Hot PRS 2000 for 10 minutes
    d. Rinse and Spin Rinse Dry
54. Clean wafer(s)
    a. Piranha (3:1 Sulfuric:H_2O_2) or Nanostrip to remove any organic contamination. 5 minutes.
55. Mount wafer(s) for use in Pegasus DRIE deep etcher
    a. 80 °C hotplate, ~3-3.3 g crystal bond 555,
    b. 5 minute vacuum degas, 5 min vacuum to seal

56. Custom DRIE etch
    a. Pegasus Deep Etcher
        i. 'LNF recipe 1' ~5:30 (etch depth ~)
        ii. 3 minute C_4F_8 passivation step
        iii. 45 second 'breakthrough' step
    b. **(U)** XeF$_2$ Xactix
        i. 10 cycles for 60 seconds @ 3 Torr (etch depth ~)
    c. **(V)** Pegasus Deep Etcher
        i. 'LNF recipe 1' ~20 minutes (etch depth ~)

NOTE: The etch times here are approximations, which will vary with etch rates, desired dimensions, the final etch depth from step #39 and the thickness of the wafer.

The total etch depth should be deep enough to create a 'via' through the wafer to complete the fluidic circuit within the µOFRR. For a 525 µm wafer this will be approximately 175 µm. Step 55a step will define the distance between the center of the toroidal expansion and the top of the µOFRR. Step 55b etch will define the diameter and height of the toroidal expansion. The depth etched in 55b must be less (typically half) of the amount etched in 55a.

From previous measurements:
55a should etch a total of 48 microns (36 microns in DRIE etch, 12 microns in breakthrough   step)
55b should etch 25 microns iso-tropically
55c should etch 120 microns

57. Un-mount wafers
    a. Heat wafers up on 90 °C hotplate for a few seconds, carefully slide apart wafers
    b. DI water bath to remove crystal bond
58. **(W)** HF etch to remove all oxide
    a. ~10 minute 1:1 HF:DI water etch depending on final oxide thickness
    b. DI water rinse
59. Clean wafer(s)
    a. Piranha (3:1 Sulfuric:H_2O_2) or Nanostrip to remove any organic contamination. 5 minutes.
    b. DI water rinse
    c. Spin rinse dry

Sidewall 'smoothing' step and structural oxide growth

    Optional: Use SEM to examine roughness on interior of µOFRR sidewalls
60. Pre-furnace clean
    a. See LNF SOP regarding pre-furnace clean
61. (X) Wet oxide growth
    a. Dry:Wet:Dry growth @ 1100 C
        i. 10 minute dry growth
        ii. 5 hour 19 minute wet growth
        iii. 10 minute dry growth
        iv. 20 minute N_2 anneal
    b. 1.5 µm oxide growth
62. **(Y)** HF etch to remove 'smoothing' oxide
    a. 1:1 HF:DI water ~10 minutes
        Note: BHF will not reach oxide inside small 'vias', must be 1:1 HF in water
63. Repeat steps 60 & 61 2 times
64. Inspect sidewalls to check that roughness incurred from DRIE steps has been significantly reduced

65. **(Z)** Structural growth
    a. Repeat steps 59 & 60, with the length of the wet growth tailored to the desired wall thickness of the μOFRR
    b. Typical wall thickness in μOFRR sensor – 1.2 μm
66. **(AA)** Chemical-mechanical polish
    a. Recipe "LNF-Oxide" on IPEC 472 tool
        i. 3x 5 minute long polish steps
        ii. Back pressure: 3.2 psi
        iii. Pressure: 5 psi
        iv. RPM ~45-50
67. RCA Clean 1 to remove contaminants from CMP step
    a. 5:1:1 DI:H_2O_2:NH_4OH
    b. ~1 min 100:1 HF etch

Alignment channel and partial release of μOFRR

68. **(AB)** Photoresist **Mask V** (Mask V defines the shallow section of the alignment channel and the partial release of the μOFRR)
    a. Spin 1827 resist @ 1500k RPM for 30 seconds with 1200 acceleration/ramp using manual spinner
        i. As the wafer(s) now have vias, be careful with choice of vacuum chuck and spin speed, as the chuck may lose vacuum and break wafer.
69. Expose through shadow mask V
    a. 80 seconds UV exposure, soft contact, with MA6 aligner –
    requires alignment with mask I
70. **(AC)** Develop PR mask V
    a. MIF319 developer (tank) for 1 minute
71. 1 min 100:1 HF etch
72. **(AD)** XeF_2 etch
    a. ~35 cycles for 30 seconds @ 3 Torr
        i. Etch depth will determine height of release, must be deep enough to expose entire toroidal bulge. ~80 μm deep etch.

73. **(AE)** Strip photoresist/un-mount wafers
    a. Hot PRS 2000 for 10 minutes
    b. Separate wafers
    c. Hot PRS 2000 for 10 minutes
    d. Rinse and Spin Rinse Dry

Dice and Clean

74. **D**ice with ADT 7100 Dicing Saw dicing saw
    a. S1230-Q5HH-000 Si blade
    b. Wafer(s) diced into 2×2 cm chips
75. RCA Clean 1 to remove contaminants from CMP step
    a. 5:1:1 DI:H_2O_2:NH_4OH
    b. ~30 second 100:1 HF etch

Diagrams of Si cross section

Under-Side Processing

(A)

(B)

(C)

(D)

(E)

(F)

(G)

(H)

(I)

(J)

180

(K)

(L)

(M)

(N)

(O)
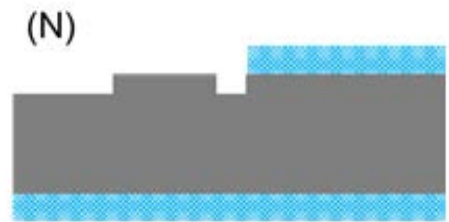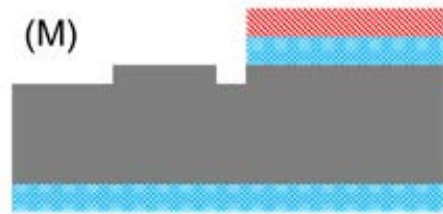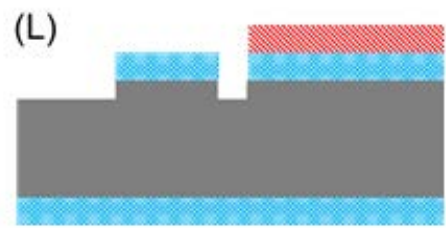
Front-Side Processing

(P)

(Q)

(R)

(S)

(T)

(U)

(V)

(W)

(X)

(Y)

(Z)

(AA)

(AB)

(AC)

(AD)

(AE)
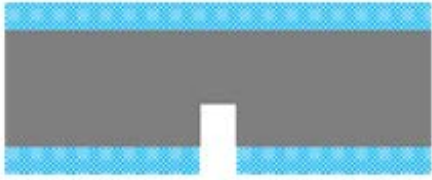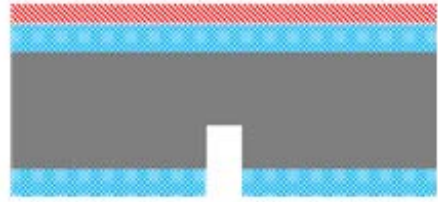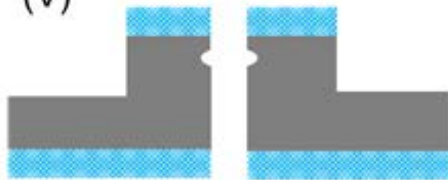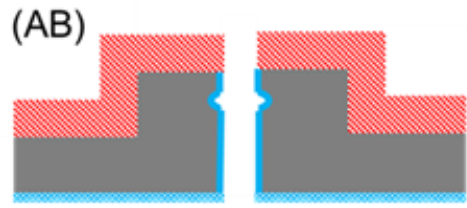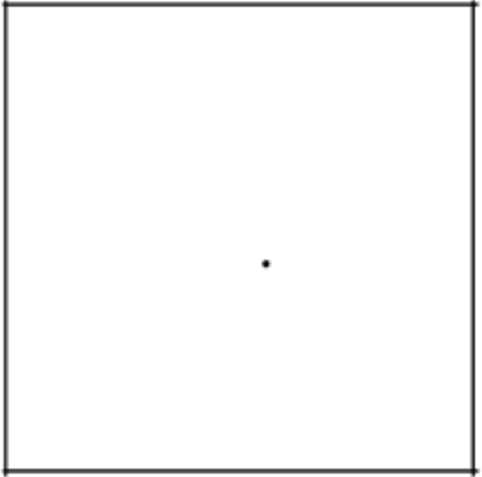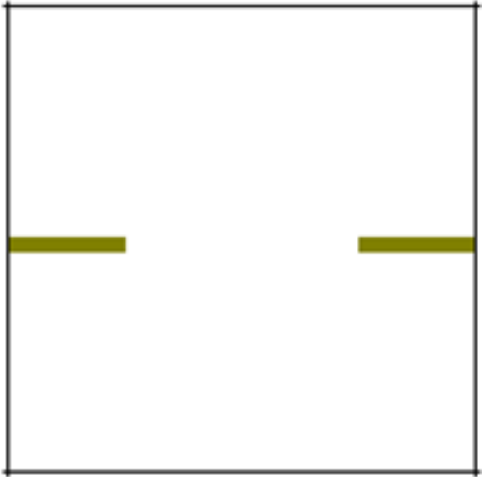
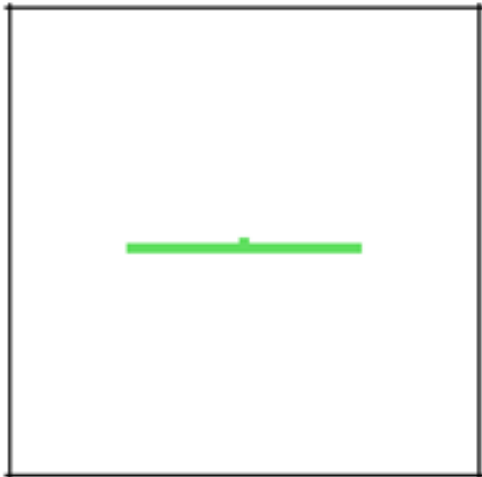# Shadow Masks
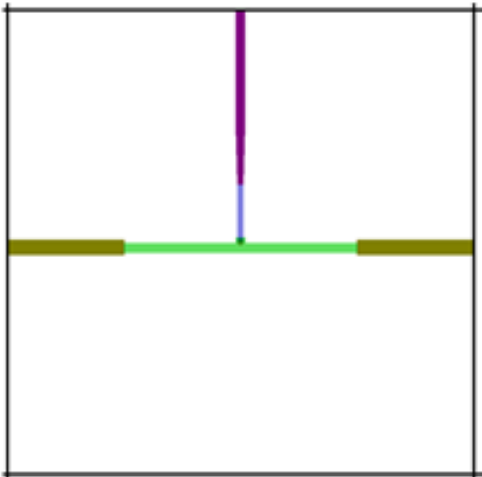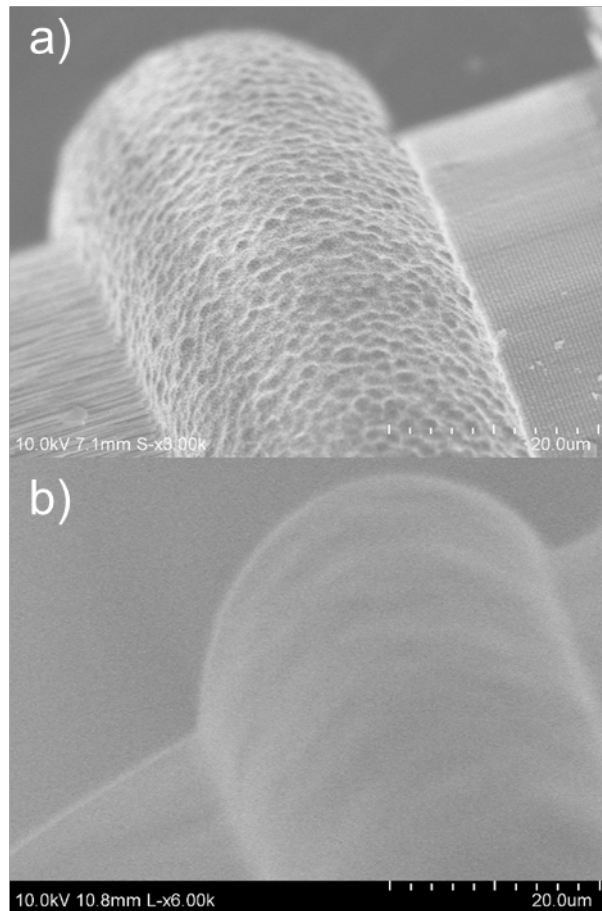
Appendix II. Supplemental information for Chapter 4

Figure A2-1. SEM of a wafer cross-section showing the plasma etched 'mold' of the µOFRR structure (a) before and (b) after reducing sidewall roughness with a series of oxidation growths.

Appendix III. Supplemental information for Chapter 7

Loss of LSPR absorbance peak upon exposure to saturated toluene. During preliminary testing, a C8-MPN coated glass slide was exposed to a saturated test atmosphere of toluene, created by injecting ~5 µL of neat liquid toluene into the cuvette that housed the C8-MPN coated glass substrate, and replacing the lid of the cuvette. Initially, the absorbance spectrum exhibited the blue shift in λ_{max} as described in the text of the article. However, over the course of several minutes the total absorbance decreased significantly, λ_{max} red shifted, and then the LSPR band diminished almost completely. Figure A3-1 displays the spectra prior to and after this change. Even after removing the sample from the cuvette and allowing it to stand unexposed for 24 hrs, the LSPR band did not reappear. Re-exposure to toluene vapor also had no effect. The sample was then removed from the cuvette and the MPN film was treated with a few drops of liquid toluene to redissolve the MPNs. The solvent was allowed to evaporate, leaving a recast film, the uniformity of which was visually degraded; a 'coffee-ring' pattern was evident in which the thickness at the periphery of the film patch was obviously much greater than in the central region. Upon replacement of the sample in the cuvette and collection of the absorbance spectrum, the LSPR peak returned, though at reduced intensity.

We cannot explain the loss of the LSPR peak upon initial exposure to this high concentration of toluene, but it obviously causes massive changes in film morphology, perhaps involving widespread agglomeration. We have observed analogous drastic increases in MPN film resistance upon exposure to high toluene vapor concentrations with CR sensors (unpublished results), and we note that Garcia-Berrios, et al. reported a similar permanent loss of film conductivity upon exposure of a C8 MPN film on a CR device to saturated atmosphere of ethanol.[1]

References

1. E. Garcia-Berrios, T. Gao, M. Woodka, S. Maldonado, B. Brunschwig, M. Ellsworth and N. Lews, *J. Phys. Chem. C*, 2010 114, 21914- 21920.
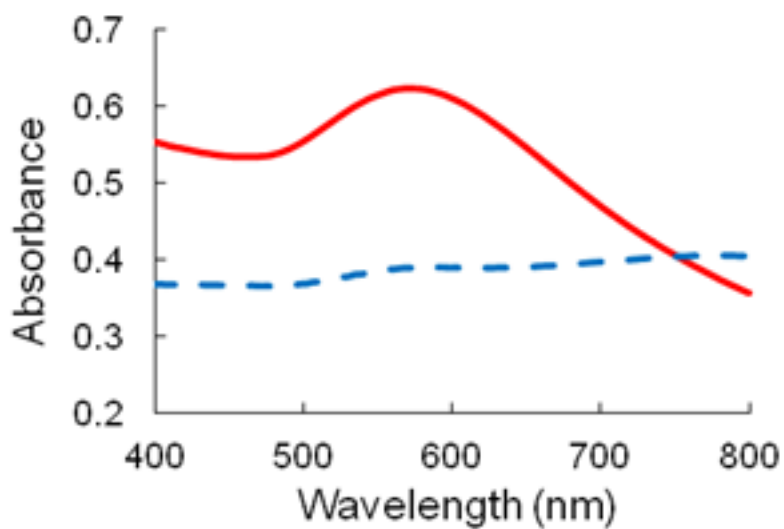
Figure A3-1. Visible absorbance spectrum of a C8-MPN coated glass slide before (solid line) and after (dashed line) several minutes of static exposure to vapors generated by injecting 5 µL of liquid toluene into the cuvette and sealing the lid.